Molecular mechanism of multivalent lipid binding mediated endocytosis and intracellular traffic

Inaugural-Dissertation

to obtain the academic degree

Doctor rerum naturalium (Dr. rer. nat.)

submitted to the Department of Biology, Chemistry, Pharmacy

of Freie Universität Berlin

by

Raluca Groza

2023

This doctorate study was conducted from February 2018 to August 2023 under the supervision of Prof. Dr. Helge Ewers in the Department of Biology, Chemistry and Pharmacy of the Freie Universität Berlin.

1st Reviewer: Prof. Dr. Helge Ewers, Freie Universität Berlin

2nd Reviewer: Prof. Dr. Francesca Bottanelli, Freie Universität Berlin

Date of defence: 20th of November 2023

Declaration of independent work

Herewith I certify that I have prepared and written my thesis independently and that I have not used any sources and aids other than those indicated by me. The dissertation has not been submitted to any other examination procedure or to any other institution.

Abstract

Non-enveloped viruses make use of multivalent lipid binding to mediate their uptake into cells. It is established that the tumor-inducing Simian Virus 40, a member of the polyomavirus family, can induce dramatic membrane curvature in the plasma membrane of cells by binding multivalently to 360 copies of its glycolipid receptor GM1. This ultimately leads to its internalization through clathrin-independent endocytosis and productive infection of the cells. It remains unclear whether this is a generic biophysical mechanism employed by non-enveloped lipid binding viruses to mediate their uptake in a clathrin-independent manner. Here, I found that several members of the polyomavirus family deform membranes *in vitro* and in cells, strengthening the hypothesis that multivalent lipid binding might be a common biophysical mechanism for membrane deformation and internalization. To further test this hypothesis, I designed a synthetic cellular system for the investigation of endocytosis mediated by globular particles multivalently binding to lipidic receptors in the plasma membrane. This system is composed of a recombinantly expressed globular virus-like-particle and corresponding lipid-anchored receptors. I made use of the *encapsulin* protein from the archaeon *Pyroccoccus furiosus* to which GFP was genetically linked and then self-assembles from 180 subunits into a 37 nm diameter capsid bearing regularly-spaced GFP molecules on the surface, here onward called GEM. As receptors for this globular virus-like-particle, I attached a GPI-anchor to 7 different anti-GFP nanobodies with individual binding affinities increasing from the µM to the pM range. This enabled me to range the adhesion energy of synthetic pentavalent lipid binding particles to membranes over 7 orders of magnitude and study the biophysics required for efficient membrane deformation and subsequent internalization to occur. For this, I reconstituted this receptor-ligand system *in vitro* and in cells and found that particles deform membranes and become internalized in a clathrin-independent manner, provided that the adhesion energy is high enough. Based on experimental work on cells and liposomal membranes and theoretical considerations, a physical model was derived to explain membrane wrapping by GEMs into long, tubular invaginations as a function of binding affinity. My work shows that polyvalent lipid binding alone is sufficient for membrane deformation and clathrin-independent internalization and provides mechanistic insight into the biophysical basis of multivalent lipid-binding mediated membrane deformation by non-enveloped, tumor-causing virions.

Secondly, non-enveloped viruses are known to traffic through the lysosomes towards their final destination in the cell, the endoplasmic reticulum, as they require the acidic environment of the endosomal compartments for disassembly and release of their genetic material. On the other hand, bacterial toxins such as the β-subunit of the Cholera toxin traffic to the Golgi apparatus instead, even though they share a similar pentavalent organization of binding sites with the core structural protein of polyomaviruses and bind to the

same lipidic moiety in the plasma membrane of cells. The mechanisms conferring the intracellular trafficking specificity to these two pathogens is not yet understood. Here I investigate whether the nanoscale configurations and multivalency of lipid binding sites on these pathogens dictates their intracellular routes. First, I found that several lipid-binding viruses are transported through the endo-lysosomal pathway after endocytosis while completely bypassing the Golgi apparatus, suggesting the existence of a global mechanism conferring specificity to their intracellular sorting. To further understand this, I used the synthetic cellular system described above to test the trafficking of a globular viral mimic with similar architecture of binding sites as the polyomaviruses. I found that the synthetic particles traffic through the endo-lysosomal system in a similar fashion to the virions. Secondly, I studied the minimum requirements conferring the Golgi transport specificity to bacterial toxins. I investigated the intracellular transport of toxin mimics with similar number and flat configuration of lipid binding sites. I found that none of the toxin mimics used in this study could successfully reproduce the Golgi trafficking of bacterial toxins, suggesting that multivalent lipid binding arranged on a flat configuration is not sufficient to provide such intracellular trafficking specificity. My work opens questions as to what other factors are at play in the binding and entry of such pathogens that provide the necessary cues for intracellular transport.

Zusammenfassung

Unbehüllte Viren nutzen die multivalente Lipidbindung, um ihre Aufnahme in Zellen zu vermitteln. Es ist erwiesen, dass das tumorinduzierende Simian Virus 40, ein Mitglied der Familie der Polyomaviren, durch multivalente Bindung an 360 Kopien seines Glykolipidrezeptors GM1 eine dramatische Membranverkrümmung in der Plasmamembran von Zellen hervorrufen kann. Dies führt schließlich zu seiner Internalisierung durch Clathrin-unabhängige Endozytose und einer produktiven Infektion der Zellen. Es bleibt unklar, ob dies ein allgemeiner biophysikalischer Mechanismus ist, der von nicht umhüllten lipidbindenden Viren genutzt wird, um ihre Aufnahme auf eine Clathrin-unabhängige Weise zu vermitteln. Hier habe ich festgestellt, dass mehrere Mitglieder der Polyomavirus-Familie Membranen in vitro und in Zellen deformieren, was die Hypothese bestärkt, dass die multivalente Lipidbindung ein allgemeiner biophysikalischer Mechanismus für die Deformation und Internalisierung von Membranen sein könnte. Um diese Hypothese weiter zu testen, habe ich ein synthetisches zelluläres System für die Untersuchung der Endozytose entwickelt, die durch die multivalente Bindung globulärer Partikel an Lipidrezeptoren in der Plasmamembran vermittelt wird. Dieses System besteht aus einem rekombinant exprimierten globulären virusähnlichen Partikel und entsprechenden lipidverankerten Rezeptoren. Ich habe das Encapsulin-Protein aus dem Archaeon Pyroccoccus furiosus verwendet, an das GFP genetisch gebunden wurde und das sich dann selbst aus 180 Untereinheiten zu einem Kapsid mit einem Durchmesser von 37 nm zusammensetzt, das regelmäßig verteilte GFP-Moleküle auf der Oberfläche trägt, im Folgenden GEM genannt. Als Rezeptoren für dieses kugelförmige virusähnliche Teilchen habe ich einen GPI-Anker an 7 verschiedene Anti-GFP-Nanokörper mit individuellen Bindungsaffinitäten vom µM- bis zum pM-Bereich angebracht. Dies ermöglichte mir die Adhäsionsenergie synthetischer fünfwertiger Lipidbindungspartikel an Membranen um sieben Größenordnungen zu variieren und die für eine effiziente Membranverformung und anschließende Internalisierung erforderliche Biophysik zu untersuchen. Zu diesem Zweck habe ich dieses Rezeptor-Ligand-System in vitro und in Zellen rekonstituiert und festgestellt, dass die Partikel Membranen verformen und unabhängig von Clathrin internalisiert werden, sofern die Adhäsionsenergie hoch genug ist. Auf der Grundlage experimenteller Arbeiten an Zellen und liposomalen Membranen sowie theoretischer Überlegungen wurde ein physikalisches Modell abgeleitet, das die Membranumhüllung durch GEMs in lange, röhrenförmige Einstülpungen als Funktion der Bindungsaffinität erklärt. Meine Arbeit zeigt, dass die Bindung an ein mehrwertiges Lipid allein für die Deformation der Membran und die Clathrin-unabhängige Internalisierung ausreicht, und gibt einen mechanistischen Einblick in die biophysikalischen Grundlagen der durch multivalente Lipidbindung vermittelten Deformation der Membran durch nicht umhüllte, tumorverursachenden Virionen.

Zweitens ist bekannt, dass unbehüllte Viren durch die Lysosomen zu ihrem endgültigen Bestimmungsort in der Zelle, dem endoplasmatischen Retikulum, wandern, da sie das saure Milieu der endosomalen Kompartimente für die Zerlegung und Freisetzung ihres genetischen Materials benötigen. Bakterielle Toxine wie die β-Untereinheit des Cholera-Toxins hingegen werden stattdessen zum Golgi-Apparat transportiert, obwohl sie eine ähnliche pentavalente Organisation der Bindungsstellen mit dem Kernstrukturprotein der Polyomaviren teilen und an denselben Lipidanteil in der Plasmamembran der Zellen binden. Die Mechanismen, die diesen beiden Krankheitserregern die Spezifität des intrazellulären Transports verleihen, sind noch nicht bekannt. Hier untersuche ich, ob die nanoskaligen Konfigurationen und die Multivalenz der Lipidbindungsstellen dieser Krankheitserreger ihre intrazellulären Routen bestimmen. Zunächst stellte ich fest, dass mehrere lipidbindende Viren nach der Endozytose durch den endolysosmalen Weg transportiert werden, wobei der Golgi-Apparat vollständig umgangen wird, was auf die Existenz eines globalen Mechanismus hindeutet, der ihrer intrazellulären Sortierung Spezifität verleiht. Um dies besser zu verstehen, habe ich das oben beschriebene synthetische zelluläre System verwendet, um den Verkehr eines globulären viralen Imitats mit einer ähnlichen Architektur von Bindungsstellen wie die Polyomaviren zu testen. Ich fand heraus, dass die synthetischen Partikel das endo-lysosomale System in ähnlicher Weise wie die Virionen durchqueren. Zweitens untersuchte ich die Mindestanforderungen, die den bakteriellen Toxinen die Golgi-Transportspezifität verleihen. Ich untersuchte den intrazellulären Transport von Toxin-Imitaten mit einer ähnlichen Anzahl und flachen Konfiguration von Lipidbindungsstellen. Ich fand heraus, dass keines der in dieser Studie verwendeten Toxin-Mimics den Golgi-Transport bakterieller Toxine erfolgreich reproduzieren konnte, was darauf hindeutet, dass eine multivalente Lipidbindung in einer flachen Konfiguration nicht ausreicht, um eine solche Spezifität des intrazellulären Transports zu gewährleisten. Meine Arbeit wirft die Frage auf, welche anderen Faktoren bei der Bindung und dem Eintritt solcher Krankheitserreger eine Rolle spielen, die die notwendigen Hinweise für den intrazellulären Transport liefern.

Table of contents

Abbreviations

Abbreviation	Full form
BAR	Bin/Amphiphysin/Rvs
BKPyV	BK polyomavirus
CAV	Caveolae
CCP	Clathrin-coated pit
CIE	Clathrin-independent endocytosis
CHC	Clathrin heavy chain
CLC	Clathrin light chain
CME	Clathrin-mediated endocytosis
CLEM	Correlative light electron microscopy
CLIC	Clathrin-independent carriers
Ctrl	Control
CTxB	B-subunit of Cholera toxin
DOPC	1,2-dioleoyl-sn-glycero-3-phosphocholine
EGFP	Enhanced green fluorescent protein
Eq.	Equation
EM	Electron microscopy
ER	Endoplasmic reticulum
et. al.	Et alii
FEME	Fast endophilin-mediated endocytosis
Gb3	Globotriaosylceramide
GD1a	Disialoganglioside isomer a
GD1b	Disialoganglioside isomer b
GEEC	Glycosylphosphatidylinositol-anchored protein enriched compartments
GEM	Genetically encoded multimeric nanoparticle
GFP	Green fluorescent protein
GL-Lect	Glycolipid-lectin hypothesis
GM1	Monosialoganglioside
GPI	Glycosylphosphatidylinositol
GPI-NB	Glycosylphosphatidylinositol-anchored nanobody
GPMV	Giant plasma membrane derived vesicle
GTP	Guanosine-5'-triphosphate
GT1a	Trisialoganglioside isomer a
GT1b	Trisialoganglioside isomer b
GUV	Giant unilamellar vesicle
JCPyV	JC polyomavirus
KD	Knock down
K_D	Dissociation constant
kDa	Kilodalton

MCPyV	Merkel cell polyomavirus
mPyV	Mouse polyomavirus
NB	Nanobody
nM	Nanomolar
PREM	Platinum replica electron microscopy
RFP	Red fluorescent protein
siRNA	Silencing RNA
SV40	Simian virus 40
STxB	B-subunit of Shiga toxin
TIRF	Total internal reflection fluorescence
Tf	Transferrin
TfR	Transferrin receptor
VLP	Virus-like-particle
VP1	Viral protein 1

List of figures and tables

Chapter 1. Introduction

Chapter 1.1. Prologue

It all started in 1665, a time in which scientists would gather in coffeehouses around major scientific hubs to discuss what now seems to be rudimentary science, a time in which the bubonic plague started to cripple European society, yet Robert Hooke's simplistic idea of mounting three lenses on top of each other to look at the details of a cork led to the birth of cell biology as we know it today. It was Hooke's cork that inspired him to coin the term <cell> and little did he know at the time about the long-lasting impact his observation would have on the world, leading to cell theory. It is universally accepted that the cell is the fundamental building block of life itself and the most complex autonomous machine known so far. It makes use of an intricate system of molecular processes for survival and proliferation, governed by the laws of physics, chemistry, and biology, many of which remain elusive. One of the biggest challenges of the 21st Century scientific research is to decipher the functioning of cells, both as an individual entity and in the larger context of a tissue.

The structure of the cell. Cells need to maintain metabolism, proliferate and perform a wide range of specialized tasks to ensure homeostasis. Cells have inner compartments called "organelles" that perform specialized functions. For example, storage and expression of the genetic information takes place inside the nucleus, protein and lipid biogenesis and traffic occurs through the endoplasmic reticulum and the Golgi apparatus, the chemical energy of the cell is produced by the mitochondria, cellular support and motility are mediated by the cytoskeleton etc. Most organelles are surrounded by a membrane for compartmentalization that allows each of them to have a unique chemical composition required for their given task.

The plasma membrane. The cell is surrounded by the plasma membrane that separates and protects it from its external environment. The main components of the plasma membrane are phospholipids, glycolipids, sterols and proteins. Due to the amphipathic character of lipids, the membrane is organized as a fluid bilayer around 4-5 nm thick, with the hydrocarbon tails of the lipids buried away from the aqueous environment and the polar head groups extending towards the extracellular space or towards the cytosol. Transmembrane proteins are inserted in between the phospholipids in the bilayer and are free to diffuse laterally **(Figure 1.1)**[1]. This model of the organization of the membrane, the fluid mosaic model, was proposed in 1972 by Singer and Nicolson and is still considered to this day to be the standard view on the structure of

the plasma membrane. Due to the fluidity of the membrane and its components, the cell can respond to exogeneous cues and can facilitate cellular processes.

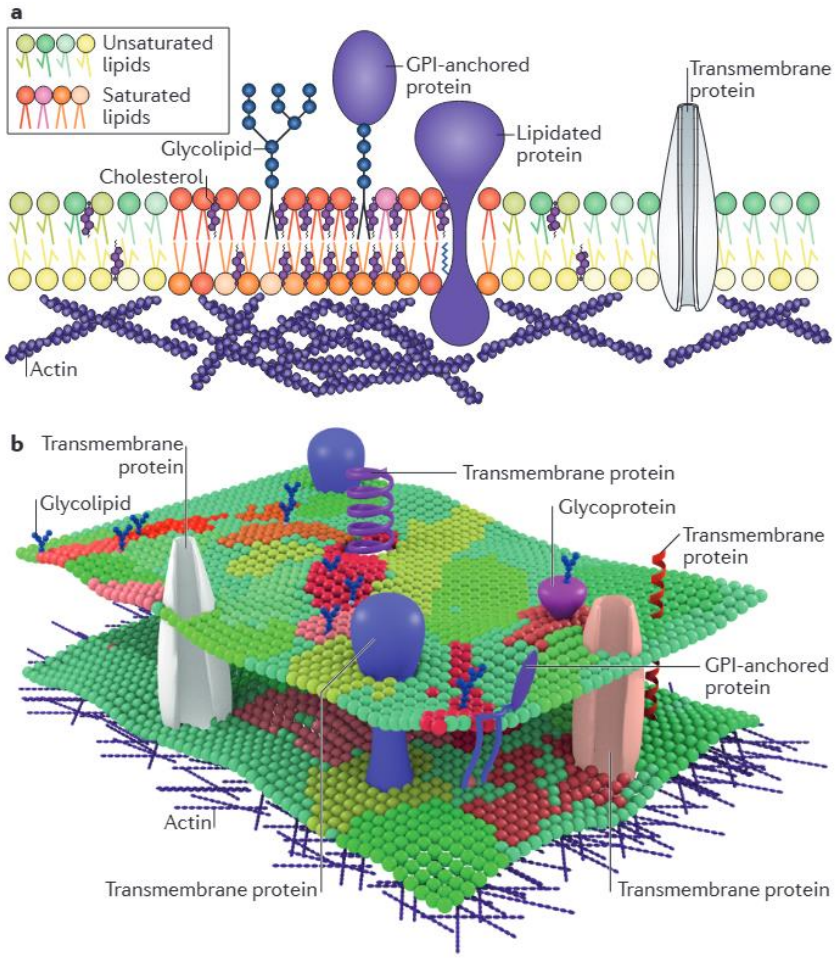

Figure 1.1. The organization of the plasma membrane. A) Schematic 2D representation of the structure and components of the membrane and the actin scaffold underneath. **B)** Schematic 3D representation of the membrane and its components. For simplicity, only the lipid headgroups are represented as spheres of different colours corresponding to their levels of saturation. Reproduced with permission from Sezgin *et al*, Nat Rev Mol Cell Biol, 2017[2].

Phase separation and lipid nanodomains. The composition and organization of the plasma membrane allows it to act as an information receiving and processing hub. It is responsible for the uptake of nutrients and other vital molecules, intracellular signalling and cell adhesion. The plasma membrane of cells exhibits a remarkable lipid asymmetry, meaning that the composition of lipids is different between the two leaflets of the bilayer. The outer leaflet is abundant in phosphatidylcholine, sphingomyelin and cholesterol, while the inner leaflet is enriched with phosphatidylethanolamine, phosphatidylserine, and phosphatidylinositol. This lipid asymmetry is essential for various cellular functions, such as the recruitment

and activation of signalling molecules in response to external stimuli. Lipid asymmetry also contributes to membrane curvature and stability, affecting membrane protein distribution and function. In fact, the proteins embedded in the membrane are mostly responsible for the functionality of the plasma membrane. Even though approx. half of the weight of the plasma membrane consists of lipids and half of proteins, the ratio of proteins to lipids in the bilayer is around 1:100, given the larger size of the proteins[3]. Given the fluidity of the membrane, it is crucial to bring together lipid and proteins in confined regions mediated by cytoskeleton interactions that would facilitate basic cellular processes such as intracellular signalling.

The free diffusion of certain proteins is restricted due to their association with specialized lipid microdomains, also known as lipid rafts. These domains are transient and form through the phase separation of lipids and proteins and are enriched in cholesterol, sphingomyelin and GPI-anchored proteins. The components of these domains are tightly packed and form liquid ordered regions in the membrane, whose height differs from the liquid disordered region surrounding it. The height mismatch between the different phases in a membrane can lead to line tension surrounding the ordered domain and ultimately to spontaneous curvature of the membrane. Therefore, membrane domains are important for the process of endocytosis as well, in which the generation of membrane curvature can facilitate the formation of endocytic pits. Endocytosis, also known as cellular eating and drinking, is one of the most vital processes that the cell undergoes. It is responsible for nutrient uptake, triggering intracellular signaling cascades[4] and the regulation of the availability of proteins and receptors at the plasma membrane[5]. Endocytosis is the main topic of the first results chapter of this thesis and will be introduced in detail in the subsequent sections of the Introduction.

Chapter 1.2. Endocytosis

Endocytosis is the fundamental cellular process through which cells ingest their nutrients and other molecules needed for their own survival and function within the organism, furthermore, this process is hijacked by several pathogens for invasion leading to infection. Cells evolved to the complex systems they are today due to their ability to engulf surrounding cargo. The first observation of an endocytic process under the microscope was made by Ilya Metchnikoff in 1883, as he was imaging cells engulfing small splinters in transparent starfish larva[6]. He termed this process "phagocytosis" from the Greek "phagos" = to eat and "cyte" = cell. It was only in 1931 that a secondary endocytic mechanism was uncovered by Warren H. Lewis who observed by time-lapse imaging the engulfment of fluids in cells, a process he called "pinocytosis" from the Greek "pinean" = to drink[7]. Both phagocytosis and pinocytosis are large-scale endocytic events, with pit diameters over 0.5 µm and could be easily observed with conventional microscopes.

The research field of endocytosis took off after the development of electron microscopy in the 1930s. Palade and Yamada independently made the first observations of caveolae in 1953 and 1955 respectively during electron microscopy imaging sessions[8,9]. Another pivotal study came out in 1964 by Roth and Porter, the first ones to describe clathrin-mediated endocytic processes[10]. They developed a time-course pulse-chase assay to study cargo uptake: they allowed mosquitos to feed on blood and fixed them after certain time intervals to visualize the uptake of yolk proteins into mosquito oocytes. They described the coat formation and even the coat disassembly process. Yet, electron microscopy studies were limited in their abilities, as they could only be used to describe the morphological features of the cell and not the biochemistry behind it.

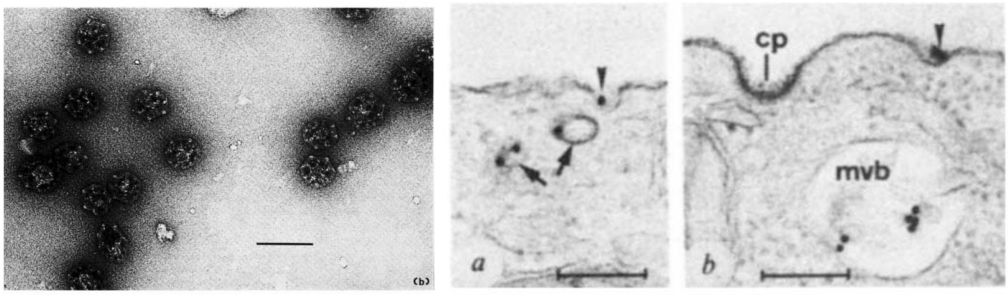

Figure 1.2. The first electron micrographs of endocytic processes and their components. (Left image) Electron micrograph of purified clathrin-coated vesicles from pig brain. Reproduced with permission from Pearse, JMB, 1975[11]. **(Right images)** Electron micrographs of non-coated endocytic pits formed by tetanus toxin labeled with gold (arrowheads) versus empty clathrin-coated pits (marked cp). Reproduced with permission from Montesano et al, Nature, 1982[12].

The molecular players involved in endocytosis were first identified shortly after, once the cellular fractionation by ultracentrifugation technique was developed by Albert Claude in the 1940s[13]. Barbara M.

Pearse was the first scientist to purify clathrin-coated vesicles from pig brain using the subcellular fractionation method and imaged them with electron microscopy (**Figure 1.2**, left panel). She then proceeded to isolate the major protein in these vesicles and named it "clathrin" since it resembled a lattice-like structure[14]. After this major discovery, the field of clathrin-mediated endocytosis (CME) was born and it remains to this day the most studied endocytic mechanism[15].

The first indications that endocytosis could occur even in the absence of coat proteins came from early studies on the entry of bacterial toxins such as tetanus and cholera toxins (**Figure 1.2**, right panel)[12]. Moreover, it was shown that under hypotonic shock when clathrin assembly is arrested, ricin toxin internalization can still occur unaffected[16]. In fact, ricin internalization could still occur even when the cytosol is acidified and the clathrin-mediated uptake of Transferrin is strongly inhibited[17]. These three studies suggested the existence of a secondary pathway independent of clathrin, but this hypothesis was met with great resistance in the field and quickly dismissed. Eventually, a dynamin mutant was created that inhibits clathrin-mediated uptake, but not fluid uptake and so the existence of different endocytic routes became generally accepted[18].

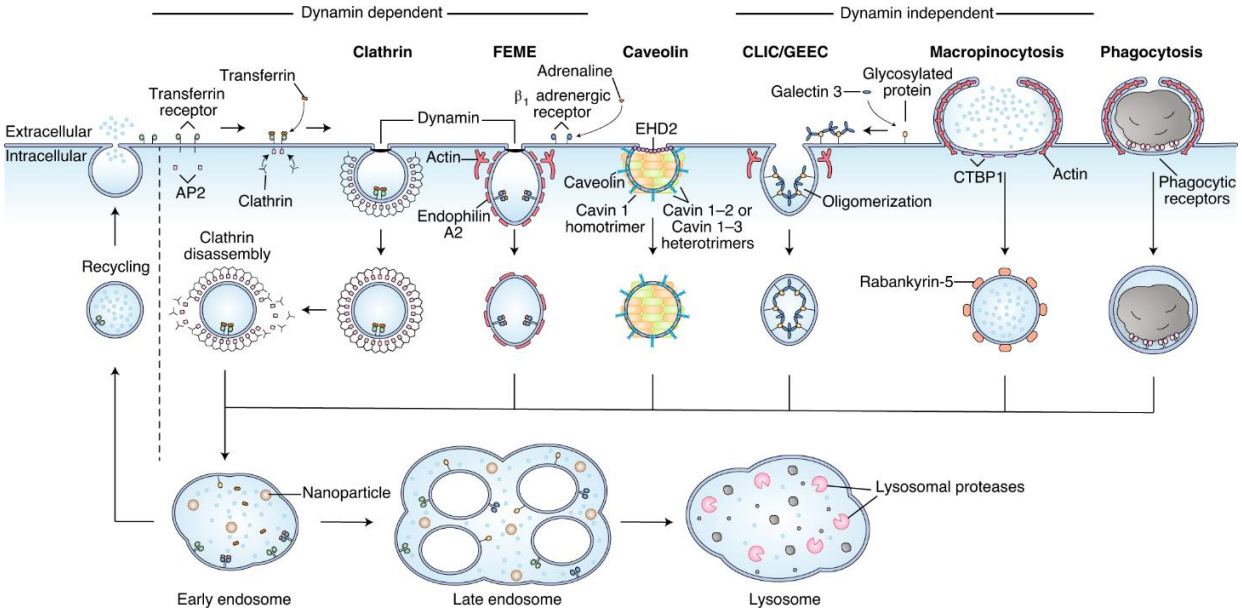

Figure 1.3. Overview of the endocytic mechanisms known to date and the molecular players involved. Reproduced with permission from Rennick *et al*, Nat Nanotech, 2021[19].

Nowadays, it is well-established that endocytosis can occur in a clathrin-dependent[15,20] or clathrin-independent manner[21,22]. There have been many endocytosis mechanisms described and providing a unifying classification is challenging due to the plethora of molecular players involved. A description of the endocytic pathways discovered to date is provided in the next sections of this chapter and in **Figure 1.3**. Large-scale endocytosis such as phagocytosis or micropinocytosis are out of the scope of this work.

Chapter 1.2.1. Clathrin-mediated endocytosis

Clathrin-mediated endocytosis is undoubtedly the main constitutive uptake pathway employed by all eukaryotic cells. Some studies even suggest that the other endocytic pathways are redundant and have no explicit functionality[23]. There is a plethora of known cargo that exploits this mechanism, mostly consisting of extracellular ligands binding to transmembrane proteins. The main steps in generating a clathrin-coated pit (CCP) are well-established and represented in **Figure 1.4**: 1) initiation 2) cargo selection 3) coat assembly 4) scission 5) uncoating and 6) fusion with endosomes.

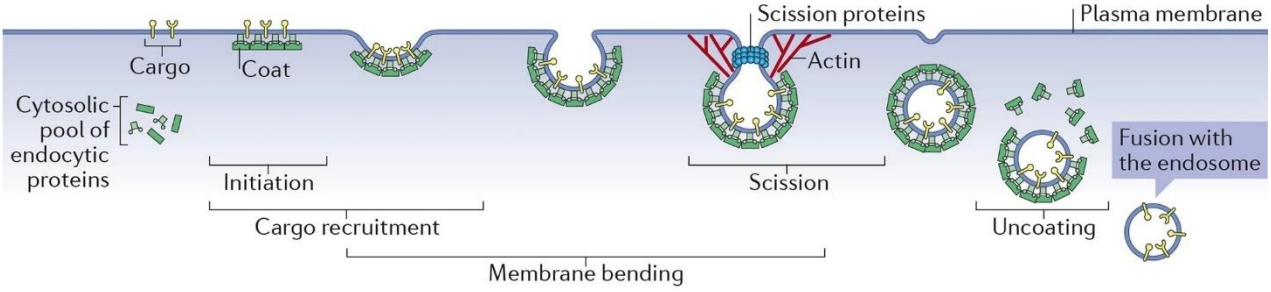

Figure 1.4. The main sequence of events in clathrin-mediated endocytosis. Reproduced and modified with permission from Kaksonen and Roux, Nat Rev Mol Cell Biol, 2018.

Initiation and cargo selection. The sequence of events during CME as well as the proteins involved are evolutionarily conserved from yeast to humans. There are over 50 different proteins involved that are recruited from the cytosolic space and become assembled onto the protein complex at specific times and places during the generation of the endocytic pit (**Figure 1.5**) [20,24]. Based on their function, these proteins can be grouped into modules. The first modular part of CCP generation is the initiation of the clathrin coat. Since clathrin is not able to bind directly to membranes, adaptor proteins are involved in the formation of the CCP. First, a putative nucleation site is generated on the plasma membrane by local PtdIns(4,5)P_2 enrichment and is mediated by the protein FCHo in both mammals and yeast[25,26]. After nucleation, the cargo destined for internalization is selected. The AP2 complex mediates clathrin recruitment to the specific cargo-attachment site[27] as it can bind to both PtdIns(4,5)P_2 lipids[28] and tyrosine-containing motifs in the cytoplasmic tails of transmembrane receptors destined for CME[29,30]. Several adaptor proteins involved in the early stages of CCP formation can induce curvature as well, such as epsins that bind to PI(4,5)P_2[31], epidermal growth factor receptor substrate 15 or intersectins[15].

Coat assembly and membrane bending. After cargo selection, clathrin triskelia are recruited from the cytosol to sites of adaptor protein nucleation, mediated mostly by AP2. These triskelia then polymerize on the forming vesicle into icosahedral cages, contributing to membrane bending as it does so[14,32]. In order

for cellular membranes to bend, the innate membrane tension forces have to be overcome. Clathrin polymerization exerts a force in the same range or higher than the plasma membrane tension leading to successful bending. It was shown in *in vitro* reconstitution assays that for higher tension ranges than the cellular membrane tension, clathrin scaffolding is no longer able to induce curvature[33]. Some studies debate whether clathrin assembly alone can trigger curvature, since many flat, fully-assembled clathrin lattices have been observed on the membrane that do not bend membranes into an endocytic pit[34]. Other more recent studies found that these flat lattices can actually spontaneously curve into coated pits without the aid of adaptors[35,36]. The adaptor proteins themselves have intrinsic curvature induction properties, for example the epsin protein has an amphipathic helix in its N-terminal domain[31] that acts as a wedge on the membrane[37]. Moreover, it was recently found that epsins and FCHo associate multivalently with each other and phase-separate in liquid protein droplets, thus facilitating the maturation of the pit[38,39]. The cytoskeleton plays a very important role in inducing membrane curvature as well. Actin assembles locally around the nascent pit in both mammalian and yeast cells and starts polymerizing around the base of the clathrin coated pit[40–42], producing enough force to pull the vesicle inward. In addition, motor proteins associated with actin could exert a pulling force on the nascent CCPs, for example myosins were found to be involved in endocytosis in mammalian cells[43,44]. Most likely, curvature generation in CME is a concerted action of all the proteins described above (**Figure 1.5**), rather than the unique action of one individual player.

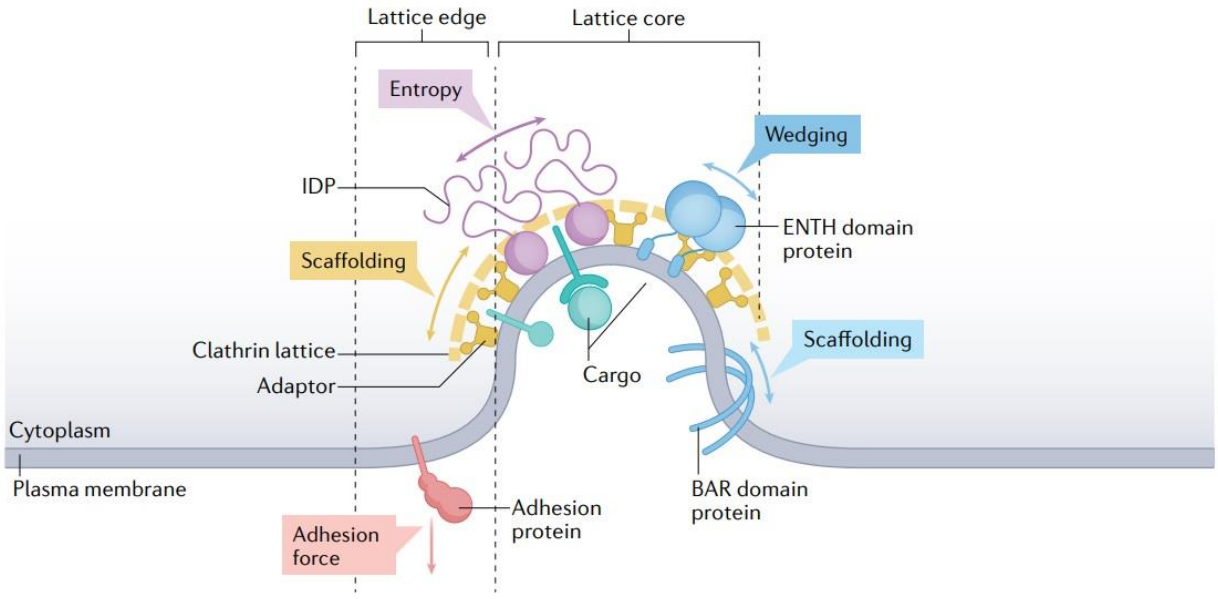

Figure 1.5. The molecular players involved in curvature generation during the initiation and maturation of the clathrin-coated endocytic pit. The force generation mechanisms include wedging by protein insertion, scaffolding by clathrin and adaptors and entropy caused by disordered protein domains. Figure reproduced with permission from Kozlov and Taraska, Nat Rev Mol Cell Biol, 2023[35].

Scission and final stages. Generally, the scission of mature endocytic pits occurs by active constriction mechanisms realized through the binding of either dynamin pinchases or BAR (Bin/Amphiphysin/Rvs) domain proteins. Dynamins self-assemble around the neck of the endocytic pit into ring-shaped structures and promote scission though constriction forces[45,46]. BAR domain proteins have a preference for curved membranes and also bind to the necks of the forming CCPs, stabilizing the vesicles and recruiting dynamins[47,48]. These proteins have an elongated banana shape and bind to each other, creating a scaffold around the neck of the forming pit and recruiting actin, which then contributed to scission by exerting polymerization forces onto the vesicle[48,49]. Finally, after pinch-off, the clathrin coat surrounding the internalized vesicle disassembles rapidly, leaving the uncoated vesicle to fuse with early endosomes.

Physiological functions. The main function of CME is to constitutively internalize receptors (meaning with or without exogeneous ligands bound) carrying metabolites into cells. A classic, well-studied example is the uptake of Transferrin (Tf) and Transferrin receptors (TfR). Transferrin is an iron-binding protein that binds to its receptor on the plasma membrane, internalizes through CME and traffics through early endosomes and recycling endosomes back to the plasma membrane[50]. The second main function of CME is the regulation of signal transduction by controlling the surface levels of proteins, especially important in the activity of synapses. CME is essential for synaptic vesicle recycling and plays a role in the regulation of the size and composition of these vesicles[51].

Exploitation by pathogens such as toxins and viruses. Small pathogens such as bacterial toxins can be easily integrated into a CCP for internalization. One of the largest toxins known to enter via this pathway is anthrax, about 25 nm x 10 nm in size. Most toxins trigger the formation of lipid clusters upon membrane binding to facilitate their internalization. A detailed list of several toxins and their uptake mechanisms are included in **Table 1.1** in the next chapter. Many viruses use CME to mediate their uptake in cells. For example the small Semliki forest virus (around 30 nm in diameter) but also larger viruses such as the reovirus (85 nm diameter) or the influenza A virus (120 nm diameter) are integrated into CCP that increase their size to accommodate the viruses[20]. A more detailed description of the entry mechanism of several viruses is provided in **Table 1.2** in the next chapter.

Chapter 1.2.2. Caveolin-mediated endocytosis

Caveolae can form pits at the plasma membrane that become internalized, but the function of caveolin-mediated endocytosis is not yet understood. The density of caveolae varies greatly among cell types, in contrast to the more constant density of clathrin-coated pits. Caveolae are highly abundant in certain cell types such as muscular cells, adipocytes and endothelial cells where they can cover up to 50% of the total membrane surface area[52]. Caveolae are completely lacking in other cell types such as kidney proximal tubule cells[53]. Caveolae are unique as they can form higher order structures on the plasma membrane, composed out of multiple caveolin-coated buds organized in clusters or rosettes, connected to the membrane via a common neck (**Figure 1.6**, right image).

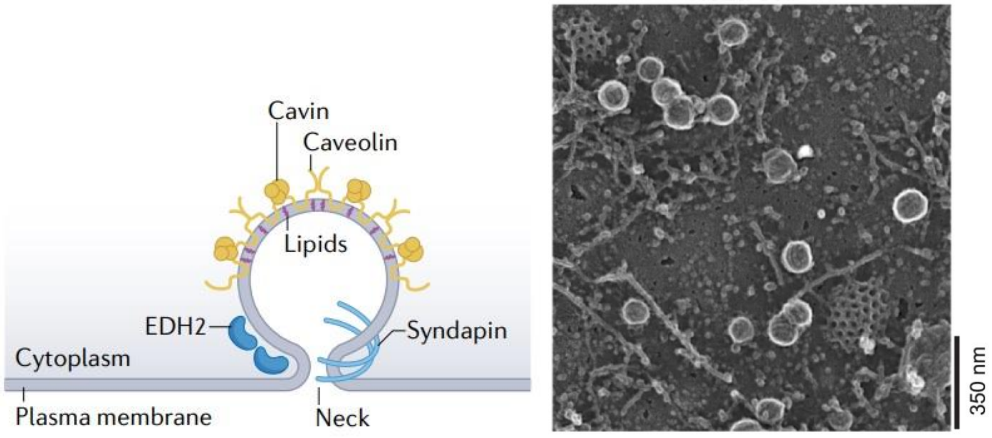

Figure 1.6. Caveolin mediated endocytosis. Left image. Schematic of the organization of the caveolin coat. Reproduced with permission from Kozlov and Taraska, Nat Rev Mol Cell Biol, 2023. **Right image.** Platinum replica electron micrograph of caveolae in HeLa cells. Figure reproduced from Matthaeus *et al*, Nat Commun, 2022[54].

Caveola formation. The caveolin-coated pit is a spherical bulb with a diameter of around 90 nm and is formed by the cooperative assembly of the caveolin and cavin proteins (**Figure 1.6**, left image). These proteins assemble into a coat in a few minutes, a longer process than clathrin-coated pit formation[55]. Caveolin1 is the main protein driving curvature on the membrane, as it has a transmembrane domain composed out of two α-helices that adopt a hairpin topology and insert into membranes, generating curvature through a wedging mechanism. It has been recently found that caveolin 1 proteins assemble into a 11 subunit-oligomeric flat disc that inserts itself into the membrane[56]. This caveolin1-disk structure creates contacts with other 4 neighbouring discs, creating a scaffold and facilitating the formation of the endocytic pit. However, cavin proteins are indispensable for the formation of spherical caveolae pits. Cavin family members are peripheral membrane proteins that fold into a coiled-coil conformation formed by two α-helices connected by intrinsically disordered regions. Cavins oligomerize on the caveolin-coated pit due to electrostatic interactions between their disordered regions[57] and they form the characteristic spherical striated structures

observed on caveolae in electron microscopy (**Figure 1.6**, right image)[58]. Moreover, it has been suggested that cavins alone can induce membrane curvature through liquid-liquid phase separation[57]. Several other accessory proteins are also recruited to the caveolin-coated pit during its formation and could contribute to curvature generation. For example, EHD2 and syndapin co-factors contain BAR domains that could synergistically form a scaffold together with caveolin1 and cavin proteins[59].

Scission and traffic. The caveolae are pinched off into the cytosol by the GTP-ase dynamin, which is known to associate and polymerize at the neck of caveolin-coated pits, generating the constriction force required for scission[60,61]. The accessory protein EHD2 promotes the association between caveolae and actin at the neck region, where subsequent actin polymerization might drive fission[62]. After pinching off, they fuse with either Rab5-positive early endosomes or with recycling endosomes[63,64].

Physiological functions. Caveolae have been shown to play an important role in signal transduction, as many proteins involved in signalling have structural caveolin-binding motifs[53]. In addition, it has been suggested that caveolae act as regulators of membrane tension upon mechanical stress and can provide membrane reservoirs to prevent cellular membrane rupture[53,65]. Caveolae generate a unique lipid environment enriched in PtdIns(4,5)P_2, PtdSer, and cholesterol[66] triggered by the direct binding of caveolin1 to cholesterol[67] and the binding of cavin proteins to PtdIns(4,5)P_2 lipids. Therefore, it has been suggested that the primary role of caveolin-mediated endocytosis is lipid regulation[68].

Exploitation by pathogens such as toxins and viruses. It has been found that infectious agents such as viruses and toxins colocalize with caveolin structures at their entry sites[69]. However, subsequent work has shown that caveolin-mediated endocytosis is completely dispensable for the internalization of most pathogens. Initially, the Simian Virus 40 (SV40) of the polyomavirus family was found to be internalized in a caveolin-dependent manner[70], but it was later found that genetic inhibition of caveolin leads to higher SV40 infection rates[71]. Similarly, Cholera toxin was also found to be internalized both in caveolae and in caveolin-independent pathways with the same efficiency[64,72].

Challenges in studying caveolin-mediated endocytosis. There are two major issues in attributing caveolin-mediated entry as the main uptake pathways of any cargo: 1) lack of specific inhibitors for this pathway and 2) overexpression of fluorescently-tagged caveolin might act as a dominant negative[73]. The removal of cholesterol from the plasma membrane does inhibit caveolae, however it disrupts other cellular processes as well. Genetic depletion of caveolin1 or cavin1 generally works, but there might be compensatory uptake pathways regulating endocytosis. Lastly, there is no known cargo to this day that penetrates the cell exclusively through caveolin-mediated endocytosis, therefore making it difficult to assess its physiological relevance and functionality.

Chapter 1.2.3. Clathrin and caveolin independent endocytosis

Even though clathrin-mediated endocytosis remains the main paradigm for the uptake of material into cells, there has been vast evidence for the existence of clathrin-independent endocytic mechanisms that operate at the same time. Caveolin-mediated endocytosis is one of these mechanisms and has already been presented in the previous chapter. Besides, there have been many newly identified uptake pathways that do not require vesicle scaffolding (so, no clathrin or caveolin) and can function in a dynamin-dependent or independent manner. Some of these pathways are constitutive, while other only occur when triggered by exogeneous ligands binding to the membrane, for example pathogens hijacking the cell. The main similarity between clathrin-independent endocytosis pathways is the redundancy of intracellular scaffolding machinery, while the main difference between them lies in the biophysical mechanism of membrane deformation and in the kinetics of vesicle formation.

Membrane curvature induction in clathrin-independent endocytosis. Here I explain the curvature generation process in clathrin-independent endocytosis from a biophysical perspective. I then provide a classification of possible membrane bending mechanisms. Some of these mechanisms might act in parallel in the cell and during the entry of the cargo.

In order for membranes to be bent, the energy applied on them must overcome the membrane bending energy that is characterized by the rigidity/stretching modulus κ[74]. This parameter is a mechanical characteristic of the membrane, and it describes its ability to resist stretching or compression. It highly depends on the lipid composition. Membranes containing many unsaturated lipids have a lower rigidity modulus than membranes containing a majority of saturated lipids. The presence of cholesterol also increases the bending modulus. Generally, κ values range in between 10 and 60 times the thermal energy, k_BT[75]. In phase separated membranes, the liquid-ordered region is about two times stiffer than the liquid disordered region, with κ values closer to 60 times k_BT[76,77]. The elastic energy of a membrane can be expressed as the Helfrich energy[74,78,79]:

$$E = \sigma \Delta A + \int_A \frac{\kappa}{2} C^2 \, dA \qquad (1)$$

where σ is the membrane tension, ΔA is the change in membrane area and C is the local membrane curvature. The tension in a bilayer represents the force acting on a certain membrane area and can be influenced by osmotic shock, cell stretching, lipid incorporation into the membrane or cytoskeleton interactions[79]. In clathrin-independent endocytosis, membrane bending can be achieved through the concerted action of

various molecular mechanisms, either by passive processes such as the generation of asymmetric bilayer stress due to unilateral amphipathic helix insertion, molecular crowding of proteins in domains, line tension due to changes in lipid composition, local scaffolding by BAR-domain proteins or by active processes such as actin polymerization or molecular motors.

1) *Amphipathic helix insertion.* The helix regions of proteins can insert themselves in between lipids as a wedge, generating asymmetric transbilayer stress and inducing membrane curvature[35,78,80]. This process depends on the shape of the proteins, for example conically shaped proteins can facilitate membrane bending. This process depends directly on the concentration of protein inserted into the local membrane area, as the clustering of such proteins leads to the formation of a budding vesicle. It also depends on the lipid receptor moiety, particularly the length of the acyl chains. Examples of such proteins are ion channels, epsins (involved in CME), caveolin1 (involved in caveolin-mediated endocytosis), BAR proteins and pathogens, such as bacterial toxins and viruses.
2) *Protein crowding effects.* Proteins attached to the membrane diffuse freely and collide with each other, and, at high enough concentrations, they can induce steric pressure laterally on the bilayer to the point where the membrane starts to bend[81,82]. However, this mechanism has only been observed in *in vitro* model membrane systems and at non-physiological protein concentrations. Is it possible that in cells these processes do not naturally occur as there has been no association with endocytosis described.
3) *Line tension.* Line tensions refers to the energy at the interface between membrane domains. If there is a lipid thickness mismatch between two phases, unfavorable contacts between the hydrophobic lipid chains of one phase and the hydrophilic lipid headgroups of the other phase triggers a constriction force at the interface. This force would work towards the minimization of the perimeter in between the two phases and would trigger membrane bending. This might occur when toxins or viruses induce glycosphingolipid clustering in domains by membrane binding[83–85].
4) *Scaffolding.* Some proteins can impose membrane curvature through their 3D structure upon attachment. For example, the BAR-domain proteins have dimeric backbones containing both amphipathic helixes and a banana-shaped BAR-domain. At a high enough density, these proteins make contacts with each other and create a scaffold around the nascent pit, leading to endocytosis. Recently, BAR proteins have been found to have a dual function: they can alone promote ligand-triggered endocytosis [86] and they also play a role in the scission of clathrin and caveolin-independent endocytic pits[87].
5) *The cytoskeleton and motor proteins.* As discussed in the previous chapters, actin polymerization at the neck of the forming endocytic pit generates a pulling force on the membrane, leading to both elongation of the vesicle and scission. This phenomena is observed in clathrin-independent endocytic

processes as well[49,88–90]. Moreover, motor proteins associated with the cytoskeleton can exert a pulling force on the endocytic pits that contributed to vesicle formation[91,92].

Scission and traffic. Some of the already described mechanisms that generate membrane curvature are also involved in the scission of the endocytic vesicles. For example, line tension, BAR domain proteins and actin polymerization can all contribute to vesicle pinch off. In addition, dynamin plays a role in clathrin-independent endocytosis, but it is not absolutely required for vesicle release in the cytosol. All in all, these mechanisms act in a concerted manner and can compensate for each other upon inhibition[78]. Subsequent traffic in the cell occurs first via fusion with early endosomes. From there, cargo is sorted either for the recycling pathway or further downstream. Cargo sorting is affected by the type of early endosome to which vesicles initially fuse and is further discussed in the next sections.

Classification and physiological functions. The CIE field has yet to reach a consensus regarding the classification of the various CIE types. Classifications have been proposed by several groups based on the involvement of dynamin, the type of cargo recruited, the morphology of the carrier pits or the speed of the process. Here I present three types of CIE processes based on the molecular players involved (**Figure 1.7**):

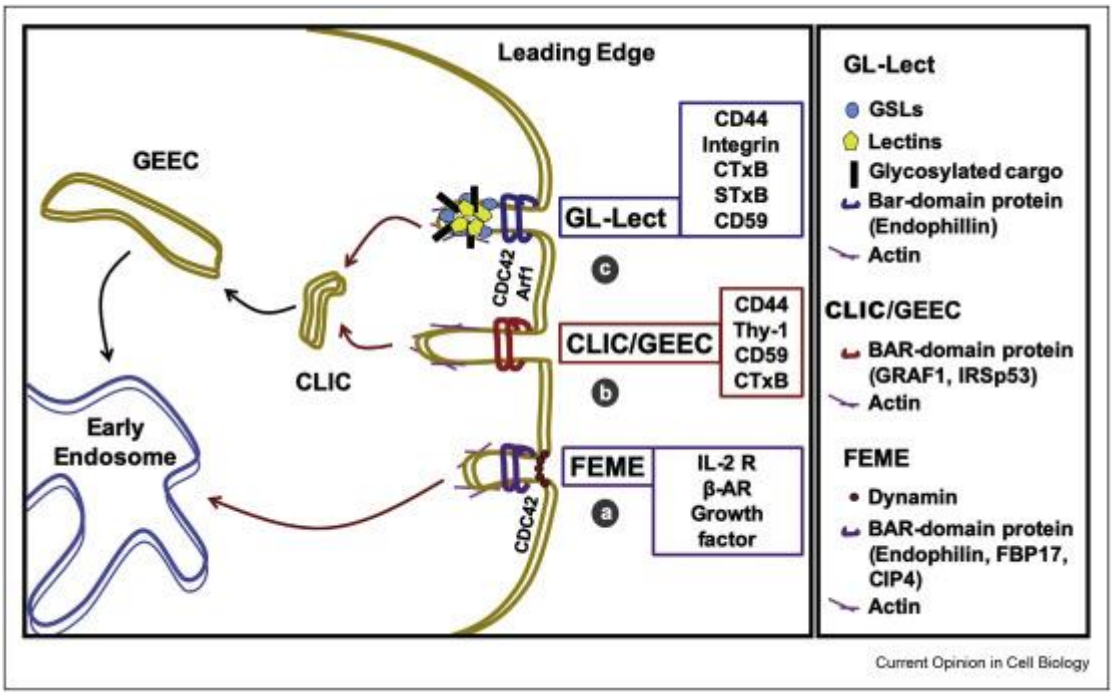

Figure 1.7. Classification of clathrin-independent endocytosis processes and the molecular players involved. Reproduced from Shafaq-Zadah *et al*, Curr Op Cell Biol, 2020 (https://doi.org/10.1016/j.ceb.2020.05.009). This article is published under the terms of the Creative Commons Attribution-NonCommercial-No Derivatives License (CC BY NC ND).

1) Fast Endophilin Mediated Endocytosis (FEME) is a newly discovered uptake pathway that relies on the scaffolding and curvature induction ability of the BAR-domain protein endophilin. It occurs

preferentially at the leading edge of cells and mediates the uptake of cargo including G-protein coupled receptors, growth factor receptors or the IL-2 receptor, by direct interaction via its SH3 domains[86].

2) The CLIC/GEEC pathway has been first observed by electron microscopy during the entry of the Cholera toxin β-subunit, as the endocytic pits containing the toxin had elongated shapes devoid of scaffolding proteins[72]. Eventually, the endocytic pits termed CLathrin-Independent Carriers (CLICs) became internalized and matured into Rab5-negative GEECs (Glycosylphosphatidylinositol-anchored protein-enriched Early Endocytic Compartments)[21]. This process has been further described during the entry of most of the native GPI-anchored proteins, the transmembrane protein CD44 and a part of the fluid phase uptake. Most likely, the cargo taken up though this pathway is then sorted for either recycling back to the plasma membrane or for degradation by subsequent fusion with pre-formed, Rab5-positive early endosomes[93].
3) The GL-Lect (glycolipid-lectin) hypothesis was proposed as an entry mechanism for lectins and lipid-binding pathogens such as bacterial toxins or viruses. During this process, cargo binding induces a reorganization of the lipid nanoenvironment and triggers the formation of tubular membranous structures that eventually become internalized in a clathrin- and caveolin-independent manner. The main difference between the CLIC/GEEC endocytosis process described in 2) and the GL-Lect hypothesis is the nature of the cargo. While CLIC/GEEC generally occurs for the regulation of endogenous transmembrane proteins and lipids, GL-Lect endocytosis occurs only when triggered by exogeneous ligand binding to cellular membranes[94,95].

Exploitation by pathogens such as toxins and viruses. Many types of toxins and viruses penetrate cells through both clathrin-mediated endocytosis and clathrin-independent endocytosis (see **Table 1.1** and **Table 1.2**). Bacterial toxins are composed out of two subunits, A and B, which have different roles in the cellular infection process. The A subunit is a catalytic machinery that can hijack the functions of the host cell, the most pronounced example being protein translation. The B subunit is responsible for the toxin binding to the cellular membrane and trafficking through the cytosol. The B subunits of bacterial toxins can be monomeric (AB toxins) or pentameric (AB_5 toxins). In many cases, the B subunits of the toxins bind to glycolipids as receptors (**Table 1.1**).

Table 1.1. Bacterial toxins: entry pathways, structure and receptors. References provided in superscript.

Toxin	CME	CIE	Caveolin	Structure	Receptors
Anthrax	✓[96]	✓[97]	-	AB	Anthrax toxin receptor
Diphtheria	✓[98]	✓[99]	-	AB	Heparin-binding epidermal growth factor precursor
Botulinum	✓[100]	-	-	-	Gangliosides and synaptotagmins I, II

Tetanus	✓[101]	✓[12]	-	AB	Gangliosides GD1b and GT1b
Ricin	✓	✓[102]	-	AB	Galactose-containing glycolipids and glycoproteins
Shiga	✓[103]	✓[84]	-	$A_1A_2B_5$	Ganglioside GD3
Cholera	✓[104]	✓[12]	✓[105]	AB_5	Ganglioside GM1

Globular viruses can be either enveloped (surrounded by a lipid membrane) or unenveloped. Based on their structural features, they have different cellular entry mechanisms. Enveloped viruses either fuse their bilayer envelope with the membrane of cells or use the spike proteins contained in their own membranes for attachment. On the other hand, nonenveloped viruses rely on the structure of their protein capsid to bind and penetrate cellular membranes. The capsids of virions are composed out of proteins arranged in icosahedrons with different symmetries, for example with a T=7 symmetry (**Table 1.2**). They generally bind multivalently to glycolipids as cellular receptors and imprint their shape onto the membrane to generate an endocytic pit. Regardless of the cell binding mechanism, most of these viruses are able to penetrate the plasma membrane through clathrin-independent endocytosis (**Table 1.2**).

Table 1.2. Viruses: entry mechanisms, structural features, diameter and receptors. References provided in superscript. NE = non-enveloped, E = enveloped.

Virus	CME	CIE	Caveolin	Structure	Diameter	Receptors
SV40	-	✓[71]	✓[70]	NE, icosahedral, T=7	~45 nm	Ganglioside GM1
mPyV	-	✓[106]	✓[106]	NE, icosahedral, T=7	~45 nm	Gangliosides GD1a and GT1b
JCPyV	?	?	✓[107]	NE, icosahedral, T=7	~45 nm	Ganglioside GD1b
BKPyV	-	✓[108]	✓[109]	NE, icosahedral, T=7	~45 nm	Gangliosides GD1b and GT1b
MCPyV	-	✓[110]	?	NE, icosahedral, T=7	~55 nm	Gangliosides GT1b and GM3
SARS-CoV-2	✓	?	?	E, spike proteins	~60-140 nm	ACE2 and gangliosides[111,112]
Norovirus	✓	✓[113]	-	NE, icosahedral, T=1, T=3	~23-40 nm	Ganglioside GD1a
Sendai	-	-*	-	E, Hemmagglutinin-Neurominidase	~200 nm	Gangliosides GD1a and GT1b

*Sendai virus enters cells via membrane fusion.

In the next section, I will present in more detail the entry mechanism of the multivalent lipid binding pathogens relevant to this study, namely the members of the polyomavirus family (e.g. the Simian Virus 40, or SV40) and the bacterial Cholera- and Shiga-toxins.

Chapter 1.3. Multivalent lipid binding in clathrin-independent endocytosis

Polyomaviruses

Polyomaviruses are small, non-enveloped, dsDNA viruses, which can infect a wide range of mammalian hosts, from birds to humans. The first polyomavirus to be discovered was the Simian Virus 40, or SV40, a virus that infects monkey cells. Polyomaviruses have been found in other organisms as well, with more than 76 different polyomaviruses identified to date, out of which 13 can infect humans. Generally, these viruses are harmless to humans, except to immunocompromised patients or to the elderly population. The most studied virions that infect humans are the JC polyomavirus (JCPyV) which might cause Progressive Multifocal Leukoencephalopathy and the Merkel Cell polyomavirus (MCPyV) which might cause Merkel Cell carcinoma, an aggressive type of human skin cancer.

The general infection pathway of polyomaviruses consists of a sequence of events: binding to the membrane, bending the membrane, uptake into the cellular space and subsequent intracellular traffic to the endoplasmic reticulum, where the genetic content of the virions is to be released. Since the polyomaviruses are non-enveloped, they must perform all these processes using the structural features of their outer capsid (**Figure 1.8**, top panel). The capsid of a polyomavirus is composed out of 72 copies of the pentameric major structural protein VP1. Each pentamer connects with neighboring pentamers via its C-terminus extensions and forms the globular, T = 7 icosahedral viral capsid of around 45 nm in diameter. Each pentamer can bind up to 5 receptors in the plasma membrane of cells therefore the fully-assembled virus can bind up to 360 receptors. Polyomaviruses bind to glycolipids found on the external leaflet of the plasma membrane, specifically to different ganglioside species containing one or more sialic acids in their structure. The interaction with the sialic acid occurs at the surface-exposed, bottom side of the pentamers. The receptor specificity is a consequence of the flexibility of the loops located in the bottom pentamer side, which can adopt distinct conformations throughout the different polyomaviruses and therefore allow different binding modes to glycolipids. Each virus binds to its glycolipid receptor with high specificity and the mutation of one single amino acid in the binding pocket of the virions can re-route the virus entirely to bind to other ganglioside species[114].

Membrane curvature generation by polyomavirus binding

The individual binding sites of polyomaviruses for their glycolipid receptors have a low binding affinity (in the mM range[115]), but the virions can bind strongly to membrane due to high avidity caused by multivalent interactions with up to 360 gangliosides. They bind tightly to the membrane, leaving virtually no space in between their capsid protein and the membrane[115,116]. To do so, the virions initially attach to a few

receptors and diffuse on the membrane, while grabbing onto more receptors until becoming immobilized in an actin-dependent manner[117]. SV40 needs to bind to a minimum of 4 receptors in order for the interaction to become irreversible[118]. Multivalent lipid binding by polyoma-virions leads to a rearrangement of lipids together with cholesterol into ordered nanodomains and might give rise to a line tension at the edge of the domain that facilitates membrane deformation. These viruses can even induce the formation of long, tubular invaginations extending from the plasma membrane into the cytosol that are filled with viruses (**Figure 1.8**, lower left panel). The formation of such invaginations has been observed in cells starved of energy, where the action of mechanical enzymes that could pinch off the tubules is inhibited thus allowing for the elongation of the endocytic pits created by the polyomas.

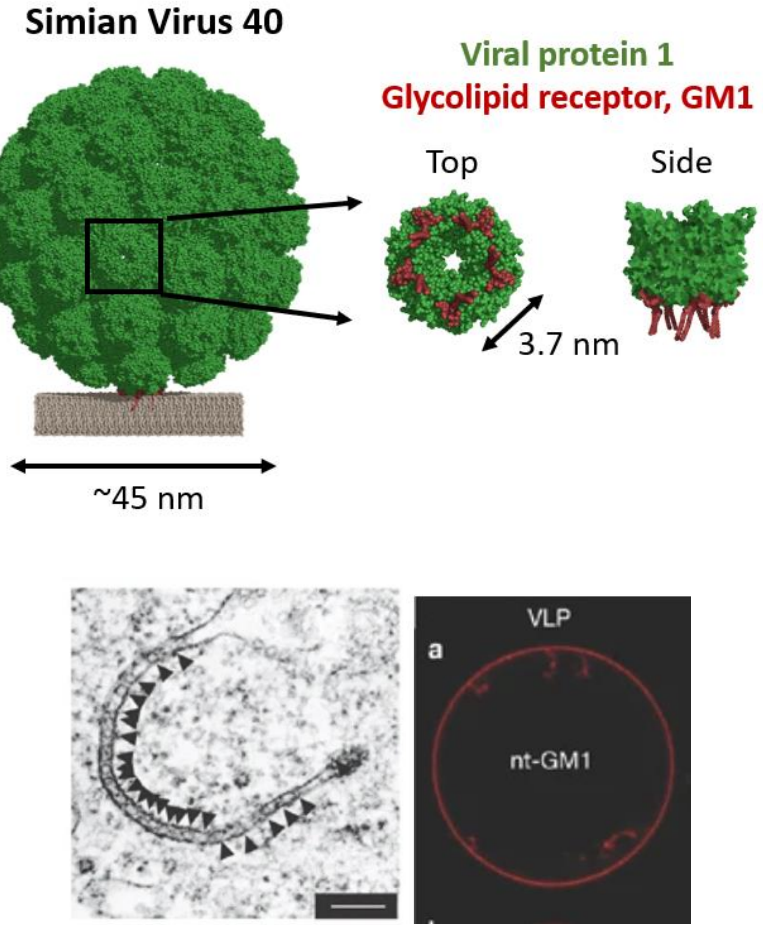

Figure 1.8. Polyoma-virions bend membranes through multivalent lipid binding. (Top) The structure of the SV40 virus (green) attached to its glycolipid receptors GM1 (red) on a membrane (beige). Insets show the pentameric structural protein VP1 from the top or from the side, highlighting the 3.7 nm spacing in between the individual binding sites. PDB files used: 3BWR. **(Bottom left)** Electron micrograph of mouse polyomavirus induced invaginations in the plasma membrane of cells. Scale bar is 200 nm. **(Bottom right)** Fluorescence micrograph of the SV40 bound to the equatorial plane of a giant unilamellar vesicle in which membrane invagination can be observed. Reproduced with permission from Ewers *et al*, Nat Cell Biol, 2010[85].

Interestingly, it seems that polyomas can induce membrane deformation without the aid of cellular machinery. For example, the same tubular invaginations observed in energy depleted cells could be reproduced in model membrane systems. These membranous structures are composed out of a bilayer vesicle with minimal lipid components and without any other proteins in its bilayer or in its lumen (**Figure 1.8**, lower right panel). Therefore, the globular polyomas are able to wrap themselves with membrane as a result of multivalent lipid binding. In contrast, antibodies with only two binding sites against the same GM1 glycolipid fail to induce similar curvature or internalization[85]. This process is highly dependent on the length of the acyl chains of the glycolipid receptors, as long acyl chains are indispensable for productive infection of the host cells[85].

Polyomavirus uptake occurs in a clathrin-independent manner

Endocytosis of the polyomaviruses is realized in a clathrin-independent manner[71], with a small fraction of the virions employing caveolin for their uptake[70]. However, the extent of caveolin involvement in polyoma-virion uptake is still unclear. Caveolins are completely dispensable for SV40 internalization as the virions can employ other clathrin- and caveolin-independent mechanisms instead[71]. The entry of polyoma-virions is moreover highly dependent on cholesterol, suggesting an involvement of lipid domains in the initial stages of endocytosis. Most likely, polyomaviruses bind tightly and multivalently to lipids which triggers the formation of liquid ordered domains and enables not only membrane deformation but also coat-protein independent internalization.

Membrane deformation by the Cholera and Shiga bacterial toxins

Cholera toxin is a protein complex secreted by the bacterium *Vibrio Cholerae* that causes severe diarrhea and dehydration in humans, leading to death when left untreated. It is generally found in the sewage systems of poorer countries, with an estimated 1.3 to 4 million people infected yearly, out of which around 100.000 deaths occur each year[119]. The B subunit of the Cholera toxin (CTxB) is responsible for the cellular attachment and intracellular traffic of the whole toxin to the Golgi apparatus. The toxin is recognized by the ER chaperone protein disulfide isomerase that cleaves the A subunit for further transport through the ER to the cytosol to complete its host cell infection. The B subunit is a pentameric protein that binds to 5 copies of the GM1 ganglioside receptor in a similar configuration as the VP1 of the polyoma-virions, also spaced 3.7 nm apart (**Figure 1.9**, top panel). However, Cholera toxin has a much higher binding affinity for its ganglioside receptor than the polyoma-virions[120].

CTxB is known to associate with liquid ordered domains in membranes. In model membrane systems, CTxB binding clusters glycolipids and induces the formation of such domains[83,121,122]. It has been

proposed that CTxB-binding induced ordered domains is a result of lipid and cholesterol co-clustering, that in turn induces the formation of line tension at the edge of the boundaries[83,123]. Moreover, CTxB clusters on the membrane as well in order to overcome the membrane tension and generate curvature. The pentameric toxin can induce the formation of long, tubular invaginations extending from the membrane in both energy-depleted cells and in *in vitro* model membranes (**Figure 1.9**, lower panels). Multivalency is key to membrane deformation, as mutant CTxB with only one active binding site fails to do so[123]. This multivalent-binding deficient mutant lost its ability to bind preferentially to ordered domains in membranes[124], and infected cells much less efficiently compared to its fully functional counterpart[125]. Interestingly, it has been recently found that Cholera toxin can enter and infect cells that are devoid of its ganglioside receptor GM1 by binding to other fucosylated receptors on the plasma membrane[126–128]. The exact role of these secondary receptors remains to be determined.

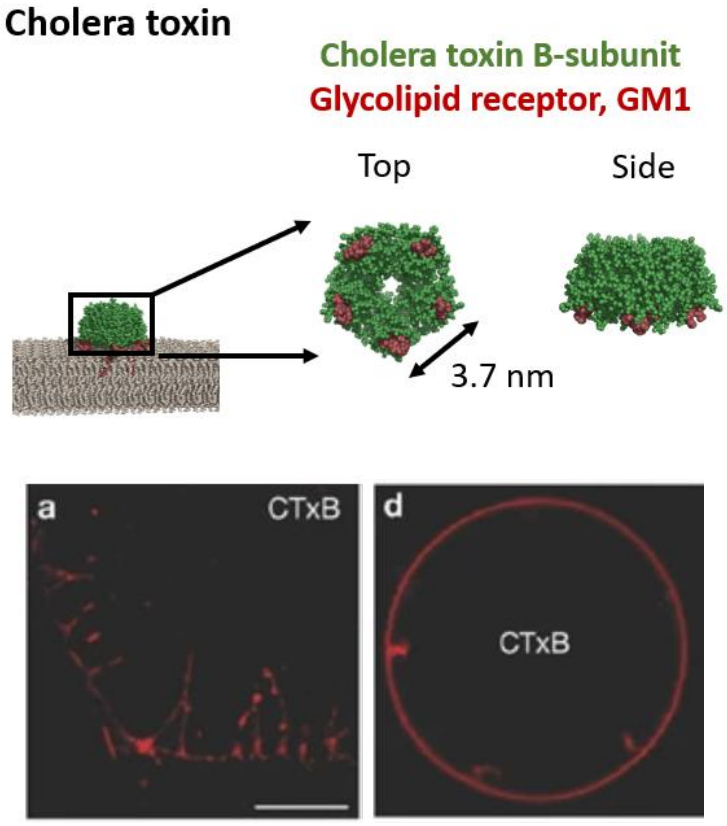

Figure 1.9. The B-subunit of Cholera toxin can deform membranes through multivalent lipid binding. (Top) The structure of the CTxB (green) attached to its glycolipid receptors GM1 (red) on a membrane (beige). Insets show the pentameric toxin from the top or from the side, highlighting the 3.7 nm spacing in between the individual binding sites. PDB files used: 6HMY. **(Bottom left)** Fluorescence micrograph of CV1 cells displaying CTxB-generated invaginations in the membrane. Scale bar is 5 µm. **(Bottom right)** Fluorescence micrograph of the CTxB bound to the equatorial plane of a giant unilamellar vesicle in which membrane invagination can be observed. Reproduced with permission from Ewers *et al*, Nat Cell Biol, 2010[85].

The Shiga toxin secreted by the bacterium *Shigella Dysenteriae* is also composed of an A-subunit responsible for the pathogenicity of the toxin and a B-subunit responsible for cellular attachment and intracellular trafficking. The B-subunit of the Shiga toxin, STxB, is a pentameric protein that can bind up to 15 copies of its glycolipid receptor Gb3 with affinities in the nM range[129] (in comparison to CTxB that binds to GM1 with affinities in the pM range[120]). The STxB was found to induce similar lipid clustering in membranes[84], which in turn generates lipid compression that favors membrane bending[130]. Upon clustering of the lipids and additional clustering of the toxin proteins themselves on the membrane due to fluctuation forces[131], membrane deformation can be realized. STxB bends the plasma membrane and form long, tubular invaginations filled with toxins, in both cells starved of energy and in model membrane systems[84,85]. STxB and CTxB employ similar mechanisms of membrane bending and internalization.

Bacterial toxin uptake occurs through both CME and CIE

Both CTxB and STxB were found to enter cells through both clathrin-dependent processes and through clathrin-independent processes[103,104]. The reason for employing both mechanisms is not clear; however, these toxins need to be trafficked through different intracellular compartments in order to efficiently infect cells. The differential sorting of the toxins might require specific transbilayer interactions that are realized through adaptor proteins, such as those involved in clathrin-mediated endocytosis. The exact mechanism leading the toxins to their destinations in the cytosol remains an open question in the field. The release of the endocytic vesicles filled with CTxB or STxB occurs mostly in a dynamin-dependent way, however it is not the only responsible factor for scission. Rather, there is a concerted action between dynamin, cholesterol-dependent line tension in the bilayer and actin polymerization[88].

Open questions in toxin and virus membrane deformation and uptake

Even though the SV40 and CTxB do not share any sequence homology, both systems employ the same configuration of lipid-binding sites to promote their uptake into cells. These two otherwise unrelated systems must be subject to convergent evolution, as multivalent lipid binding is an absolute requirement for efficient infection of their hosts. It is still not clear how these pathogens generate the forces required to bend membranes, is multivalent lipid binding sufficient? It remains to be determined how the adhesion energy between these particles and the membrane influence membrane deformation and whether the induction of curvature is alone sufficient to trigger internalization. Moreover, most of these pathogens exhibit pleiotropic membrane binding behavior and bind to secondary receptors as well. The possibility that the secondary receptors play a role in facilitating membrane bending and/or internalization cannot be ruled out.

Chapter 1.4. Multivalent lipid binding in intracellular traffic

After exogenous cargo internalization in cells through endocytosis, downstream traffic is required to deliver the cargo to its final destination. Its destination depends on the type of cargo and generally, there can be only two major outcomes: 1) recycling back to the plasma membrane or 2) degradation in lysosomes. In the case of pathogens, the outcome of the intracellular traffic must be the completion of the infection pathway and the generation of new virions. For example, polyomaviruses must escape degradation and enter the ER where their outer capsids start to disassemble and fuse with ER membranes. From there, the virions are extracted to the cytosolic space and they release their inner genomic content into the nucleus. Nevertheless, before reaching their final destination, polyoma-virions need to be sorted through the correct organelle compartments. On the other hand, bacterial toxins pass through the Golgi apparatus on their way to the ER instead, probably to escape degradation in lysosomes.

Early endosomes: the sorting station of the cell

Immediately after endocytosis, the vesicles containing endocytic cargo fuse with early endosomal compartments, as they are the first sorting station of the cell. These endosomal structures are heterogeneous when it comes to size and shape and are generally formed by the fusion of many endocytosed vesicles. They reside at the periphery of the cells close to the plasma membrane. There are different early endosomal populations with different characteristics[132]. A fraction of early endosomes is decorated with Rab5 proteins, which are key regulators of the endosomal maturation process. There is another fraction of early endosomal compartments devoid of Rab5 effectors which form by the fusion of endocytic pits generated through the CLIC/GEEC pathway[93]. From early endosomes, cargo is either recycled back to the plasma membrane through recycling endosomes or it is retained in early endosomes for the following maturation steps into late endosomes. Pathogens generally traffic through endosomal compartments on their way to the ER. After internalization, the endocytic vesicles containing the pathogens fuse with either Rab5-positive early endosomes for the particles internalized through CME or Rab5-negative early endosomes in the case of pathogens internalized through clathrin-independent endocytosis. While CTxB and STxB have been found to colocalize well with Rab5-positive vesicles[133,134], the SV40 virus does not significantly colocalize to these compartments[135]. The fusion between the toxins or virion with different early endosomal species might be a consequence of the endocytic mechanisms employed. The virus enters without the aid of coat proteins such as clathrin or caveolin, however the toxins enter through both CME and CIE. After fusion with early endosomes (devoid of Rab5), SV40 remains in these compartments as they mature into late endosomes and fuse with lysosomes (**Figure 1.10**)[135]. On the other hand, the toxins are sorted directly to the Golgi apparatus (**Figure 1.10**)[133,134].

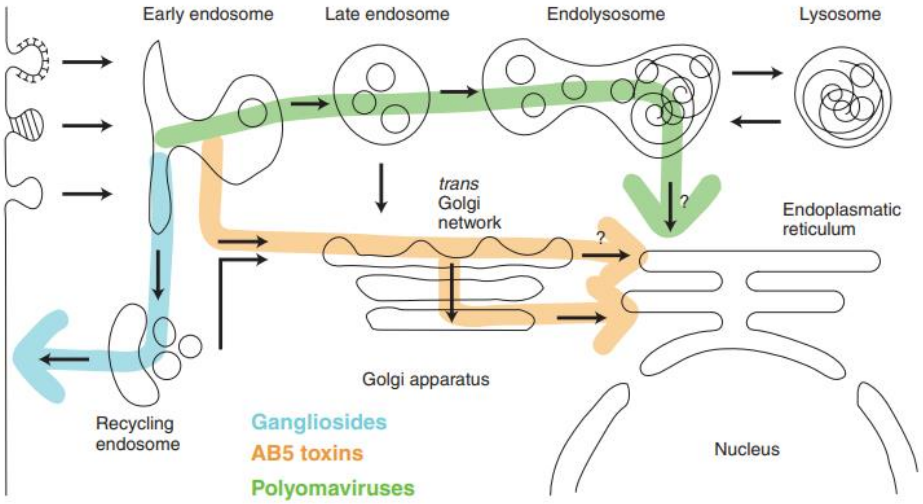

Figure 1.10. The intracellular trafficking pathways of pathogens and their receptors. The SV40 polyomavirus intracellular pathway is shown in green, the bacterial toxin intracellular sorting through the Golgi is shown in orange and the recycling of their lipid receptors back to the plasma membrane is shown in blue. Reproduced with permission from Ewers and Helenius, CSH Perspectives in Biology, 2011.

The endo-lysosomal pathway

As early endosomes start to mature into late endosomes, they are transported closer to the nuclear region and their intraluminal pH drops due to the accumulation of acid hydrolases in their lumen. The Rab5 GTPase recruits Rab7 on the membrane of late endosomes. Ultimately, late endosomes will fuse with lysosomes, which are dense, acidic compartments formed through the fusion of phagosomes, autophagosomes and macropinosomes. They are the degradative station of the cell and have a high hydrolase content.

Pathogens such as SV40 are sorted through the endo-lysosomal pathway on their way to the ER where they complete the infection of the host cells (**Figure 1.10**). The capsids of the virions survive the acidic environment of lysosomes, but conformation changes do occur, which facilitate their disassembly during the next trafficking steps. It remains unclear at which point are the polyoma-virions sorted to lysosomes during their intracellular traffic. It could take place already at the plasma membrane level, where the binding to certain lipid species triggers lipid clustering and nanodomain formation in the membrane. In addition to facilitating the formation and the scission of pathogen-filled endocytic pits, lipid clustering by multivalent binding virions induces signal transduction in the cells. In the case of SV40, tyrosine and other kinases become activated[136,137] upon binding and are crucial for the effective infection of the cells. Most likely, the signalling pathways activated by the binding of these pathogens are involved in their subsequent targeting to the ER. However, the sorting of the virions through lysosomal compartments could also occur at the early endosomal level since these pathogens enter cells through clathrin-independent endocytosis and fuse with

early endosomes devoid of Rab5 effectors. This subset of early endosomes could be enriched in other proteins that are involved in the targeting of certain intracellular compartments. More research into these mechanisms is needed to understand the mediators of the sorting of virions in lysosomes.

The Golgi apparatus

There is a constant exchange of vesicles always taking place between endosomal compartments and the trans-Golgi network. As this is a bidirectional pathway, vesicles emerging from endosomes fuse with the Golgi and vice versa. Vesicles originating in the early endosomes are targeted to the Golgi through an enrichment in certain proteins in their membranes, such as the retromer protein complex. The retromer complex is composed out of sorting nexins and Vsp proteins that assemble on the cytosolic side of the early endosomal membrane. Often, the retromer complex is used to sort the acid hydrolase receptors to the trans-Golgi network[138]. Strikingly, the bacterial toxins are sorted to the Golgi apparatus instead of lysosomes, and from there they move on to the ER to complete the intoxication of the cells (**Figure 1.10**). The retromer complex has been suggested to be involved in mediating this trafficking pathway[139,140]. Cholesterol is also required for correct sorting of the toxins to the Golgi apparatus[141] as well as the long acyl chains of their lipid receptors[142].

Lipid receptor recycling to the plasma membrane

As the acidification of the lumen of early endosomes triggers the release of the receptors bound to either the polyoma-virions or the bacterial toxins, the lipids become rapidly recycled back to the plasma membrane. The recycling of receptors allows for regulation of infection by these pathogens. For example, when the acidification of the intra-endosomal space is inhibited, the receptors are not recycled back to the plasma membrane and their availability for new virions or toxins to bind to drops significantly. As a result, infection of cells by pathogens is reduced under these conditions[135].

Open questions in toxin and virus intracellular traffic

It remains to be determined what causes the differential sorting of SV40 and the bacterial toxins through the intracellular space. The virions have a globular multivalent arrangement of binding sites while the toxins have fewer binding sites on a rather flat disc shape configuration. It might be the specific architecture of the multivalent lipid binding sites that clusters the receptors in a specific manner and triggers the activation of certain signalling pathways. The different signalling pathways activated by toxins and the polyomaviruses could direct them one way or the other in the intracellular space but remains to be determined.

Chapter 1.5. Aim of this thesis

Glycolipid-binding bacterial toxins and viruses can induce membrane curvature by multivalent lipid binding. The SV40 polyomavirus and the structurally unrelated CTxB bind their ganglioside receptor GM1 in a pentavalent configuration and trigger the formation of long, tubular invaginations in energy-depleted cells and in model membrane systems or become directly internalized in regular cells[17,18]. This suggests that multivalent glycolipid binding alone is sufficient to trigger clathrin-independent endocytosis. However, it remains unclear whether 1) this is a generic, global mechanism and 2) how multivalent binding and receptor affinity control membrane deformation and internalization. The first aim of this thesis is to investigate whether membrane deformation induced by multivalent lipid binding is common among the members of the polyomavirus family. More importantly, the work in this thesis aims to determine if this is a general biophysical mechanism in cell biology that can be employed by other multivalent lipid-binding mimics to trigger their cellular uptake. The main hurdle in addressing this question is the lack of a tractable experimental system that reproduces the architecture of binding sites of polyoma-virions but excludes the possibility of pleiotropic membrane binding behavior observed for these virions. Can such a system be designed and built? Can it provide a glimpse into the generality of the multivalent-binding induced, clathrin-independent endocytosis mechanism? Could it be expanded further to investigate the contribution of other biophysical parameters in endocytosis? All these questions are addressed in the first results and discussion chapter of this thesis.

In the second chapter of this work, I investigated the intracellular trafficking of non-enveloped, tumour-causing viruses and bacterial toxins. Polyomaviruses have a globular arrangement of lipid-binding sites and become trafficked through the endo-lysosomal system on their way to the ER. In contrast, bacterial toxins have a flat arrangement of lipid binding sites and become trafficked through the Golgi apparatus on their way to the ER. An important open question here that remains to be answered is how do these pathogens become transported through different pathways inside the cells? Is the particular arrangement of multivalent lipid binding sites responsible for their differential sorting? And finally, could this sorting be reproduced using artificial viral and toxin mimics in order to determine the minimal requirements for lysosomal or Golgi targeting by exogeneous cargo? All these questions are addressed in the second results and discussion chapter or this thesis.

Chapter 2. Results and discussion

Chapter 2.1. Adhesion energy mediated endocytosis triggered by multivalent-lipid-binding

Non-enveloped, tumour-causing viruses such as the Simian Virus 40 are able to infect cells by making use of the limited resources they have at hand, namely the structure of their capsid. The viral capsids are composed of pentameric proteins that bind multivalently to lipids anchored in the external leaflet of the plasma membrane. Through strong avidity resulting from multivalent lipid binding, the virions generate enough energy to bend membranes into an endocytic pit. This induced membrane curvature ultimately leads to the internalization of the virions in a clathrin- and caveolin-independent manner. In this chapter, I first asked whether the interaction between multivalent lipid-binding globular particles and membranes is a common biophysical mechanism employed by all the members of the polyomavirus family to penetrate cells. Next, I investigate whether multivalent lipid binding in a globular configuration could generally induce membrane deformation and clathrin-independent endocytosis.

Chapter 2.1.1. Polyomaviruses employ multivalent lipid binding for membrane deformation and uptake

To understand whether multivalent lipid binding is a common biophysical principle that non-enveloped viruses can exploit to infect cells, I made use of several members of the polyomavirus family to check for similarities in their endocytosis behavior. To do that, I assembled virus-like-particles (VLPs) from the VP1 major structural capsid proteins of the SV40 virus, JC polyomavirus (JCPyV) and mouse polyomavirus (mPyV) (**Figure 2.1**A). These particles are known to bind to different glycolipid moieties on the external leaflet of the plasma membrane, namely SV40 binds to GM1, JCPyV binds to GD1b and mPyV binds to the GD1a and GT1b gangliosides, respectively.

Note: all the assembled VLPs used in this thesis are not infectious agents since they are composed out of the capsid proteins alone and lack any genomic content. All the work in this thesis (also in the next chapter of Results) was performed using such non-infectious VLPs. The artificial virus-like-particles created in the subsequent sections are non-infectious as well.

First, I verified the monodispersity of the assembled VLPs by performing live-cell time-course assays on a spinning disk microscope. I observed all the polyoma VLPs binding as discreet spots onto cellular membrane and diffusing laterally before becoming immobile (**Figure 2.1**B).

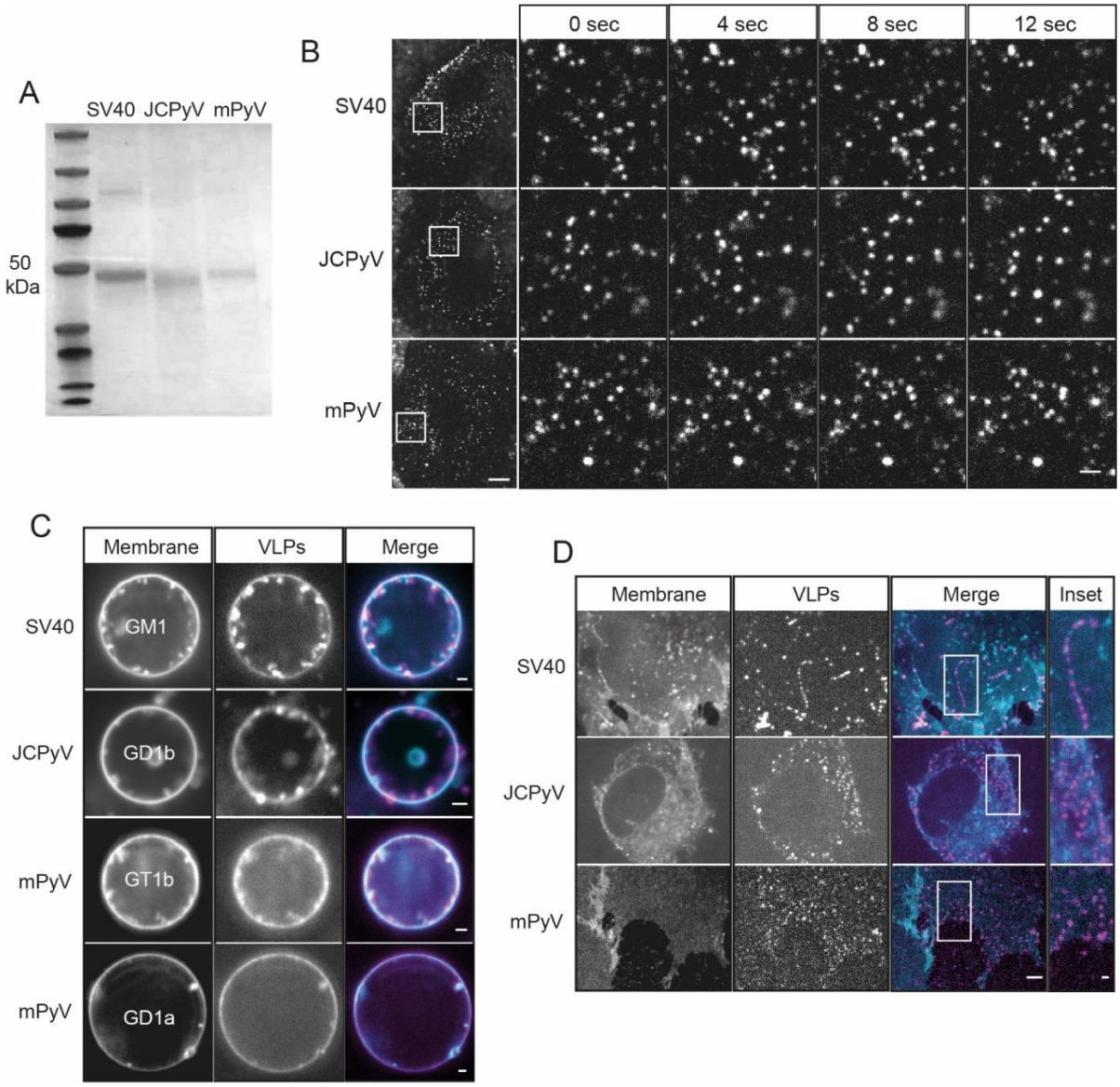

Figure 2.1. Polyoma-virions share a common biophysical mechanism of membrane-deformation based on multivalent lipid binding. A) SDS-Page gel showing the single capsid protein composition of the commercial polyoma VLPs. **B)** Fluorescence micrographs of polyoma VLP binding to the membrane of CV1 cells for 30 min at at 4 ˚C before imaging live on a spinning disk confocal microscope at 37 ˚C. Left panels: overview of the cells with bound VLPs as indicated. Scale bar is 10 µm. Right panels: time-course fluorescence micrograph insets of the regions of interest indicated in the left panels for the respective polyoma VLPs diffusing on the membrane. Scale bar is 2 µm. **C)** Spinning disc confocal fluorescence microscopy micrographs of polyomavirus-like particles (VLPs) bound to Giant unilamellar vesicles (GUVs) containing receptor gangliosides. 2 µg of each VLP was incubated for 1 h at RT with GUVs containing the indicated gangliosides (98% DOPC, 1% ganglioside, 1% β-BODIPY FL C12-HPC dye) and imaged at the equatorial plane. Scale bar is 2 µm. **D)** Spinning disc confocal fluorescence microscopy micrographs of polyomavirus-like particles (VLPs) bound to energy-depleted CV1 cells. Cells were starved of cellular energy by 30

min incubation in starvation buffer ($PBS^{+/+}$ supplemented with 10 mM 2-deoxy-D-glucose and 10 mM NaN_3) followed by 1 h incubation with 5 µg of each VLP in starvation buffer and imaged live on a spinning disk confocal microscope. DiI membrane dye was added 10 min prior to imaging at 1 mg/ml final concentration. Scale bars are 5 µm and 1 µm for insets.

Secondly, I tested whether all the VLPs could deform membranes by multivalent lipid binding alone, without the aid of cellular machinery. For this, master student Kita Schmidt and I made use of an *in vitro* model membrane system composed out of a bilayer bubble with minimal lipidic components, called Giant Unilamellar Vesicles (GUVs), that do not contain any proteins in their membrane or in their lumen. These vesicles were composed of phospholipids (DOPC), a membrane dye (BODIPY) and the indicated gangliosides **Figure 2.1**C). We found that all three polyoma VLPs could induce the formation of long, tubular structures filled with virions that emanate towards the intralumenal space of the GUVs (**Figure 2.1**C). Next, I investigated whether polyoma VLPs could also deform the membranes of cells into such tubular structures. To enable the formation and visualization of such long invaginations filled with viruses, the rapid scission of the nascent endocytic vesicles created in the plasma membrane had to be blocked. I blocked active cellular processes such as actin polymerization and the action of mechanoenzymes such as dynamin by starving the cells of energy. The cells were subjected to metabolic treatment using sodium azide and a non-metabolizable glucose analog, 2-Deoxy-D-Glucose for 20 minutes prior to the addition of the VLPs. After 1 hour of incubation of the cell with the VLPs in energy-depletion medium, I observed the formation of long, tubular invaginations filled with VLPs extending from the membrane towards the cytosol (**Figure 2.1**D), similar to the invaginations observed previously in the GUVs.

Further, to understand whether all polyoma VLPs become successfully endocytosed in cells, I needed to design and validate a high-throughput quantitative endocytosis assay. This assay allowed for a comparison between the amount of VLPs internalized into cells after 1 hour at 37 ˚C in comparison to the amount of particles internalized in cells after 1 hour at 4 ˚C (**Figure 2.2**A and B). When cells are kept at 4 ˚C, endocytosis does not occur and the uptake of any exogeneous cargo is inhibited[19]. Moreover, in order to successfully quantify the internalized particle fraction alone, the particles that are merely bound to the external leaflet of the plasma membrane have to be removed prior to measurement. For this, the cells are washed with an acidic buffer (pH ~ 3) that efficiently causes the VLPs to release their receptors and detach from the plasma membrane. Control quantifications of the internalized VLP amount before and after this acidic buffer wash are shown in Annex 1. To perform high-throughput endocytosis assays, I measured the fluorescence intensity of the internalized VLPs in at least 5000 cells with flow cytometry and I quantified the percentage of cells containing the fluorescent VLPs from the total amount of cells in the sample (at least 10000). I observed that almost all cells contained internalized VLPs when incubated at 37 ˚C, however there was no internalized VLP fraction observed for cells incubated at 4 ˚C (**Figure 2.2**B).

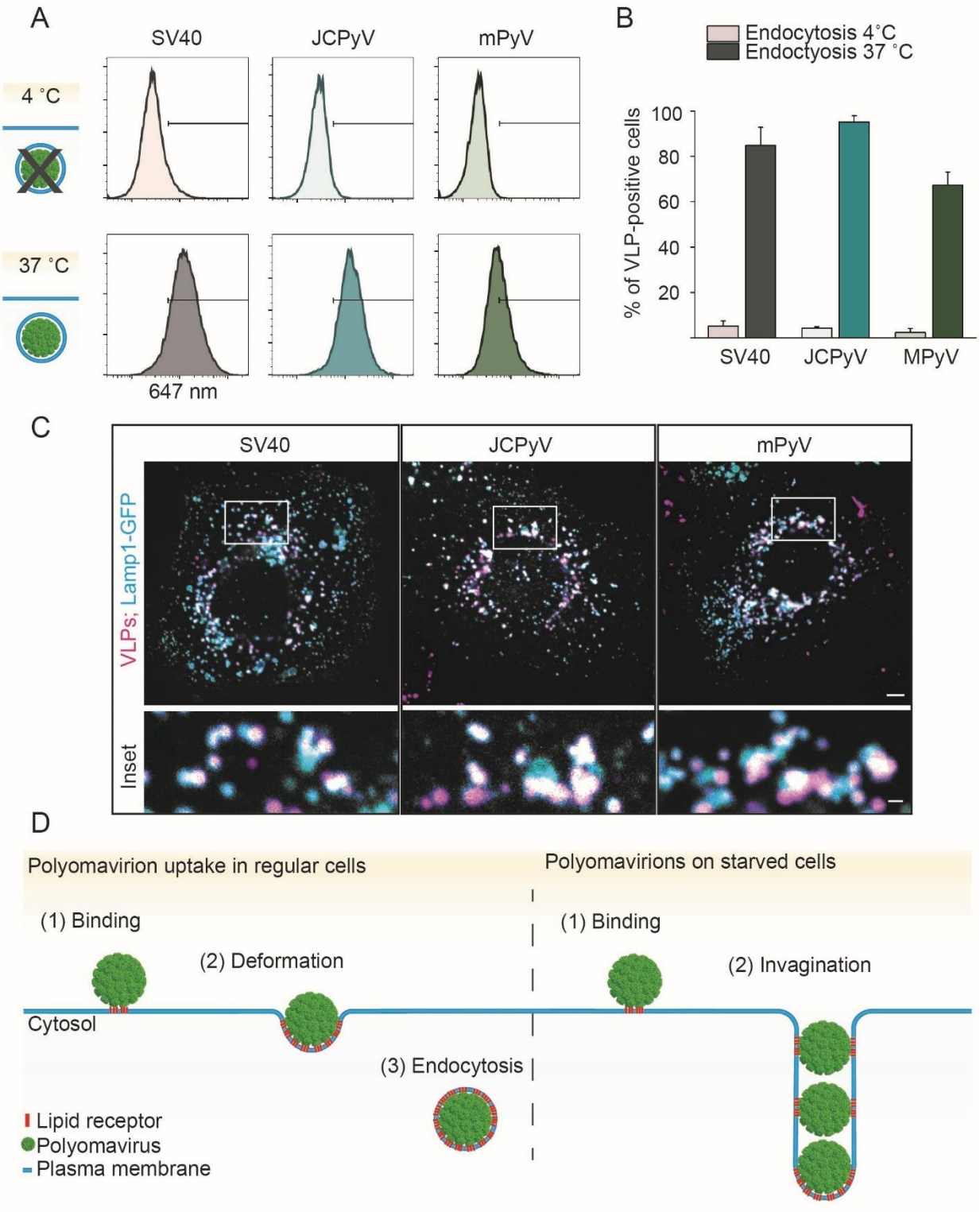

Figure 2.2. Polyoma-virions become internalized in cells. A) Histograms of of the mean fluorescence intensity values for the indicated VLP endocytosis in CV1 cells either at 4 ˚C (top panels) or at 37 ˚C (lower panels) as determined from flow cytometry measurements. Measured is intensity of at least 5000 cells/sample. **B)** Quantification of polyoma VLP endocytosis in CV1 cells either at 4 ˚C or at 37 ˚C from the flow cytometry measurements represented in A), means ± s.e.m., n = 2 independent experiments. **C)** Fluorescence micrographs showing the intracellular

localization of the VLPs in Lamp1-positive lysosomes. VLPs in magenta, Lamp1-GFP in cyan, positive colocalization becomes white. Scale bar is 10 µm and 1 µm for inset. **D)** Schematic illustration of the uptake process of polyoma VLPs in regular cells (left) and in energy-depleted cells (right). In energy-depleted cells, the VLPs trigger the formation of long tubular invaginations extending into the cytosol and do not become internalized.

To confirm that the VLPs are successfully internalized into the cells, I added them to cells expressing Lamp1-GFP, a lysosomal marker, incubated for 6 hours and visualized them with confocal fluorescence microscopy. I observed that the VLPs colocalize with Lamp1 as indicated by the white overlapping regions (**Figure 2.2**C), therefore confirming their uptake into cells.

Taken together, these results point out the existence of a common biophysical mechanism that polyomaviruses use to induce membrane deformation and this is an absolute requirement for internalization. I hypothesize it is sufficient for VLPs to bind to enough receptors on the membrane (**Figure 2.2**D, left panel, part (1)) and start imprinting their shape onto it, generating an endocytic pit (**Figure 2.2**D, left panel, part (2)) that then becomes internalized into the cell (**Figure 2.2**D, left panel, part (3)). If the cells are starved of energy and unable to perform basic cellular processes, these endocytic pits formed after VLP-binding will elongate into long tubular structures filled with particles (**Figure 2.2**D, right panel) and their uptake into cells will be inhibited.

Chapter 2.1.2. A synthetic virus-like-particle and lipid-receptor system to study endocytosis

I next aimed to understand if multivalent-lipid-binding triggered membrane deformation is a universal biophysical mechanism that globular particles can employ to mediate their uptake into cells or if it is exclusive for polyomaviruses. To this end, I made use of a synthetic cellular system, composed out of a virus-like-particle and a lipid-anchored receptor tailored for it. The synthetic globular VLP mimics the nanoscale molecular architecture of binding sites of polyoma VLPs and similarly binds to a lipidic receptor (**Figure 2.3**A). To build the synthetic VLP, I made use of the *encapsulin* protein originating from a virus-like-particle found in the archaeon *Pyrococcus furiosus*[143] to which a GFP molecule is genetically-linked. The GFP-encapsulin monomer then self-assembled into a 37-nm diameter, icosahedral genetically-encoded multimeric nanoparticle (GEM)[144] that exhibits 180 copies of GFP symmetrically distributed all over its surface (**Figure 2.3**A, **Annex 3.**A and B). A tailored high-yield purification procedure of the GEMs from *E.coli* was devised and is presented in **Annex 4.**

As a receptor for the GEMs, I incorporated a GFP-binding nanobody (LaG16)[145] into the external leaflet of the plasma membrane of cells by adding a GPI-anchor to its C-terminus (**Figure 2.3**A purple, **Annex 3.**C) and transiently expressing it in cells. Purified GEMs successfully bound to the membranes of cells

expressing the GPI-anchored anti-GFP nanobody and diffused laterally as discreet fluorescent spots (**Figure 2.3**B). I could inhibit the binding of the GEMs to these cells by pre-incubating the particles with recombinantly expressed anti-GFP nanobodies (LaG16) in a dose-dependent manner **Figure 2.3**C, D).

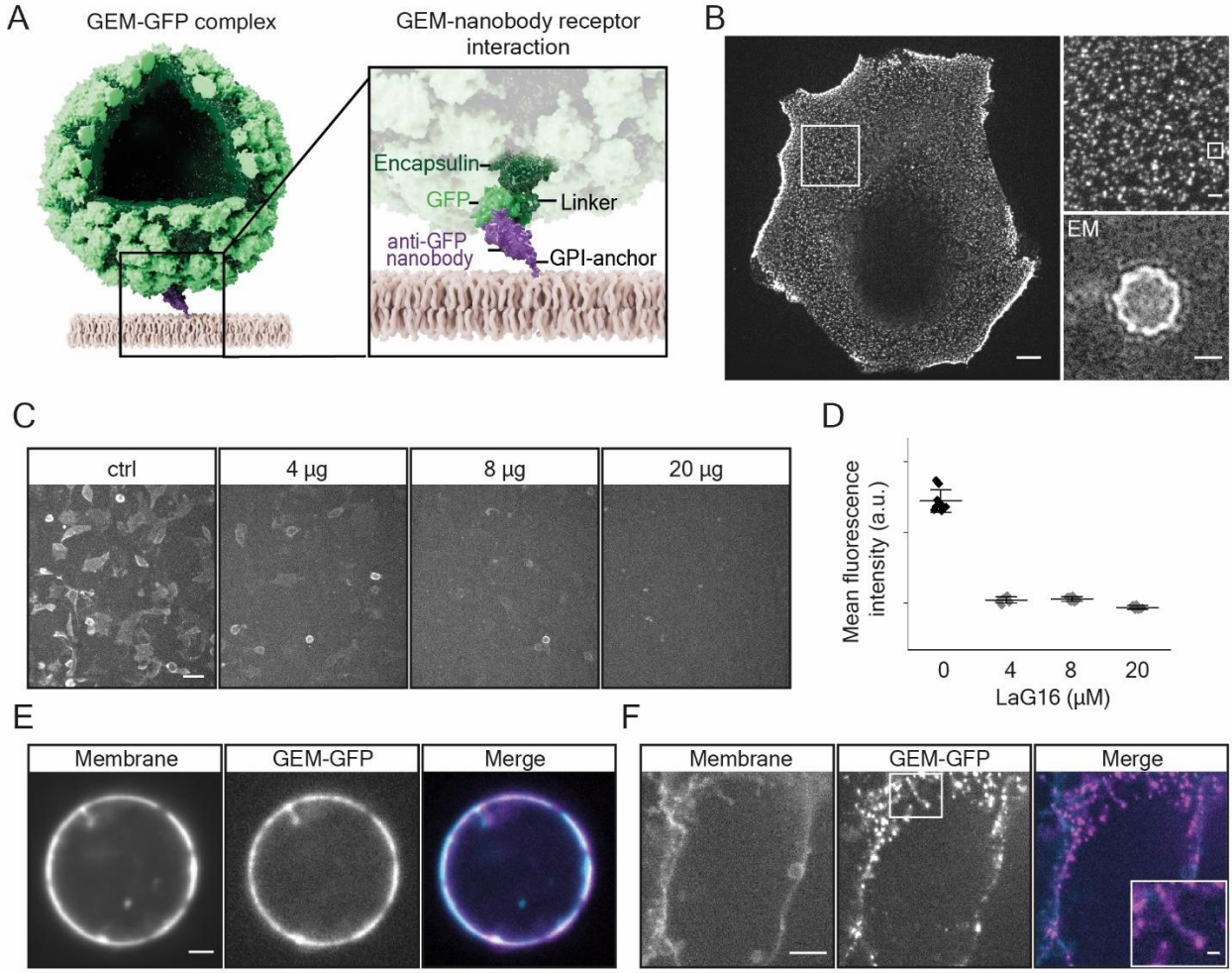

Figure 2.3. A polyvalent virus-like-particle lipidic-receptor system triggers membrane deformation. A) Schematic representation of the synthetic system. Shown is a genetically encoded nanoparticle (GEM) assembled from 180 copies of the *encapsulin* protein (dark green) coupled to GFP (light green). A GPI-anchored anti-GFP nanobody (purple) inserted into the membrane (beige) serves as receptor. **B)** Fluorescence micrograph of GEMs binding to the cell membrane of CV1 cells. Scale bar is 10 µm. Insets: (upper) magnified region of the GEM-GFP decorated membrane from the overview emphasizing monodisperse binding. A single particle is shown in the box. Scale bar is 2 µm. (lower) Transmission electron micrograph of purified GEM. Scale bar is 15 nm. **C)** Fluorescence micrographs of GEMs bound to the surface of the cells after pre-mixing with the indicated concentrations of recombinant LaG16 nanobody. Scale bar is 50 µm. **D)** Quantification of the fluorescence intensity of the micrographs represented in panel C), means ± s.e.m.. **E)** Fluorescence micrograph of GEMs bound to Giant Plasma Membrane Vesicles (GPMVs) of CV-1 cells expressing GPI-anchored nanobody. GPMVs were incubated with 0.45 nM GEMs for 1 h at RT before imaging at the equatorial plane on a spinning disk confocal microscope. Scale bar is 2 µm. **F)** Fluorescence micrograph of GEMs bound to energy-depleted CV1 cells expressing GPI-anchored anti-GFP nanobody that were starved of cellular energy by 30 min incubation in starvation buffer ($PBS^{+/+}$ supplemented with 10 mM 2-deoxy-D-glucose and 10 mM NaN_3) followed by 1 h incubation with 2 µg of purified GEMs in starvation buffer and imaged live on a spinning disk confocal microscope. DiI membrane dye was added 10 min prior to imaging at 1 mg/ml final concentration. Scale bars are 5 µm and 1 µm for the inset.

To ask whether the polyvalent globular lipid binders, GEMs, could indeed deform membranes without the aid of cellular machinery, master student Kita Valerie Schmidt generated an *in vitro* model membrane system composed out of giant plasma-membrane derived vesicles (GPMVs), that were vesiculated and isolated from CV1 cells expressing the GPI-anchored anti-GFP nanobody receptor. GEMs were added to the GPMVs and incubated for 1 hour at room temperature (RT). We observed that GEMs induced the formation of tubular membrane invaginations emanating towards the lumen of the GPMVs (**Figure 2.3**E). Next, I investigated whether the GEMs could deform the membranes of cells into longer tubules, similarly to the ones generated by the polyoma-virions. When I added the GEMs to cells starved of cellular energy by metabolic inhibitor treatment with sodium azide and 2-Deoxy-D-Glucose, I observed the formation of these long, tubular invaginations filled with GEMs extending from the plasma membrane into the cytosol (**Figure 2.3**F).

I then probed whether GEMs became successfully endocytosed into CV1 cells by performing live-cell pulse-chase assays using microscopy to track the intracellular localization of GEMs in a time-course experiment. In brief, I pre-incubated the cells at 4 ˚C for 10 min to stop endocytic processes from occurring, then added the GEMs and further incubated them at 4 ˚C for 30 min to allow the GEMs to bind. I then switched the cells to 37 ˚C to rescue endocytosis and imaged them live on a spinning disc confocal microscope at the indicated time points. I found that GEMs were exclusively localized on the plasma membrane immediately after the switch to 37 ˚C, but then became endocytosed after 1 h incubation at 37 ˚C based on their colocalization with Lamp1-mRFP decorated lysosomes (**Figure 2.4**A).

To further prove their internalization and understand the molecular mechanism behind it, I performed the quantitative endocytosis assays described in the previous section and measured the fluorescence intensity of the internalized GEMs in at least 5000 cells/sample with flow cytometry. In addition to verifying successful endocytosis, I aimed to determine the molecular players involved in the uptake process. Therefore, I pre-treated the cells with inhibitors of certain endocytic factors and compared the GEM endocytosis in the cells with and without treatment (**Figure 2.4**B). To validate the efficiency of the inhibitors used, I also tested the uptake of positive control proteins, such as SV40 or Tf. I found that when Clathrin Heavy Chain was knocked down using an siRNA genetic inhibitor or when the activity of dynamin was suppressed by expressing a dominant-negative variant of the protein, the uptake of Tf, a well-known CME cargo, was significantly reduced. However, GEM endocytosis did not show a major reduction, indicating an independence of clathrin- or dynamin-mediated processes for uptake (**Figure 2.4**B). When I removed membrane cholesterol by pre-treating cells overnight with Nystatin and Progesterone or when I inhibited endosomal acidification by treating the cells with the BafilomycinA drug, I observed a significant decrease in SV40 uptake, which is known to be highly dependent on cholesterol and endosomal acidification[135].

However, I did not observe a major reduction in GEM endocytosis, suggesting that neither cholesterol, nor an endosomal drop in pH are required for GEM uptake (**Figure 2.4**B).

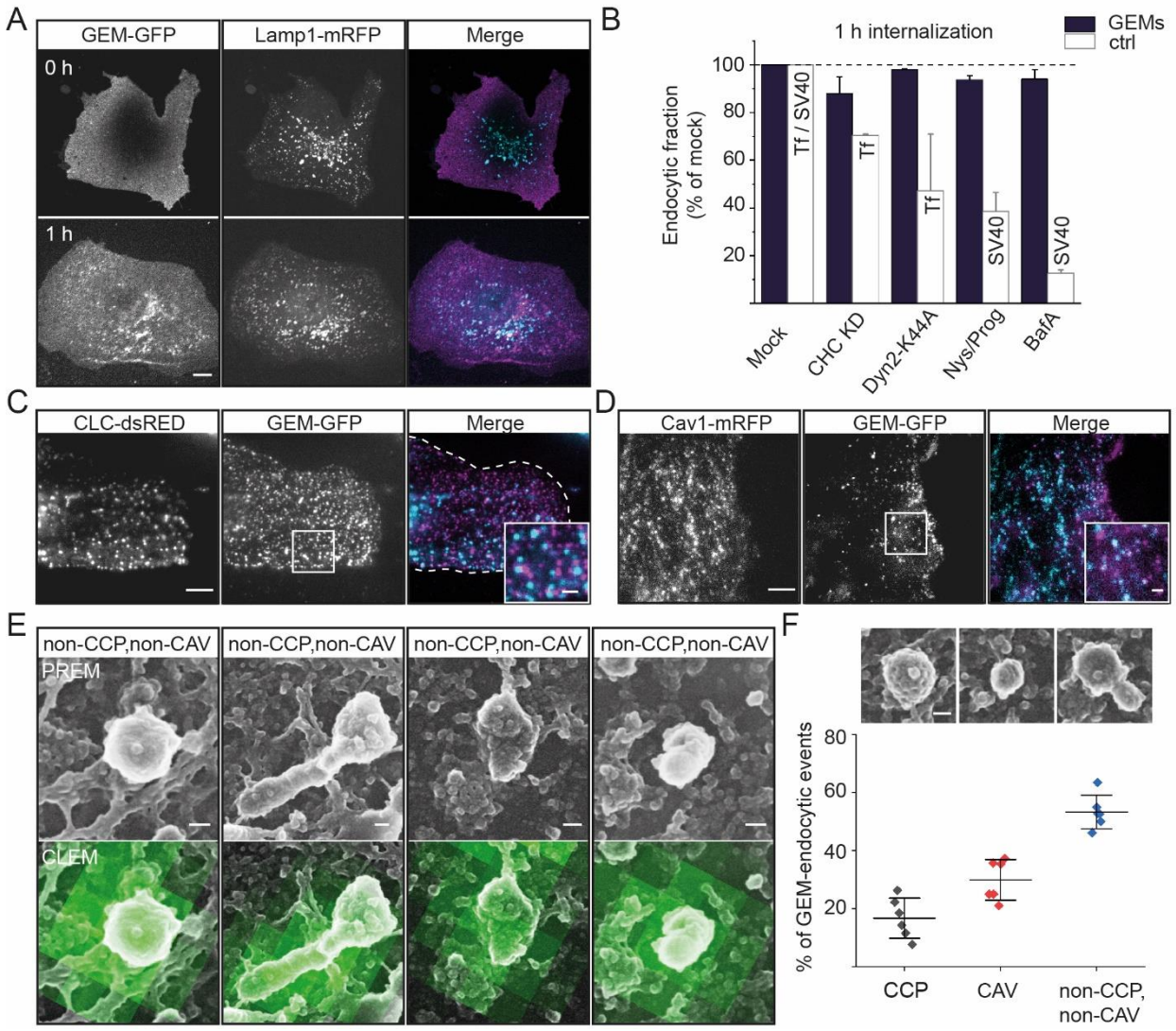

Figure 2.4. The endocytic mechanism of artificial polyvalent globular binders. A) Fluorescence micrographs from a time-course experiments of endocytosis showing the distribution of GEMs in CV1 cells expressing anti-GFP nanobody and Lamp1-mRFP. Cells were incubated with 2 µg of GEMs for the indicated time points at 37 ˚C before live imaging on a spinning disk confocal microscope. Scale bars are 10 µm. **B)** Quantification of GEM endocytosis upon treatment with genetic (siRNA against clathrin-heavy-chain and expression of dominant negative Dyn2-K44A) or chemical inhibitors (Nystatin/Progesterone and BafilomycinA) as compared to mock treatment. Mean fluorescence intensity ± s.e.m was determined from flow cytometry measurements for at least 5000 cells/sample, n = 2 independent experiments. **C)** Fluorescence micrograph of GEMs bound to CV1-cells expressing Clathrin-light-chain-dsRED incubated for 10 min with 2 µg of GEMs before live imaging on a TIRF microscope. Scale bars are 5 µm and 1 µm for inset. **D)** Fluorescence micrograph of GEMs bound to CV1-cells expressing Caveolin-1-mRFP incubated for 10 min with 2 µg of GEMs before live imaging on a TIRF microscope. Scale bars are 5 µm and 1 µm for inset. **E)** Correlative fluorescence, platinum-replica electron microscopy micrographs of plasma membrane sheets generated after unroofing of cells incubated with GEMs. Shown are plasma membrane structures colocalizing with GEMs bound to the outside of cells that are neither positive for clathrin (as shown by antibody-staining) nor caveolin (as estimated from the ultrastructure). Scale bars are 50 nm. Electron microscopy micrographs are on top, same field of view with correlative

GFP fluorescence of the GEMs at the bottom. **F)** Top: Example platinum replica electron microscopy micrographs of a typical clathrin-coated pit, caveola and clathrin/caveolin double-negative invagination. Bottom: Quantification of colocalization of GEM fluorescence with endocytic structures. Means ± s.e.m. for 6 cells from n = 3 independent experiments. Scale bar is 50 nm.

To precisely understand the nature of the GEM endocytic process, I performed live-cell colocalization assays between GEMs and either Clathrin Light Chain-dsRed (CLC-dsRED) or Caveolin1-mRFP (Cav1-mRFP) on a Total Internal Reflection Fluorescence (TIRF) microscope. I found that the GEMs did not significantly colocalize with either of these endocytic markers, suggesting that they employ a clathrin- and caveolin-independent endocytic mechanism instead (**Figure 2.4**C, D). Furthermore, to verify that the main entry pathway of the GEMs does not rely on scaffolding proteins from the cytosol, collaborators Dr. Paul Markus Müller and Dr. Dymtro Puchkov performed correlative platinum-replica electron microscopy experiments on unroofed cells where they could visualize the GEM endocytic events occurring at the plasma membrane with high resolution. The fluorescence signal of the GEMs revealed their precise location and the nm-resolution electron microscopy imaging revealed the nature of the endocytic pits containing the GEMs. We found that the majority of the GEMs colocalized with structures devoid of both clathrin and caveolin, while a small fraction of GEM endocytic events did exhibit a caveolin pattern on top and almost no GEMs colocalized with clathrin-positive structures (**Figure 2.4**E, F).

Taken together, these results point out that an artificial polyvalent globular binder mimicking the organization of binding sites of non-enveloped virions is able to induce membrane deformation and it mediates its uptake via a clathrin-independent mechanism.

Chapter 2.1.3. Adhesion energy mediates membrane deformation by polyvalent, globular lipid-binders

To expand our understanding of the biophysics behind the endocytic mechanism employed by the GEMs and the role of the adhesion energy between the particle and the plasma membrane, I created a panel of 7 different lipid-anchored anti-GFP nanobody receptors with individual binding affinities ranging from the µM to the pM range (**Figure 2.5**A and **Table 2.1**). I verified their successful incorporation into the extracellular leaflet of the plasma membrane by adding purified EGFP to cells transiently expressing the panel of GPI-anchored anti-GFP nanobodies. In brief, the cells were preincubated for 10 min at 4 ˚C to stop endocytosis and further incubated with EGFP for 30-minute at 4 ˚C before imaging live on a spinning disk confocal microscope. I observed that EGFP successfully bound to the membrane of these cells and that the amount of binding scaled with the binding affinity of the lipidic receptors (**Figure 2.5**B, D). Next, I added

GEMs to cells expressing the panel of lipidic nanobody receptors and observed a similar affinity-dependent binding pattern (**Figure 2.5**C, E). Strikingly, the GEM binding levels on the two lowest affinity samples were close to the threshold values of GEM binding to non-transfected cells (**Figure 2.5**E), suggesting that the avidity of multivalent binding particles alone might not be sufficient to promote efficient receptor binding.

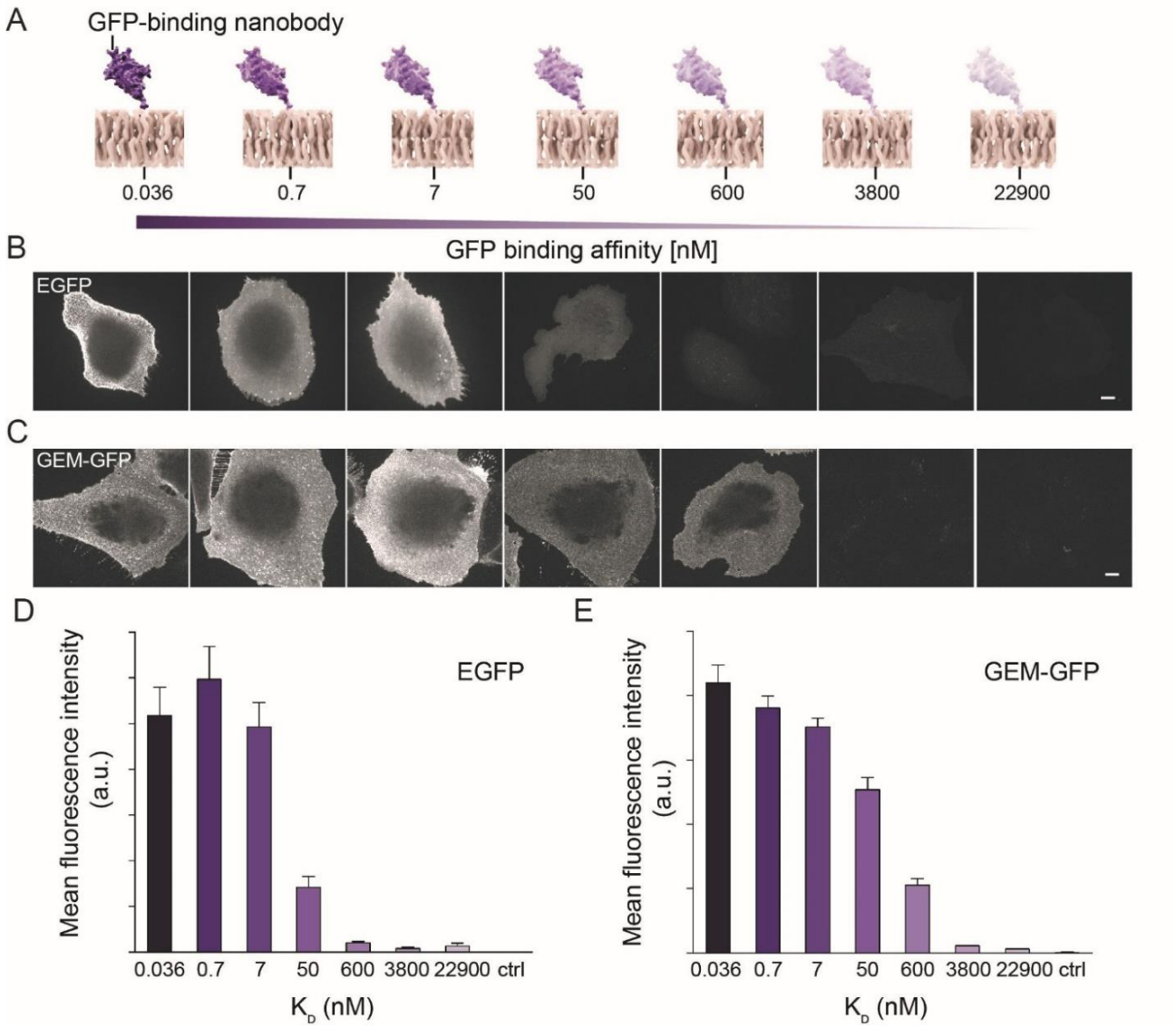

Figure 2.5. An artificial system tailored for the study of adhesion energy mediated endocytosis. A) Schematic representation of GPI-anchored nanobody constructs with decreasing binding affinity expressed in the outer membrane of cells used in this study. **B)** Fluorescence micrographs of recombinant EGFP binding and **C)** GEM binding to the membranes of CV1 cells expressing the panel of GPI-anchored anti-GFP nanobodies. Cells were incubated with 2 µg of either GEMs or EGFP for 30 min at 4 ˚C before imaging live on a spinning disk confocal microscope. Scale bar is 10 µm. **D)** Quantification of EGFP binding in dependence of receptor affinity as determined from the fluorescence micrographs represented in panel B). **E)** Quantification of GEMs binding in dependence of receptor affinity as determined from the fluorescence micrographs represented in panel C). Shown are means ± s.e.m., n = 2 independent experiments.

Table 2.1. GFP-binding nanobodies used in this study and their characteristics[145].

Construct name	K_D (nM)*	MW (Da)	Amino acid sequence**
LaG16-G_4S-LaG2	0.036[a]	30,791	MAQVQLVESGGRLVQAGDSLRLSCAASGRTFSTSAMAWFRQAPG REREFVAAITWTVGNTILGDSVKGRFTISRDRAKNTVDLQMDNLE PEDTAVYYCSARSRGYVLSVLRSVDSYDYWGQGTQVTVSGGGGS MAQVQLVESGGGLVQAGGSLRLSCAASGRTFSNYAMGWFRQAP GKEREFVAAISWTGVSTYYADSVKGRFTISRDNDKNTVYVQMNS LIPEDTAIYYCAAVRARSFSDTYSRVNEYDYWGQGTQVTV
LaG16	0.7[a]	16,306	MAQVQLVESGGRLVQAGDSLRLSCAASGRTFSTSAMAWFRQAPG REREFVAAITWTVGNTILGDSVKGRFTISRDRAKNTVDLQMDNLE PEDTAVYYCSARSRGYVLSVLRSVDSYDYWGQGTQVTVS
LaG21	7[a]	15,452	MAQVQLVESGGGLVQAGGSLRLSCAASGPTGAMAWFRQAPGME REFVGGISGSETDTYYADFVKGRLTVDRDNVKNTVDLQMNSLKP EDTAVYYCAARRRVTLFTSRADYDFWGQGTQVTVS
LaG17	50[a]	15,823	MADVQLVESGGGLVQAGGSLRLSCAASGRTISMAAMSWFRQAPG KEREFVAGISRSAGSAVHADSVKGRFTISRDNTKNTLYLQMNSLK AEDTAVYYCAVRTSGFFGSIPRTGTAFDYWGQGTQVTVS
LaG42	600[a]	15,490	MADVQLVESGGGLVQAGDSLRLSCAASGPTGAMAWFHQGLGKE REFVGGISPSGDNIYYADSVKGRFTIDRDNAKNTVSLQMNSLKPED MGVYYCAARRRVTLFTSRTDYEFWGRGTQVTVS
LaG18	3,600[b]	16,459	MAQVQLVESGGGLVQTGGSLKLSCTASVRTLSYYHVGWFRQAPG KEREFVAGIHRSGESTFYADSVKGRFTISRDNAKNTVHLQMNSLK PEDTAVYYCAQRVRGFFGPLRSTPSWYDYWGQGTQVTVS
LaG11	22,900[b]	16,221	MADVQLVESGGRSVRAGDSLRLSCLASGGTFSLYAMGWFRQAPG KEREFVAAVTWSGGSTYYTDSVKGRFSISRDNAKNTVYLQMNSL KPEDTAVYYCAVRTSGFFGSIPVTERAFDYWGQGTQVTVS

*K_D values were determined by either Surface Plasmon Resonance (marked with [a]) or by bead binding assays (marked with [b]) in the original study. **Sequences were codon-optimized for mammalian expression systems prior to cloning. These sequences were then subcloned into a pEGFP-N1 vector containing a GPI-anchor sequence.

Moving forward, I investigated how the modulation of adhesion energy between the GEMs and their lipidic receptors affected the membrane deformation process. To do this, master student Kita Valerie Schmidt generated Giant Plasma-Membrane derived Vesicles (GPMVs), that were vesiculated and isolated from CV1 cells expressing the panel of the GPI-anchored anti-GFP nanobody receptors. She then added the GEMs to each of these samples and incubated them for 1 hour at RT. We found that the particles were able to successfully induce the formation of tubular invaginations filled with GEMs only for the four highest-binding affinity receptors (**Figure 2.6**A). Then, I proceeded to check if the same behavior is reproducible in cells starved of energy. When I added GEMs to cells under metabolic inhibitor treatment to deplete their energy, I observed membrane deformation occurring for the five highest-binding affinity receptors (**Figure 2.6**B). In addition, once membrane tubulation by multivalent lipid binding of GEMs occurs, I observed that there is a similar probability of formation of such GEM-filled membrane invaginations throughout all the panel of GPI-anchored anti-GFP nanobodies for both *in vitro* membranes and in cells (**Table 2.2**). The main reason why

tubular structures were not observed for the fifth highest-binding affinity receptors in the GPMV experiments is the low concentration of the GEM particles used to perform the assay.

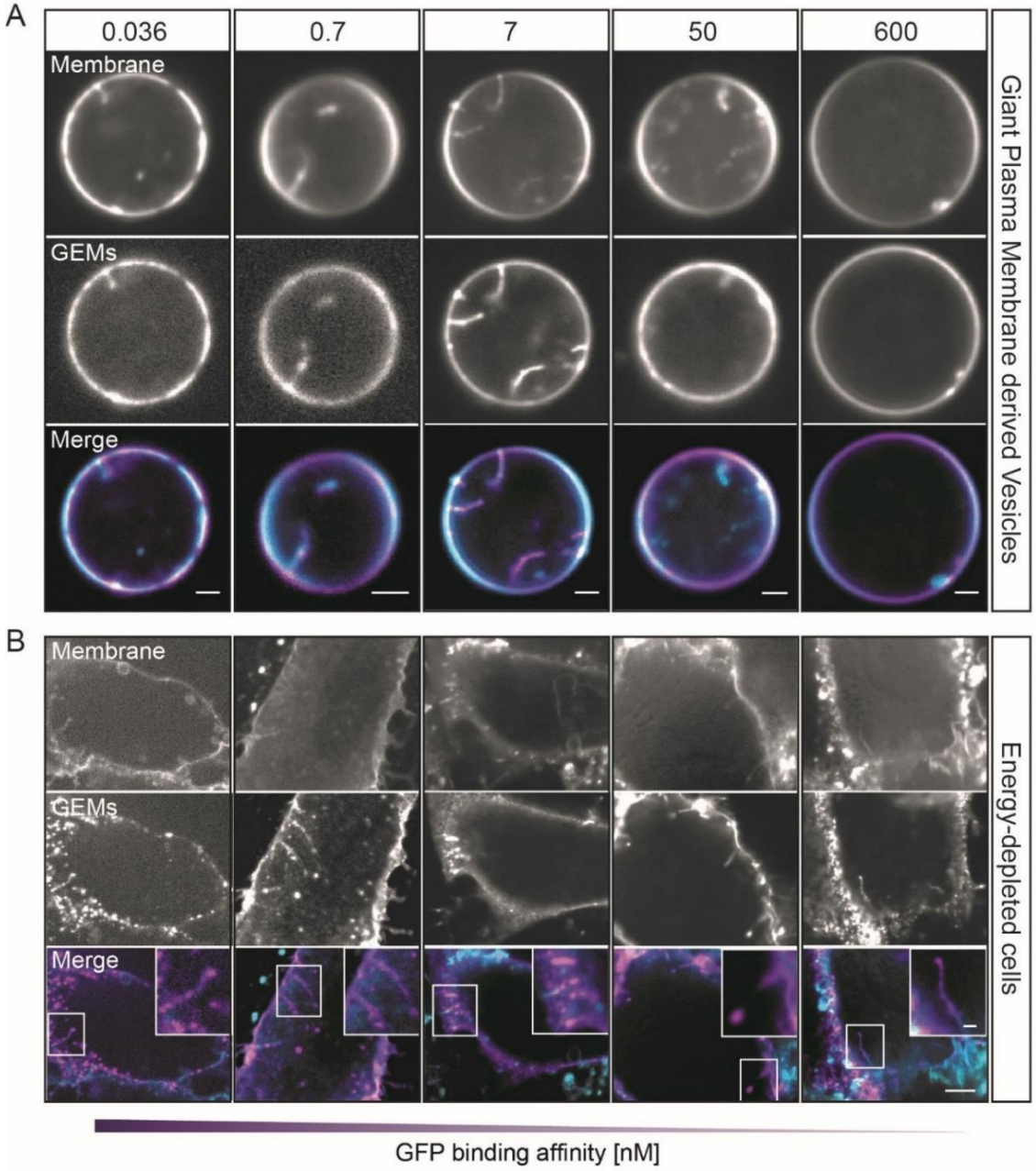

Figure 2.6. Adhesion energy mediated membrane deformation. A) Fluorescence micrographs of GEMs bound to GPMVs harvested from CV1 cells expressing the panel of GPI-anchored anti-GFP nanobody constructs as indicated, incubated with 0.45 nM GEM-GFP particles for 1 h at RT before imaging at the equatorial plane on a spinning disk confocal microscope. Scale bars are 2 μm. **B)** Fluorescence micrographs of GEMs bound to energy-depleted CV-1 cells expressing the panel of GPI-anchored anti-GFP nanobodies. CV1 cells were starved of cellular energy by 30 min incubation at 37 ˚C in starvation buffer ($PBS^{+/+}$ supplemented with 10 2-deoxy-D-glucose and 10 mM NaN_3) followed by 1 h incubation with 2 nM of GEM-GFP particles in starvation buffer at 37 ˚C and imaged live on a spinning disk confocal microscope. DiI membrane dye was added 10 min prior to imaging at 1 mg/ml final concentration. Scale bars are 5 μm and 1 μm for insets.

These results point out the existence of a threshold in the adhesion energy necessary to deform membranes by multivalent lipid binders and that this process rather occurs is a yes-or-no manner once this threshold is met instead of increasing in a stepwise manner with the binding affinity of the receptors.

Table 2.2. The percentages of energy-depleted cells and GPMVs containing GEM-filled tubular invaginations from the total number of cells/GPMVs.

K_D (nM)	Cells	GPMVs
0.036	24%	6%
0.7	25%	2%
7	25%	3%
50	19%	1%
600	20%	-
3,600	-	-
22,900	-	-

Chapter 2.1.4. Endocytosis of polyvalent, globular lipid-binders requires a threshold adhesion energy

In order to investigate the role of the adhesion energy in the endocytosis of multivalent lipid binding particles, I probed the endocytosis of the GEM particles in cells expressing the panel of the 7 different binding affinity receptors. I performed the same quantitative endocytosis assays described previously using flow cytometry. In brief, CV1 cells were first transfected with the panel of the GPI-anchored anti-GFP nanobodies and co-transfected with a cytosolic RFP marker. The next day, GEMs were added to these cells and incubated for 1 hour at 37 ˚C before acid stripping of the membrane-bound GEM fraction. The GFP fluorescence intensity of the internalized GEM fraction in these cells was measured using flow cytometry. The gating strategy employed for the flow cytometry measurements is exemplified and explained in detail in **Annex 2.**

First, I observed that all samples had similar levels of RFP expression, indicating a low variability in the protein expression levels of the transfected constructs (**Figure 2.7**A and B). Next, I found that both the percentage of cells containing internalized GEMs out of the total number of cells and the amount of endocytosed GEMs directly scaled with the binding affinity of the receptors. Interestingly, the fluorescence intensity of the internalized GEMs in the two lowest binding affinity samples was close to the values of the GFP-negative control sample, suggesting that efficient endocytosis does not occur in these cases (**Figure**

2.7A, C and D). These results further confirm the existence of a minimum threshold value for the adhesion energy between pentavalent, globular particles and their lipidic receptors that allows for particle uptake.

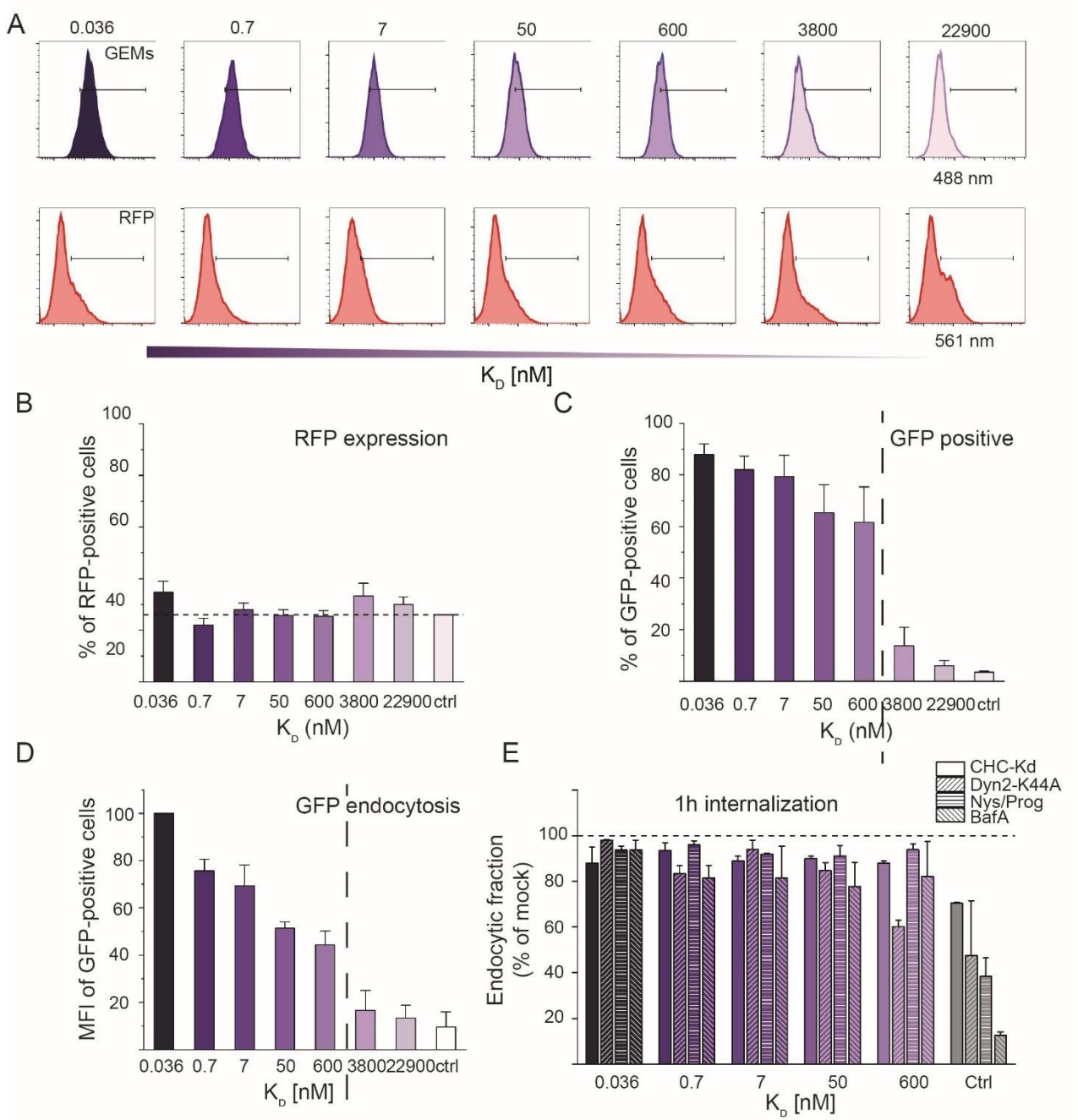

Figure 2.7. Adhesion energy modulates the endocytosis of polyvalent, globular binders. A) Histograms of the GEM endocytosis (top panel) and RFP co-transfection (lower panel) in CV1 cells expressing the panel of GPI-anchored anti-GFP nanobodies as indicated, determined from flow cytometry measurements. Cells were incubated with 2 µg of GEM-GFP for 1 h at 37 ˚C before acidic wash to remove all cell surface-bound GEM fraction. The fluorescence intensities of individual cells were then measured for both GEM and RFP channels, for at least 5000 cells/sample. The percentage of either GFP- or RFP-positive cell population from the total amount of cells is marked on the histograms. **B)** Quantification of the percentage of RFP-positive cells from the total amount of cells as a function of receptor affinity,

determined by the flow cytometry measurements represented in panel A). Measured is intensity of at least 5000 cells/sample, shown is means ± s.e.m., n = 3 independent experiments. The dotted line represents RFP-positive level of control cells transfected with RFP alone. **C)** Quantification of the percentage of GEM positive cells from the total amount of cells as a function of receptor affinity, determined by the flow cytometry measurements represented in panel A). Measured is intensity of at least 5000 cells/sample, shown is means ± s.e.m., n = 3 independent experiments. **D)** Quantification of GEM-GFP endocytosis as a function of receptor affinity as determined by flow cytometry measurements of the mean cell-associated fluorescence after acid wash. Measured is intensity of at least 5000 cells/sample, shown is means ± s.e.m., n = 3 independent experiments. **E**) Quantification of GEM-GFP endocytosis as a function of receptor affinity and upon treatment with genetic (siRNA against clathrin-heavy-chain and expression of dominant negative Dyn2-K44A) or chemical inhibitors (Nystatin/Progesterone and BafilomycinA) as compared to mock treatment controls (Transferrin endocytosis for siRNA against CHC and overexpression of DynK44A; SV40 endocytosis for Nystatin/Progesterone and BafilomycinA). Endocytosis was determined by flow cytometry measurements of the mean cell-associated fluorescence after acid wash. Measured is intensity of at least 5000 cells/sample, shown is means ± s.e.m., n = 2 independent experiments.

To determine the molecular players involved in the endocytosis mechanism of GEMs for all the panel of different binding affinity receptors, I performed the same quantitative endocytosis assays under inhibitor conditions. When I knocked down CHC using an siRNA genetic inhibitor or when I suppressed the activity of dynamin by expressing a dominant-negative variant of the protein, I found that the uptake of Transferrin, a well-known clathrin-mediated endocytosis cargo, was significantly reduced. In comparison, GEM endocytosis did not show a major reduction for any of the different binding affinity receptors, indicating that the entry mechanism of GEMs does not rely on either clathrin or dynamin for any of the adhesion energies between the particles and the membrane (**Figure 2.7**E). In order to ensure that the lack of reduction in GEM endocytosis under these inhibitory conditions was not due to an increase in the amount of receptors on the surface of the cell, I quantified the difference in receptor abundance with and without treatment (**Annex 5.**A). The slight increase in the amount of Tf receptors or GPI-anchored NB receptors was accounted for in the quantifications provided in **Figure 2.7**. Lastly, I observed a strong decrease in the total amount of CHC in cells treated with the siRNA genetic inhibitor as compared to untreated cells (**Annex 5.**B), which indicates that the inhibitory treatments were successful.

When I removed membrane cholesterol by treating cells overnight with Nystatin and Progesterone or when I inhibited endosomal acidification by treating the cells with BafilomycinA, I observed a significant decrease in SV40 uptake, which is known to be highly dependent on cholesterol and endosomal acidification[135]. However, I did not observe a major reduction in GEM endocytosis for any of the binding affinity samples, suggesting that neither cholesterol, nor a drop in pH in endosomes are required for GEM uptake regardless of the adhesion energy of the system (**Figure 2.7**E).

To obtain definitive proof of GEM endocytosis in cells, collaborator Dr. Paolo Ronchi from the European Molecular Biology Laboratories performed correlative light electron microscopy (CLEM) measurements on cells expressing either the highest binding affinity nanobody receptor (0.036 nM) or the threshold affinity receptors (600 nm) that were pre-incubated with GEMs for 1 hour at 37 ˚C. The precise

intracellular location of the GEMs could be determined from their fluorescence signal visualized with a confocal microscope. Afterwards, high resolution electron tomographs were acquired of the regions inside the cells positive for GFP fluorescence. The electron tomographs revealed that GEMs were indeed successfully internalized and colocalized with endosomal compartments (**Figure 2.8**).

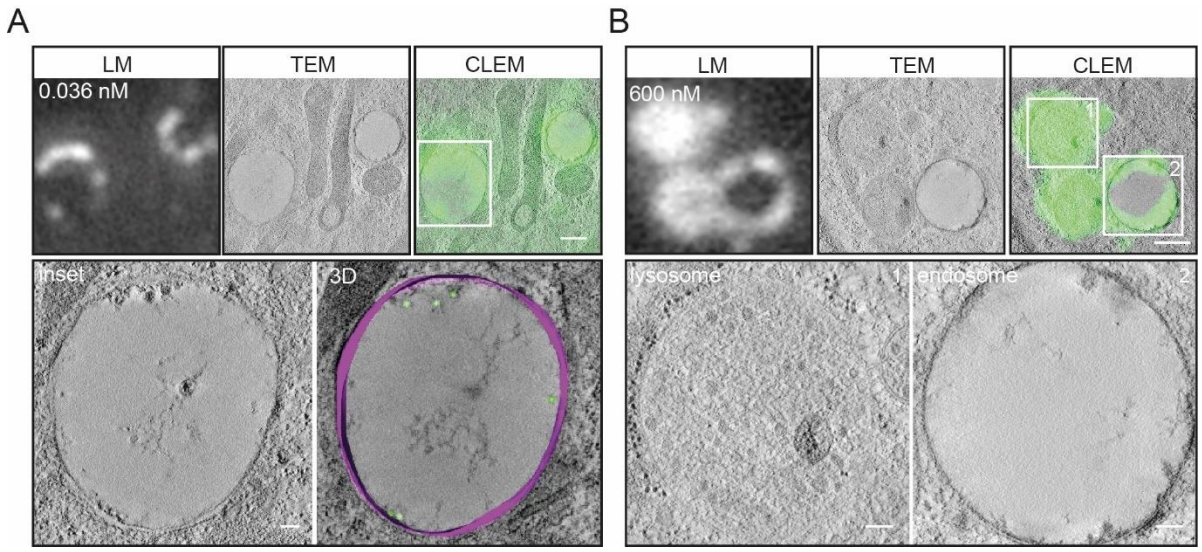

Figure 2.8. GEMs become internalized in endosomes. A) High magnification correlative fluorescence light microscopy and transmission electron microscopy of GEMs internalized in CV-1 cells expressing the 0.036 nM GPI-anchored nanobody after 1 hour of incubation at 37 ˚C. **B)** High magnification correlative fluorescence light microscopy and transmission electron microscopy of GEMs internalized in CV-1 cells expressing the 600 nM GPI-anchored nanobody after 1 hour of incubation at 37 ˚C. Top panel from left to right: Fluorescence micrograph of GEMs; transmission electron micrograph of same region; correlative images. Each panel bottom left: Transmission electron micrograph of inset above. Panel bottom right for the 0.036 nM receptor: Volumetric 3D-reconstruction of electron tomograph on the left. GEMs emphasized in green, membrane emphasized in purple. Panel bottom right for the 600 nM receptor: Transmission electron micrograph of inset number 2 above. Scale bars are 500 nm for overview and 100 nm for insets.

To further investigate the precise endocytic mechanism of GEM endocytosis upon adhesion energy modulation, I performed live-cell colocalization assays between GEMs and Clathrin Light Chain-dsRed and between GEMs and Caveolin1-mRFP on a Total Internal Reflection Fluorescence (TIRF) microscope. I imaged the membrane plane of these cells in a time-course experiment, taking an image every min for 6 min in total, to precisely follow the uptake of GEM events and exclude transient, non-specific colocalization events. First, I found that the GEMs did not significantly colocalize with clathrin for any of the different binding affinity receptors, even though Tf, a known CME marker, colocalized extensively with it (**Figure 2.9**A and C). Next, I found that a fraction of GEMs seemed to colocalize with Caveolin especially for lower binding affinity receptors. Tf did not colocalize with Caveolin1 as expected (**Figure 2.9**B and D). Taken together, these results indicate the existence of a minimum threshold adhesion energy between the GEMs and their receptors that enables efficient endocytosis by a mechanism independent of membrane scaffolding proteins such as clathrin or caveolin, based on multivalent lipid binding alone.

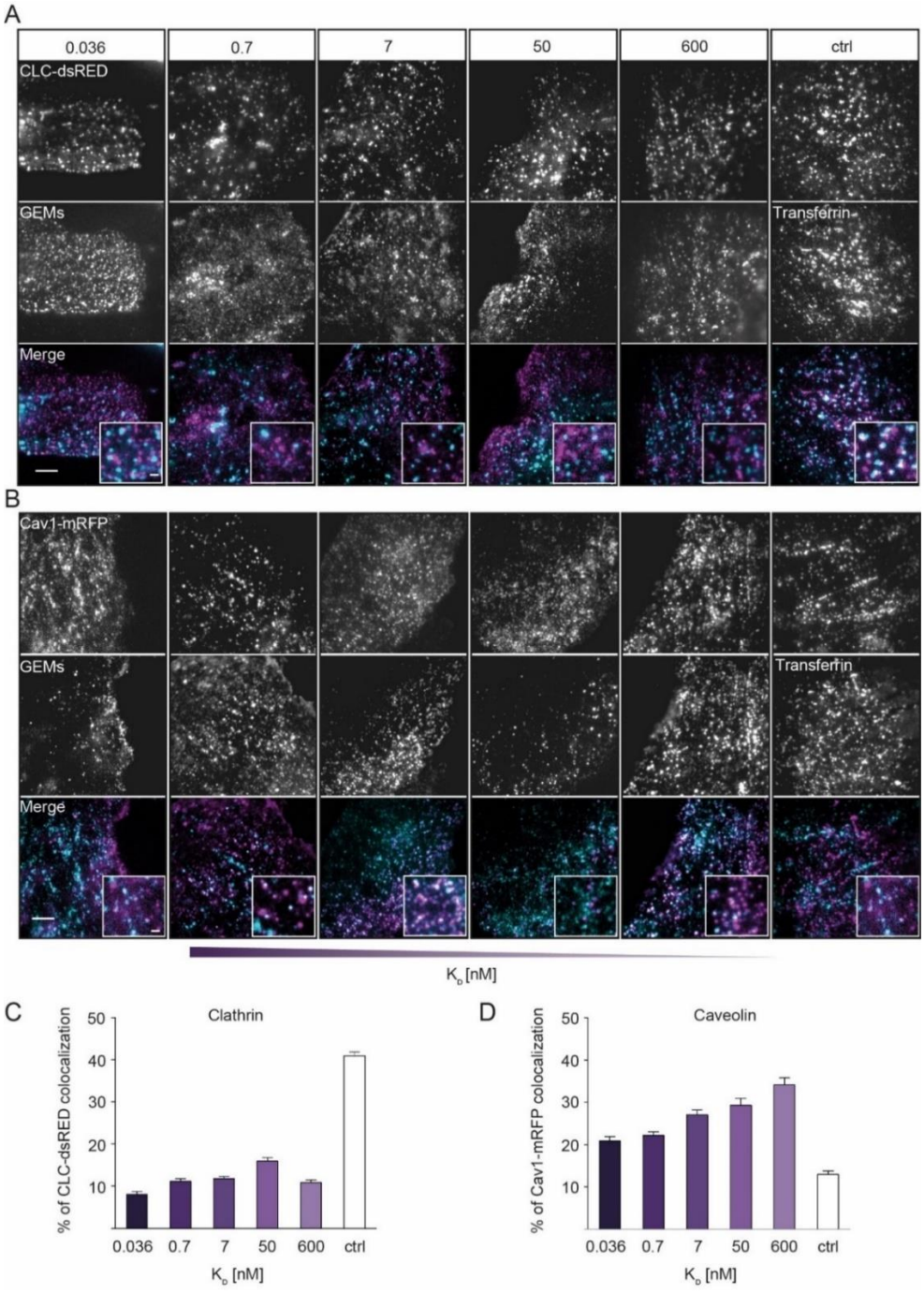

Figure 2.9. GEM endocytosis is by a clathrin- and caveolin-independent mechanism. A) Fluorescence micrographs of GEMs (magenta) bound to CV1 cells expressing Clathrin-light-chain-dsRED (cyan) and the panel of GPI-anchored anti-GFP nanobodies as indicated. CV1 cells were incubated for 10 min with 2 µg of GEMs at 37 ˚C before time-course live imaging on a TIRF microscope. Images were acquired every 1 min for 6 min in total. Scale bar is 5 µm for overview and 1 µm for inset. **B)** Fluorescence micrographs of GEMs (magenta) bound to CV1 cells expressing Caveolin1-mRFP (cyan) and the panel of GPI-anchored anti-GFP nanobodies as indicated. CV1 cells were incubated for 10 min with 2 µg of GEMs at 37 ˚C before time-course live imaging on a TIRF microscope, as described in A). Scale bar is 5 µm for overview and 1 µm for inset. **C)** Quantification of colocalization between GEMs and CLC-dsRED from all the timepoints/cell, means ± s.e.m., n = 3 independent experiments. **D)** Quantification of colocalization between GEMs and Cav1-mRFP from all the timepoints/cell, means ± s.e.m., n = 3 independent experiments.

Chapter 2.1.5. Theoretical modelling of the adhesion-energy mediated membrane wrapping

To understand the biophysical processes that lead to membrane deformation triggered by multivalent lipid binding of globular particles, a physical model was derived by Dr. Thomas Weikl based on the adhesion energy between the particle and the membrane. For successful membrane deformation to occur, the bending energy of the membrane has to be overcome by the adhesion energy between the particle and membrane. The bending energy cost for membrane wrapping depends on the shape and size of the particle. In this regard, certain key parameters were estimated in the modelling of the interaction between GEMs and membranes and are presented in **Table 2.3**.

Table 2.3. Theoretical modelling variable estimates.

l_0	8 nm
σ	1 nm
l	3.2 – 4.8 nm
a	1 – 2 nm
b	2.5 nm
Θ	0 – 50˚

First, the structure of the GEM-GFP monomer was simulated with AlphaFold (**Annex 3.**A) based on its amino acid sequence. The resulting structure of the monomer revealed that the GFP molecule sits very closely to the surface of the *encapsulin* core protein of the GEM. This occurs because the genetically-encoded linker in between them is formed out of 6 repeats of Glycine-Serine, so only 12 amino acid residues in total and collapses into a bent conformation. The estimated vertical extension of this unstructured linker connecting the N-terminus of GFP to the GEM inner core ranges between 1 and 2 nm and is annotated with *a* (**Figure 2.10**A and **Table 2.3**). However, when the GFP moiety binds to the anti-GFP nanobody anchored in the plasma membrane, there is a flexibility in the binding imposed by the linker. The GFP-nanobody complex can wiggle around its axis with a tilt angle Θ estimated to range between 0 to 50 ˚ (**Figure 2.10**A and **Table 2.3**). Thus, the distance between the N-terminus of the GFP and the anchoring point of the anti-GFP nanobody in the membrane is variable according to the value that the tilt angle adopts at any given time. The final distance *l* ranges in between 3.2 and 4.8 nm. Lastly, the distance between the GPI-anchor point and the membrane midplane is notated with *b* and is estimated to be 2.5 nm. All in all, the flexibility of the interaction between the GEMs and membranes is dictated by the total distance between the core of the GEM and the midplane of the membrane, annotated with l_0 that, according to the previous assumptions, is equal to 8 nm, but has a large error σ of 1 nm due to the flexibility of binding.

After estimating the distances involved between the GEMs and the membrane, the adhesion energy of this interaction can be inferred. To do so, it is critical to take into account the multivalent nature of the binding that leads to a two-dimensional binding constant

$$K_{2D} = \frac{[RL]}{[R][L]}$$

(2)

where [R] is the surface concentration of the unbound receptors (GPI-anchored anti-GFP nanobodies), [L] is the surface concentration of the ligands (GFPs on GEMs) and [RL] is the surface concentration of the bound GFP-nanobody complexes. Taking into account the binding constant, the 2D effective adhesion potential at equilibrium becomes

$$[R]K_{2D}(l_0) = \frac{[RL]}{[L]} = \frac{P_B(l_0)}{P_U(l_0)} = e^{-\Delta G(l_0)/k_B T}$$

(3)

where $P_B(l_0)$ is the distance-dependent probabilities that a GEM is bound to a GFP, $P_U(l_0) = 1\text{-}P_B(l_0)$ is the distance-dependent probabilities that a GEM is not bound to a GFP, $\Delta G(l_0)$ is the binding free energy of a GFP-nanobody complex and k_BT is the thermal energy (Boltzmann constant k_B times temperature T). From equation (2), the adhesion energy per area can be determined as

$$V(l_0) = \frac{\Delta G(l_0)}{A} = -\frac{k_B T}{A}\ln[[R]K_{2D}(l_0)]$$

(4)

where $A = 4\pi r^2$ is the area of the globular GEM surrounded by membrane and r is the radius of the GEM particle surrounded by membrane. According to previous studies[146], the effective adhesion potential can be estimated as a Gaussian function

$$V(l) = -U\exp[-(l - l_0)^2/2\sigma]$$

(5)

where the depth of the potential is

$$U = \frac{k_B T}{A}\ln[[R]/\xi K_D]$$

(6)

and ξ is a conversion length[146] from 3D binding of the soluble complex to 2D binding of the anchored complex at the preferred separation l_0. Using the determined biophysical parameters from above, membrane

shape calculations were performed by Dr. Thomas Weikl, where the rotationally symmetric membrane shapes around an individually wrapped GEM and around a GEM in a long membrane tubule are inferred by energy minimization of the effective Gaussian adhesion potential in equation (4). The rescaled adhesion energy then becomes

$$u = \frac{Ur^2}{K} \qquad (7)$$

where K is the bending rigidity of the membrane and is estimated to be $20k_BT$[147].

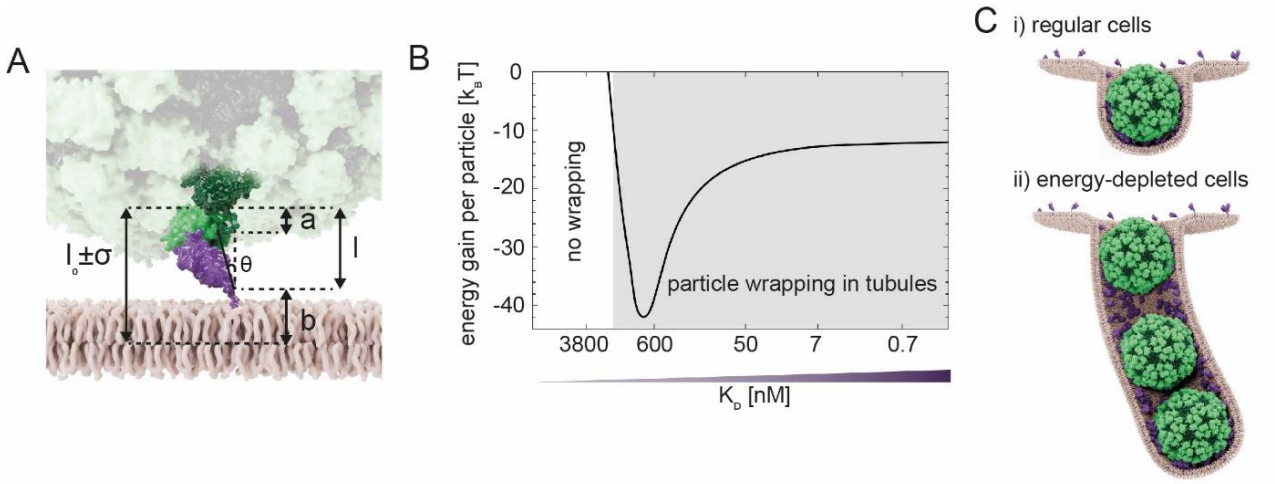

Figure 2.10. Theoretical modelling of GEM-GFP membrane wrapping and tubulation. A) Schematic representation of the geometric parameters considered in the modelling for the length and tilt angle variations: b = estimated distance from membrane midplane to nanobody C-terminus to which the GPI-anchor is attached; a = estimated vertical extensions of unstructured 12-residue peptide linker connecting the GFP N-terminus to the GEM surface; Θ = estimated tilt angle of the complex, i.e of the axis (with length 4.8 nm) connecting the linker attachment sites at the nanobody C-terminus and GFP N-terminus, relative to the membrane normal; l = projected vertical extensions 4.8 nm Cos[Θ] of the complex corresponding to tilt angle estimates. These length estimates and variations lead to the mean distance l_0 = 2.5 + 1.5 + 4 nm = 8 nm and standard deviation σ = -1 nm. **B)** Diagram of energetics of particle wrapping. The energy gain per particle as a function of binding affinities illustrating two regimes: no membrane wrapping and particle wrapping in tubules. **C)** Schematic representation of the two membrane wrapping cases: **i)** GEM wrapping in live cells leading to cellular endocytosis and **ii)** GEM wrapping resulting in the formation of long tubules in energy-depleted cells.

The GEM wrapping in membrane becomes possible when the adhesion energy compensates for the bending rigidity of the membrane. From the calculations, joint particle wrapping in tubules is more energetically favourable than single particle wrapping which explains the experimental findings that GEMs form tubules in model membrane systems. In **Figure 2.10**B, the theoretical threshold for GEM wrapping corresponds to a value of K_D = 1000 nM. This indicates that GEM wrapping is energetically unfavourable for binding affinities lower than 1000 nM and does not occur, which explains well our experimental findings that GEMs do not efficiently bind or deform membranes below this threshold. Above this threshold, GEMs

can wrap themselves with membranes and form an endocytic pit (**Figure 2.10**C, (i)) or extend into longer tubules filled with GEMs like beads on a string in energy-depleted cells (**Figure 2.10**C, (ii)) as there is no active machinery in these cells that could perform scission of the nascent endocytic pits. In this case, wrapping of GEMs into long tubules becomes more favourable than individual particle wrapping as there are two membrane necks around GEMs in a tube which adopt nearly catenoidal shapes with low bending energy and the energy required for the next GEM to enter the tube is smaller than for single particle wrapping.

Chapter 2.1.6. Discussion

In this chapter of the thesis, I have developed a cellular platform to study the biophysical mechanism of multivalent lipid binding endocytosis of non-enveloped, tumour-causing viruses. I have used a genetically altered version of the VLP found in the *Pyroccoccus furiosus* archaeon that bears 180 copies of GFP symmetrically arranged on its globular surface as a mimic of polyomaviruses (**Figure 2.3**A). For it, I have created a panel of lipid-anchored anti-GFP nanobodies with binding affinities spanning over 7 orders of magnitude that could be inserted into the membranes of cells and allowed for particle binding (**Figure 2.5**). Using this artificial VLP and lipidic receptor system, I found that for efficient membrane deformation and endocytosis to occur, a minimum threshold in the binding adhesion must be met (**Figure 2.6**, **Figure 2.7** and **Figure 2.10**). Once the approx. 1 μM-binding affinity threshold is surpassed, membrane wrapping of the multivalent, globular lipid-binding particles becomes energetically favourable and they become internalized in a clathrin- and caveolin- independent manner (**Figure 2.9**).

A tractable, artificial cellular system for the study of clathrin-independent endocytosis

The first line of evidence for the existence of a scaffolding-protein independent endocytic process was derived from studies on the cellular entry of several bacterial toxins, which were observed by electron microscopy to induce the formation of non-coated endocytic pits in cellular membranes[12,16]. However, the major challenges in defining a clathrin- and caveolin-independent uptake pathway remain the lack of defining morphological features and common molecular players. Since the majority of the clathrin-mediated endocytosis inhibitors have been shown to have off-target side effects on other basic processes in the cell, it has been suggested that clathrin-independent uptake arises merely as a compensatory mechanism in order for the cell to maintain homeostasis in inhibitory conditions[18,23]. Recent studies have found more concrete evidence on the prevalence of bona fide clathrin-independent pathways by investigating the entry of non-enveloped viruses that occurs in a non-clathrin, non-caveolin mediated fashion[71,85].

Pathogens such as the non-enveloped SV40 virus and several bacterial toxins have been used as tools to study basic cellular processes, for example clathrin-independent endocytosis. They make use of a tight organization of their glycolipid binding sites to alter the biophysical properties of cellular membranes by inducing lipid clustering and by creating tight membrane contacts. SV40 can multivalently bind to 360 copies of its ganglioside receptor GM1 therefore imprinting its shape onto the membrane and inducing the formation of long, tubular membrane invaginations filled with virions, in both energy-depleted cells and in *in vitro* model membrane systems[85]. The force required for these globular particles to overcome the bending rigidity of the membrane is provided by the avidity of binding. In this work, I first investigated whether this is common cellular entry mechanism shared between the virions of the polyoma family. I found that indeed, several polyoma VLPs can deform membranes into tubular structures like the ones found for SV40, even though they bind to different glycolipid species (**Figure 2.1**). This leads to their uptake in cells, most likely by a clathrin- and caveolin-independent pathway and allows them to internalize in their host cells (**Figure 2.2**).

On the other hand, toxins do not dispose of so many binding sites as they do not self-assemble into globular VLPs, yet they can still their trigger the formation of the same long, tubular invaginations in cells starved of energy and in model membrane systems[85]. There have been several mechanism proposed for membrane curvature generation by toxins: protein clustering on membranes[85,123,131,148], lipid reorganization into membrane ordered regions[83,121] and the specific arrangement of the amino acid residues in their lipid binding sites (such that the membrane has to be pulled upwards at the edges of the toxins when they bind to five lipid receptors thus creating curvature)[149]. The exact biophysical mechanism behind membrane deformation by multivalent lipid binding pathogens such as toxins and viruses is not yet fully understood. The two unrelated systems lack any sequence homology but share a pentameric organization of lipid-binding sites, spaced precisely 3.7 nm apart. This suggests that they have been subject to convergent evolution and employ the same mechanism to trigger their uptake into cells. However, both CTxB and SV40 exhibit a pleiotropic cellular binding behaviour and can interact with several secondary receptors on the plasma membrane of cells[127,150,151], making it impossible to attribute curvature induction to their structural features alone.

A major bottleneck behind the study of the biophysical principle governing the entry of these pathogens has been the existence of a malleable system in which the isolation of individual biophysical parameters can be realized. In this work, I built an artificial cellular system consisting of a globular virus-like-particle, GEM, and its corresponding lipid-anchored receptors. The specificity of the interaction between GFP and anti-GFP nanobodies ruled out the involvement of other proteins in the binding and entry of the GEMs. There was no unspecific binding observed between the GEMs and the membranes of cells lacking

the GPI-anchored nanobody receptors (**Figure 2.5**). Therefore, this artificial system enabled me to specifically study the importance of multivalent lipid binding in endocytosis. I was able to exactly reproduce the behaviour of polyoma-virions, as the GEMs could also bind and diffuse on cellular membranes, bend membranes, and become internalized without the aid of any intracellular active machinery, exactly like the polyoma VLPs.

I found that the major GEM uptake pathway was independent of clathrin and caveolin by performing three complementary assays: genetic inhibitor assays of clathrin heavy chain, colocalization assays with either clathrin light chain or caveolin1 and high-resolution electron microscopy imaging of early, GEM-positive endocytic events at the plasma membrane (**Figure 2.4** and **Figure 2.9**). Taken together, these assays convincingly show that clathrin is not involved in the uptake of GEMs, while only a minor fraction of GEMs make use of caveolin-coated pits for uptake. Likewise, the polyoma VLPs do not require clathrin to induce curvature in the plasma membrane, but rather imprint their globular shape on the membrane through multivalent lipid binding. Some of the VLPs do, however, enter cells through caveolin-coated pits as well[70,89,152,153]. One interesting thing to note here is that caveolin-mediated uptake is dispensable for polyomavirus uptake and infection[71]. While clathrin-mediated endocytosis is a ubiquitous uptake mechanism, caveolin-coated pits are lacking altogether from some cells and their amount and distribution is highly cell type-dependent[154–156]. It is possible that virions randomly fall into caveolin-coated pits or associate with them due to their abundance on membranes. In the future, it would be interesting to test is GEM endocytosis can efficiently occur in cells lacking caveolins or if this pathway is dispensable as it is in the case of polyomaviruses. The similarity in the type of endocytic mechanism employed by polyomaviruses and the artificial GEMs further supports the hypothesis that pathogens convergently evolved to use a common, purely biophysical mechanism for efficient cellular internalization and infection based on multivalent lipid-binding induced membrane deformation.

Lipid reorganization as a curvature generation mechanism

In general, membranes can be bent when the mechanical energy applied to them is higher than the bending energy that characterizes the membrane. There are multiple ways in which membranes can be bent in cells. Besides the spontaneous curvature generated by the intrinsic properties of lipids or transmembrane proteins, membranes can be bent by external factors as well. For example, the insertion of amphipathic helixes by bacterial or viral proteins can induce asymmetric transbilayer stress and their subsequent clustering then triggers membrane curvature[84,157–159]. Other studies suggest that membranes can be bent due to local crowding of proteins due to steric hindrances, which in term creates lateral pressure on the bilayer and leads to spontaneous curvature[81,82,160]. However, these findings must be interpreted with care, as the studies were only performed *in vitro* and under non-physiological conditions. Another possibility for generation

membrane curvature is through intracellular leaflet scaffolding, for example by the well-known clathrin and caveolin scaffolding proteins or BAR proteins (Bin/Amphiphysin/Rvs) that contain both an amphipathic helix region and a naturally curved dimeric membrane-binding domain[161]. BARs can bind electrostatically to phosphoinositide lipid moieties and can impose their curvature on the membrane at high local concentrations[162,163]. They can even self-assemble to create a rigid scaffold on the membrane and generate tubular invaginations[164]. However, some pathogens do not require such scaffolding proteins whatsoever and can deform membranes by multivalent binding to their lipid receptors. This in turn generates a reorganization of the glycolipid receptors underneath them and facilitates the formation of long, tubular invaginations extending from the plasma membrane into the cytosol[84,85]. The same lipid-reorganization mechanism is used by endogenous lectins that also bind multivalently to their receptors and induce membrane deformation in a glycolipid dependent manner[165]. It is possible that the artificial polyvalent, globular lipid-binding GEMs can wrap themselves in membrane by clustering of GPI-anchored proteins beneath them and overcoming the bending rigidity of the membrane. It would be interesting to test in the future if GEMs would associate preferentially with the liquid-ordered phase in model membrane systems[85].

The importance of the adhesion energy in endocytosis

The most important finding of my study revealed that there is a strong connection between endocytosis and the adhesion energy of the cargo for its receptors. I have developed a library of GPI-anchored anti-GFP nanobodies with binding affinities varying from the pM to the mM range (**Figure 2.5**). My artificial system thus enabled the fine-tuning of the adhesion energy between globular binders and membranes over 7 orders of magnitude. I found a clear-cut threshold for both membrane deformation and endocytosis at around 1 μM binding affinity (**Figure 2.6** and **Figure 2.7**). Unexpectedly, the probability of membrane wrapping and tubulation is constant once this threshold in adhesion energy is met, as GEMs induced the formation of a similar number of tubulation events in cells and in GPMVs for all the binding affinities higher than 1 μM (**Table 2.2**). This yes-or-no behaviour suggests that once sufficient energy is provided to overcome the energetic barrier of the membrane, particle wrapping becomes favourable and is a general occurrence (**Figure 2.10**B).

The ability of membrane wrapping by multivalent, globular particles is dependent on the mode of interaction between the ligand and receptor. For example, polyomaviruses interact in a very tight configuration with the membrane, as indicated by the crystal structure of polyomas complexed with their lipid receptors[115,166,167]. However, the GEMs interact more loosely with the membranes, as the GFP molecules are anchored to the inner surface of the capsid via a 12-amino acid residue linker that provides flexibility in the interaction with the lipid-anchored receptors (**Figure 2.10**A). Therefore, the GFP-nanobody complex can wiggle about the normal axis to the midplane of the membrane and results in a range of possible distances

between the particle and the membrane (**Table 2.3**). This additional degree of freedom in my synthetic system causes a shift in the panel of adhesion energies that enable membrane deformation and internalization compared to polyomaviruses. Much higher energies are required in this case than for the polyoma-virions to bend membranes. Polyoma VLPs have a very low individual binding affinity for their glycolipid receptor, around three orders of magnitude lower than the 1 µM binding affinity threshold observed for the artificial GEMs. This difference highlights the importance of the flexibility of the interaction.

In addition, the nanoscopic architecture and the number of binding sites in the artificial GEMs differs from the polyoma-virions and might also account for the higher adhesion energy requirement. The 360 copies of the major structural proteins VP1 of polyoma-virions are arranged in pentamers that occupy the equivalent hexavalent positions in a T = 7 icosahedral capsomere, with individual lipid binding sites spaced precisely 3.7 nm apart. In contrast, only 180 copies of the major structural protein *encapsulin* in the GEM capsid are arranged in a T = 3 icosahedral asymmetric unit and the GFPs on top form both pentamers and hexamers with individual binding sites spaced around 5 nm apart (**Annex 3.**). Still, regardless of this difference in the number, shape and spacing between binding sites, both polyomas and the GEMs make use of multivalent binding to lipid-anchored receptors to trigger their uptake in cells through dramatic curvature generation in membranes. This is indeed a common, purely biophysical mechanism reproducible in a completely synthetic system that is sufficient to promote host cell infection by pathogens.

The lack of cholesterol involvement in GEM uptake

A surprising result came from the extraction of cholesterol from cellular membranes by Nystatin/Progesterone overnight treatment. While the internalization of polyoma-virions is strongly reduced under these conditions, GEM endocytosis remains unaltered (**Figure 2.4** and **Figure 2.7**). Since both systems cluster their lipid receptors in a small area by multivalent receptor binding, it is expected that cholesterol would play an important role in the generation of nanoscopic liquid ordered domains underneath that could facilitate membrane bending. Many studies have found that toxin and virion entry is highly sensitive to cholesterol extraction from the membranes of cells[71,110,141,168] and SV40 even preferred to associate with liquid-ordered domains in model membranes[85].

On the one hand, GEM entry could be independent of membrane cholesterol since the non-endogenous lipidic receptors are overexpressed in cells and might not be as prone to associate with cholesterol as native ganglioside species[169–171]. The receptors for the GEMs are instead GPI-anchored proteins and it is well established that the GPI-anchored proteins internalize through a constitutive pathway termed CLIC/GEEC endocytosis. During endocytosis, tubular CLathrin-Independent endocytic Carriers (CLICs) are formed instead of the classical bulb-shaped endocytic pits and further fuse with heterogeneously-

sized GPI-anchored protein enriched Early Endosomal Compartments (GEECs). These compartments are a subset of early endosomal species that are devoid of Rab5 effector protein and from here, cargo is most likely sorted to recycling endosomes[72,93]. The CLIC/GEEC endocytosis pathway is heavily dependent on the amount of cholesterol in cellular membranes[172,173]. However, there is still much debate about the preference of the GPI-anchored proteins for liquid ordered microdomains in cellular membranes. It has been suggested that only some of the signal sequences attached to the GPI-anchored proteins allow them to adhere to such liquid ordered domains[174–176], while other studies have convincingly shown that the number of GPI-anchored proteins that cluster together is too small to constitute a functional microdomain and is rather a transient association of the proteins[172,177,178]. Perhaps the transient association of the high-amount of overexpressed GPI-anchored proteins with each other would render their uptake independent of cholesterol-enriched microdomains in the membrane. More answers could be deduced from testing the preference of the GEMs for liquid-ordered domains in model membrane systems or their association with detergent-resistant membranes in cells.

On the other hand, it might be difficult for GEMs interacting with the GPI-anchored receptors to create liquid-ordered phases in the membrane. This interaction might be simply too flexible to allow for phase separation. Therefore, cholesterol would not play a role in the uptake process of the GEMs.

However, it is surprising that cholesterol is not involved in the regulation of GEM endocytic events since I observed a considerable fraction of the total GEM-endocytic events to be caveolin positive (**Figure 2.9**). It is known that caveolin assembly at the pit-formation spot on the inner leaflet of the membrane is cholesterol dependent and the extraction of cholesterol from membranes leads to the disassembly of caveolin structures[66,67,179]. So even though some GEMs make use of caveolin to enter the cells, cholesterol extraction does not reduce GEM uptake. This could suggest that GEMs randomly fall into caveolin-coated pits. At lower adhesion energies, the interaction between the particles and the membrane is not as strong and the formation of endocytic pits most likely takes longer to be initiated. Caveolin recruitment could be facilitated by the longer timescales required for curvature generation, given the propensity of crosslinked GPI-anchored proteins to be targeted to caveolin-coated pits[180–182]. At higher receptor binding affinities, membrane deformation-triggered endocytosis could occur fast enough that caveolin recruitment does not occur to the same extent. All in all, it is not clear throughout literature if caveolin-coated pits do indeed act as an autonomous endocytosis pathway or if they play a different role. In the future, it would be interesting to investigate the specific uptake mechanism of GEMs in cells where cholesterol levels are decreased by inhibitor treatment.

Endosomal acidification and receptor availability in GEM endocytosis

Bafilomycin A1 (BafA1) is a known antibiotic that inhibits vacuolar V-ATPases and disrupts the autophagic flux of the cells by preventing the fusion of lysosomes with autophagosomes[183,184]. Also, BafA1 inhibits translocation of H+ through the V-ATPases after binding and prevents the acidification of endosomal compartments. BafA1 treatment severely inhibits the uptake of SV40[135] (**Figure 2.7**) and other polyoma-virions[106,110,185], but not of GEMs at any given receptor binding affinity. Polyoma VLP entry depends on early endosomal acidification, which triggers a conformational change in the viral capsid structure that releases their receptors for subsequent recycling to the plasma membrane. It might not be the case for the GEMs, where receptors are overexpressed and do not necessarily have to be recycled. In comparison, gangliosides are found in a very low concentration in the external leaflet of the plasma membrane, with total amounts of around ~2% of the total lipid content of the membrane[186,187]. Given that each polyoma VLP can bind up to 360 copies of its receptor at a time, ganglioside amounts in the plasma membrane are likely to get depleted rather fast upon viral entry. Therefore, rapid release and recycling of these glycolipids due to the acidic environment of early endosomes proved to be crucial in viral infection. In contrast, the overexpression of the GPI-anchored nanobody receptors leads to continuous replenishment of the cell surface levels and could possibly be more independent of the receptor recycling process than the uptake of polyomaviruses.

Possible scission mechanisms of GEM-positive endocytic pits

First, I observed the long, tubular membrane invaginations containing GEMs diffusing around in GPMVs without any observable internalization of the particles inside of the lumen of the vesicles. This suggests that it is not enough for the GEMs to wrap themselves with membrane in order to also trigger membrane scission (**Figure 2.6**A). Moreover, the scission of the GEM-positive endocytic pits from the plasma membrane of cells must be an energy-dependent process. In energy-depletion experiments, treatment for 20 minutes with 2-deoxy-D-glucose, a variant of glucose that cannot undergo glycolysis and NaN_3 leads to acute depletion of cellular energy at the point where GEMs are added. The GEMs can deform membranes into invaginations filled with particles, but they remain stuck in tubules instead of internalizing under such energy-depletion conditions (**Figure 2.6**B). Therefore, there must be some energy-dependent molecular players responsible for the pinch-off of the GEM endocytic pits.

Secondly, I checked for the involvement of dynamin, a GTP-binding pinchase known to constrict the necks of fully-formed endocytic pits. I inhibited its function by expressing a dominant-negative dynamin2 construct and observed a reduction in Transferrin uptake, used here as a positive control for dynamin inhibition (**Figure 2.7**). However, GEM uptake was not significantly affected under these conditions. Interestingly, dynamin has been reported to affect the entry of bacterial toxins and SV40,but is not essentially

required for their internalization to occur[84,85,188]. This suggests that there must be multiple synergetic mechanisms employed by cells to pinch off newly formed endocytic vesicles.

Actin polymerization plays an important role in all types of endocytosis, from clathrin-mediated[189,190] to clathrin-independent endocytosis[173,191,192]. It has been determined that actin polymerization at the neck of the budding vesicles containing toxins or SV40 virions can lead to their extension and subsequent scission[85,88,89]. Also, dynein motor proteins seem to pull on the forming vesicles while walking on microtubules and extend them into longer invaginations, as it was observed for cholera toxin-filled membrane invaginations[91]. Microtubules also affect the extension of SV40-filled tubular invaginations[85]. In the future, it will be of great importance to investigate to what extent the cytoskeleton is responsible for the pinching of GEM-positive endocytic structures, especially since GPI-anchored proteins form transmembrane interactions with cortical actin that leads to their clustering in nanodomains[193]. Lastly, BAR proteins were recently found to play a role in the formation and pinching of clathrin-independent endocytic pits filled with bacterial toxins[86,87,194]. BAR-domain proteins might be involved in the entry of GEMs as well; however this remains to be determined.

In conclusion, I have developed an experimental platform suited for the study of clathrin-independent entry mechanisms triggered by multivalent lipid binding. I found that artificial mimics of the viral architecture of lipid-binding sites behave similarly to non-enveloped viruses, by deforming membranes to mediate their uptake without the aid of scaffolding proteins, in an adhesion energy dependent manner. In the future, I envision that this artificial system could be expanded further to study the influence of other biophysical properties on endocytosis such as the diameter of the multivalent particles, the linker length or the lipid receptor moiety.

Chapter 2.2. Intracellular trafficking mechanism of multivalent lipid binders

Non-enveloped viruses such as the polyomaviruses are known to traffic through the endo-lysosomal system towards the ER where they begin to disassemble in order to release their genomic content and finish the infection cycle of the host cell. These viruses can escape the acidic environment of the lysosomes even though they suffer conformational changes that facilitate the subsequent disassembly of their viral capsids once in the ER. In contrast to the polyoma-virions, AB_5 bacterial toxins bypass the lysosomes altogether and traffic instead through the Golgi apparatus on their way to the ER. Both polyoma-virions and bacterial toxins make use of multivalent lipid binding in a pentameric configuration for inducing curvature in the plasma membrane of cells and facilitating their internalization. However, these two pathogens are trafficked to different intracellular compartments in the cell and the exact mechanism leading to their sorting in either lysosomes or the Golgi remains poorly studied. It is unclear whether their specific binding site geometry on either a globular or a flat configuration is directly responsible for their traffic to one organelle or the other. The aim of the work performed in this chapter is to address this hypothesis using artificial constructs that mimic the number and organization of lipid binding sites of the polyoma-virions and of the bacterial toxins.

Chapter 2.2.1. Polyoma-virions traffic through the endo-lysosomal system

SV40 was previously found to traffic through the endo-lysosomal system in cells on its way to the endoplasmic reticulum[135]. To ask whether this is a common behaviour of all the members of the polyomavirus family, I first assembled virus-like-particles (VLPs) from the VP1 major structural capsid proteins of the SV40 virus, JC polyomavirus (JCPyV), mouse polyomavirus (mPyV) and BK polyomavirus (BKPyV) as described in the previous results chapter (**Figure 2.1**A). In addition, I purified the VP1 of the Merkel cell polymavirus (MCPyV) from mammalian cells and allowed it to self-assemble into a VLP as described in the Material and Methods section. All the assembled VLPs used here are not infectious agents since they are composed out of the capsid proteins alone and lack any genomic content. From all of these viruses, JCPyV, BKPyV and MCPyV can infect humans, while SV40 infects monkeys and mPyV infects mice. Thus, these VLPs bind to different glycolipid moieties on the external leaflet of the plasma membrane, namely SV40 binds to GM1, JCPyV binds to GD1b, mPyV binds to the GD1a and GT1b gangliosides, BKPyV binds to GD1b and GT1b and MCPyV binds to GT1b and GM3, respectively.

I then performed pulse-chase assays with the VLPs in CV1 cells to track their intracellular distribution over time. Initially, cells expressing a lysosomal marker, Lamp1-EGFP were pre-cooled to 4 ˚C in order to stop endocytosis from occurring. Next, I added 2 µg/ml of each VLP to the cells and incubated them for 30 minutes at 4 ˚C to allow the VLPs to bind efficiently to the plasma membrane. Next, I switched the cells to 37 ˚C to restore endocytosis and imaged them live on a spinning disk confocal microscope every hour for a total of 6 hours. I observed that the virions begin to colocalize with lysosomes a couple of hours after their uptake and reach a peak in colocalization after 5 hours (**Figure 2.11**A, B). Strikingly, while almost all the SV40 and JCPyV reached the lysosomes already after 3 hours, mPyV accumulated to a lower extent in these compartments, even after 6 hours of chase time (**Figure 2.11**B).

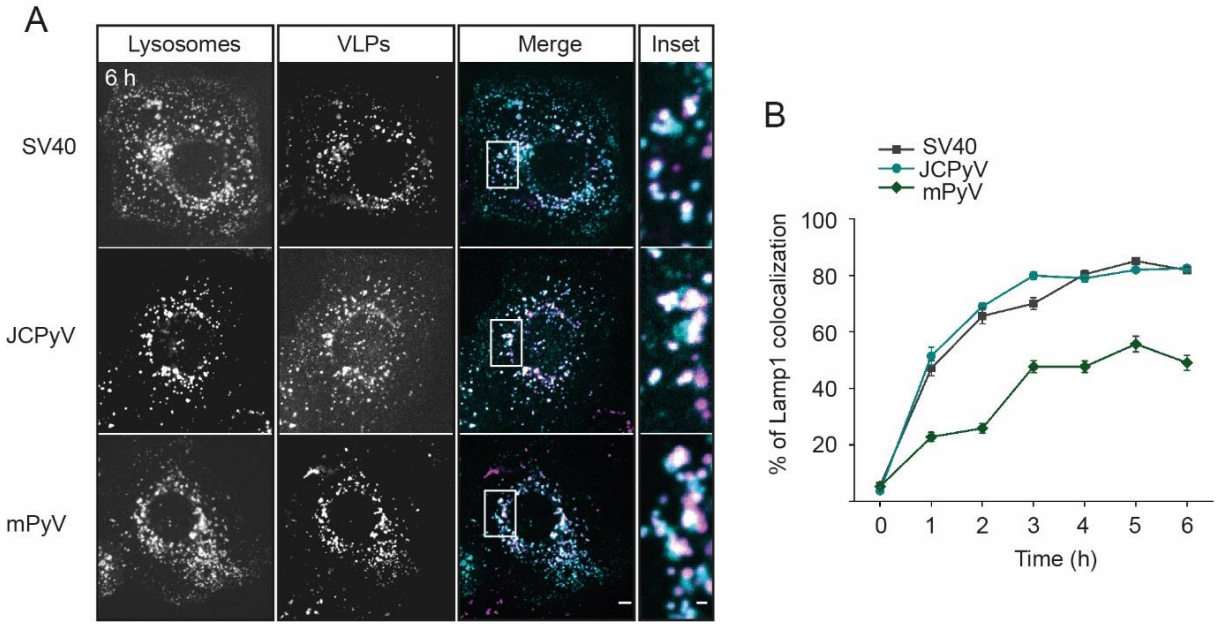

Figure 2.11. Polyoma-virions traffic through lysosomes. A) Representative confocal fluorescence micrographs of Lamp1-EGFP expressing cells containing the indicated VLPs after 6 h incubation at 37 ˚C. CV1 cells expressing Lamp1-EGFP were kept at 4 ˚C for 10 min before incubation with 2 µg of the indicated VLPs for 30 min at 4 ˚C. The cells were switched to 37 ˚C and imaged live on a spinning disk confocal microscope every h for 6 h in total. Scale bars are 5 µm and 1 µm for insets. Magenta: VLPs, Cyan: Lamp1-EGFP. **B)** Quantification of colocalization in confocal fluorescence micrographs between polyomavirus VLPs and lysosomes as marked by Lamp1-GFP in live cells. Means ± s.e.m., n = 2 independent experiments.

To investigate if the VLPs traffic to the Golgi, I performed similar pulse-chase assays to the ones described above in CV1 cells together with master student Alexia de Caro. In brief, pre-cooled CV1 cells were incubated with 2 µg/ml of the respective VLPs for 30 minutes at 4 ˚C to allow VLP-binding to cell membranes. Then, the samples were transferred to 37 ˚C for the indicated time points before fixation and subsequent immunolabeling with antibodies against GM130, a cis-Golgi matrix protein[195]. The samples were then imaged on a spinning disk microscope and the amount of colocalization between the VLPs and the Golgi marker was analysed. We found that none of the different polyoma VLPs colocalized with the Golgi

apparatus during the 3 h time-course of the assays (**Figure 2.12**A, B)., in contrast to the high degree of colocalization between the B-subunit of the Cholera toxin (CTxB) and the Golgi showed here as a positive control (**Figure 2.12**B, red curve).

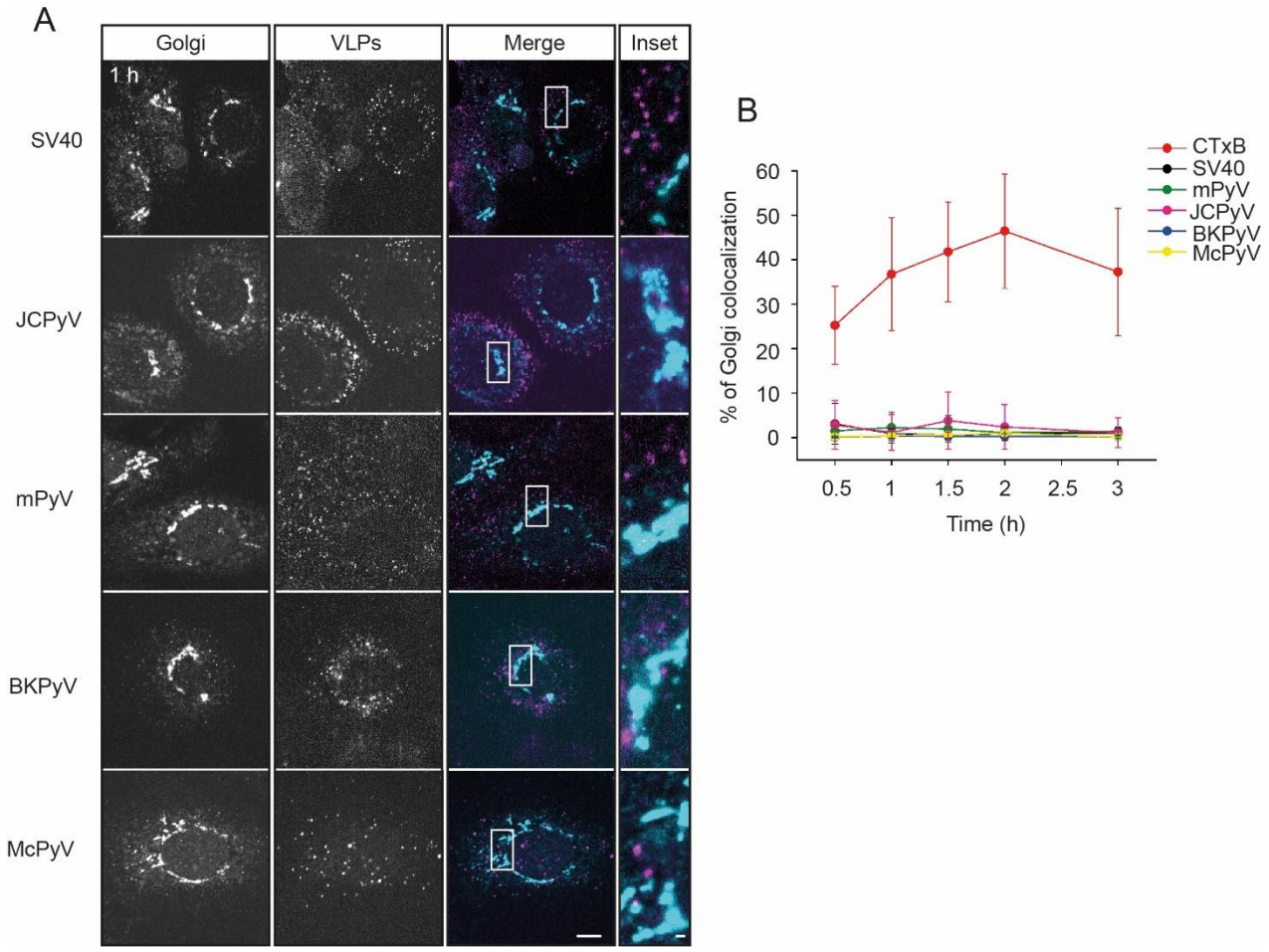

Figure 2.12. Polyoma-virions do not traffic through the Golgi apparatus. A) Representative confocal fluorescence micrographs of cells containing the indicated VLPs and stained with anti-GM130 antibodies to mark the Golgi apparatus after 1 h incubation at 37 ˚C. CV1 cells were kept at 4 ˚C for 10 min before incubation with 2 µg of the indicated VLPs for 30 min at 4 ˚C. The cells were then incubated at 37 ˚C for the indicated times before fixation and immunostaining. Scale bars are 10 µm and 1 µm for insets. Magenta: VLPs, Cyan: Golgi. **B)** Quantification of colocalization in confocal fluorescence micrographs between polyomavirus VLPs and Golgi as marked by anti-GM130 antibodies in fixed cells. CTxB is used as a positive control for Golgi colocalization. Means ± S.D.

Taken together, these results support the hypothesis that all VLPs traffic through the endo-lysosomal system, while bypassing the Golgi entirely, on their way to the endoplasmic reticulum where they complete their infection of the host cells.

Chapter 2.2.2. Synthetic polyvalent, globular lipid-binders also traffic through the endo-lysosomal system

I next aimed to understand if traffic through the endo-lysosomal system is a common mechanism for globular, multivalent-lipid-binding particles that resemble the size and molecular architecture of binding sites of polyoma-virions. To this end, I made use of the same synthetic virus and receptor system developed in Chapter 2.1. In brief, I purified a globular, 37-nm in diameter particle (GEM) that self-assembles from 180 copies of the *encapsulin* protein originating from a virus-like-particle of the archaeon *Pyrococcus furiosus*[143] which is genetically-linked to a GFP molecule. The resulting synthetic VLP displays 180 copies of GFP regularly spaced all over its surface (**Figure 2.13**A). As receptors for the GEMs, I added a GPI-anchor to a high affinity (0.036 nM) anti-GFP nanobody, that could be successfully incorporated into the external leaflet of the plasma membrane by transient expression (see **Figure 2.5** from previous Results chapter).

First, I investigated where the artificial VLPs traffic to after cellular uptake. I performed pulse-chase assays with the GEMs, where I analysed their colocalization with either Lamp1-positive lysosomes or with Rab7-positive late endosomes. I added 2 µg/ml of GEMs to cells transiently expressing these markers and the high affinity GPI-anchored anti-GFP nanobody and performed a 6-hour time-course colocalization assay in live cells on a spinning disk confocal microscope. I found that the GEMs colocalized well with lysosomes, especially 3 hours after internalization (**Figure 2.13**B, C). Surprisingly, the GEMs did not colocalize with lysosomes to the same extent that polyoma-virions did, as only around 30% of the total amount of GEMs in a cell were localized in Lamp1-positive compartments as compared to 80% of the total amount of polyoma VLPs colocalizing with lysosomes. Additionally, GEMs accumulated in late endosomes as well as indicate by their colocalization with Rab7, however this occurred much slower and peaked at around 30% after 6 hours post-internalization (**Figure 2.13**B and D). The polydispersity of the GEM distribution to various endosomal compartments, instead of the highly specific accumulation in lysosomes, could indicate a loss in the specificity of intracellular trafficking or a possible degradation of the GEMs in lysosomes over time.

Next, I looked at whether GEMs traffic to the Golgi apparatus as well. I performed pulse-chase assays on pre-cooled CV1 cells incubated with 2 µg/ml of GEMs for 30 minutes at 4 ˚C to allow efficient membrane binding of the particles. Then, the cells were switched to 37 ˚C for the indicated time points before fixation and immunolabeling with anti-GM130 antibodies. I found that there was very low colocalization between the GEMs and the Golgi (**Figure 2.14**A and B), as compared to the amount of colocalization between the CTxB and the Golgi shown as a positive control here (**Figure 2.14**B, red curve).

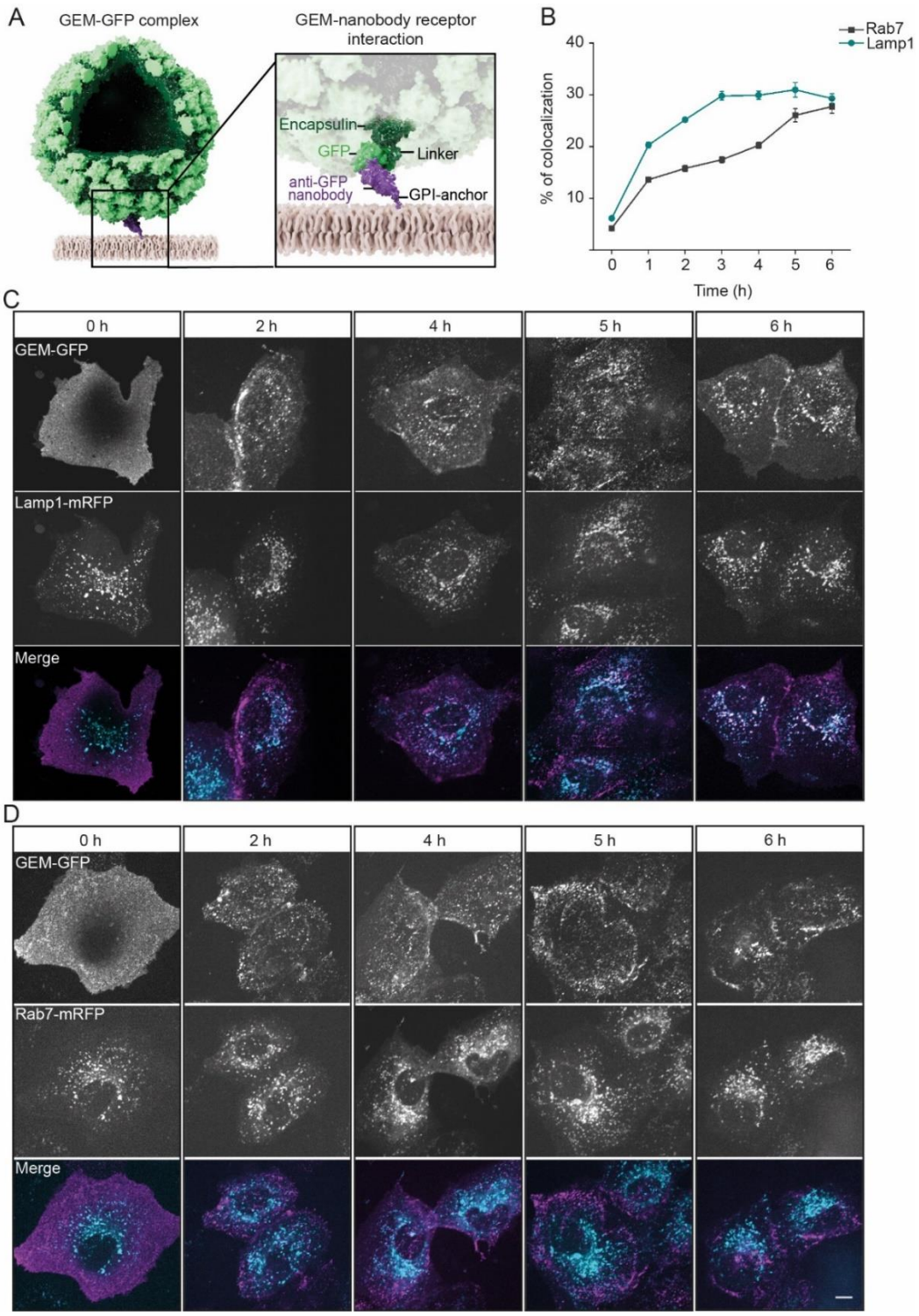

Figure 2.13. GEMs are trafficked through the endo-lysosomal pathway. A) Schematic representation of the synthetic system. Shown is a genetically encoded nanoparticle (GEM) assembled from 180 copies of the *encapsulin* protein (dark green) coupled to GFP (light green) scaffold. A GPI-anchored anti-GFP nanobody (purple) inserted into the membrane (beige) serves as receptor. **B)** Quantification of colocalization between GEMs and Lamp1-mRFP and between GEMs and Rab7-mRFP. Means ± s.e.m., n = 3 independent experiments. **C)** Fluorescence micrographs from a time-course experiment of endocytosis showing the distribution of GEMs in CV1 cells expressing anti-GFP nanobody and Lamp1-mRFP. Cells were incubated with 2 μg of GEMs for the indicated time points at 37 ˚C before live imaging

on a spinning disk confocal microscope. Scale bars are 10 µm. **D)** Fluorescence micrographs from a time-course experiment of endocytosis showing the distribution of GEMs in CV1 cells expressing anti-GFP nanobody and Rab7-mRFP. Cells were incubated with 2 µg of GEMs for the indicated time points at 37 ˚C before live imaging on a spinning disk confocal microscope. Scale bar is 10 µm. Magenta: GEMs; Cyan: Golgi.

To obtain a deeper understanding of the precise intracellular location of the GEMs at various time points after internalization, I performed pulse-chase assays in CV1 as described above after which collaborator Dr. Paolo Ronchi proceeded to cryofreeze the cells and further prepare them for CLEM measurements. He first acquired fluorescence microscopy images of the GEMs in order to pinpoint their exact localization inside cells. Then, he first acquired low-magnification transmission electron micrographs of the cells containing GEMs and selected regions of interest enriched in GFP fluorescence. He then acquired high-magnification transmission electron tomograms of the selected regions of interest positive for GEM signal. GEMs localized exclusively to endosomal compartments inside the cells, both after 1 and 6 hours after internalization (**Figure 2.15**A-D) and were completely excluded from the Golgi apparatus.

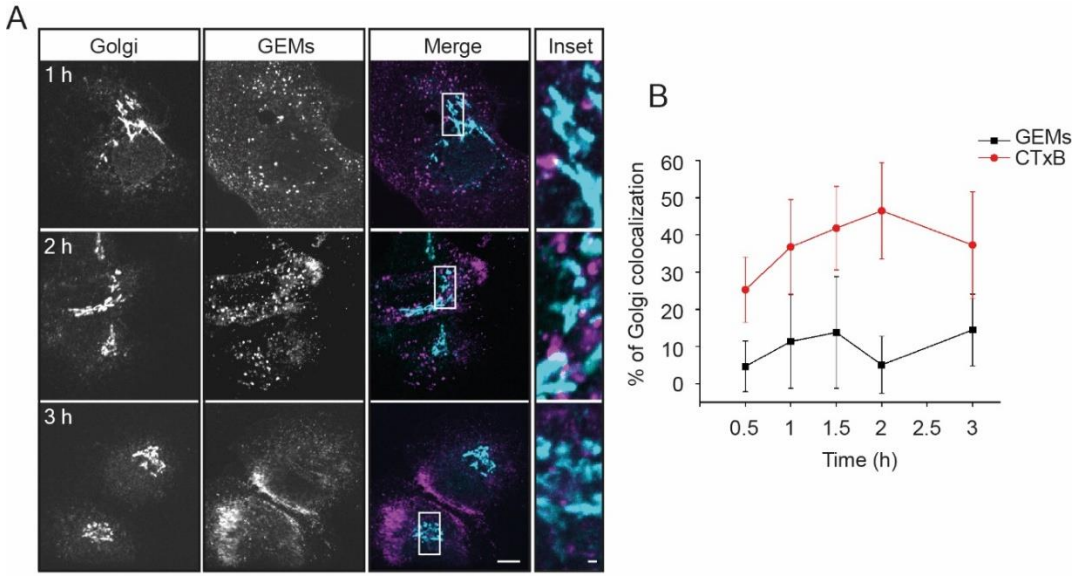

Figure 2.14. GEMs do not traffic to the Golgi apparatus. A) Fluorescence micrographs from a time-course experiment of endocytosis showing the distribution of GEMs in CV1 cells expressing anti-GFP nanobody and immunostained with anti-GM130 antibodies to mark the Golgi. Cells were incubated with 2 µg of GEMs for the indicated time points at 37 ˚C before fixation. Scale bar is 10 µm and 1 µm for inset. Magenta: GEMs; Cyan: Golgi. **B)** Quantification of colocalization between GEMs and Golgi apparatus. CTxB is used as a positive control for Golgi colocalization. Means ± S.D.

These results confirm that the GEMs do not traffic to the Golgi apparatus and traffic through the endo-lysosomal system instead, exactly like the polyoma-virions. Therefore, these results suggest that globular, multivalent lipid binding particles all traffic through the endo-lysosomal system.

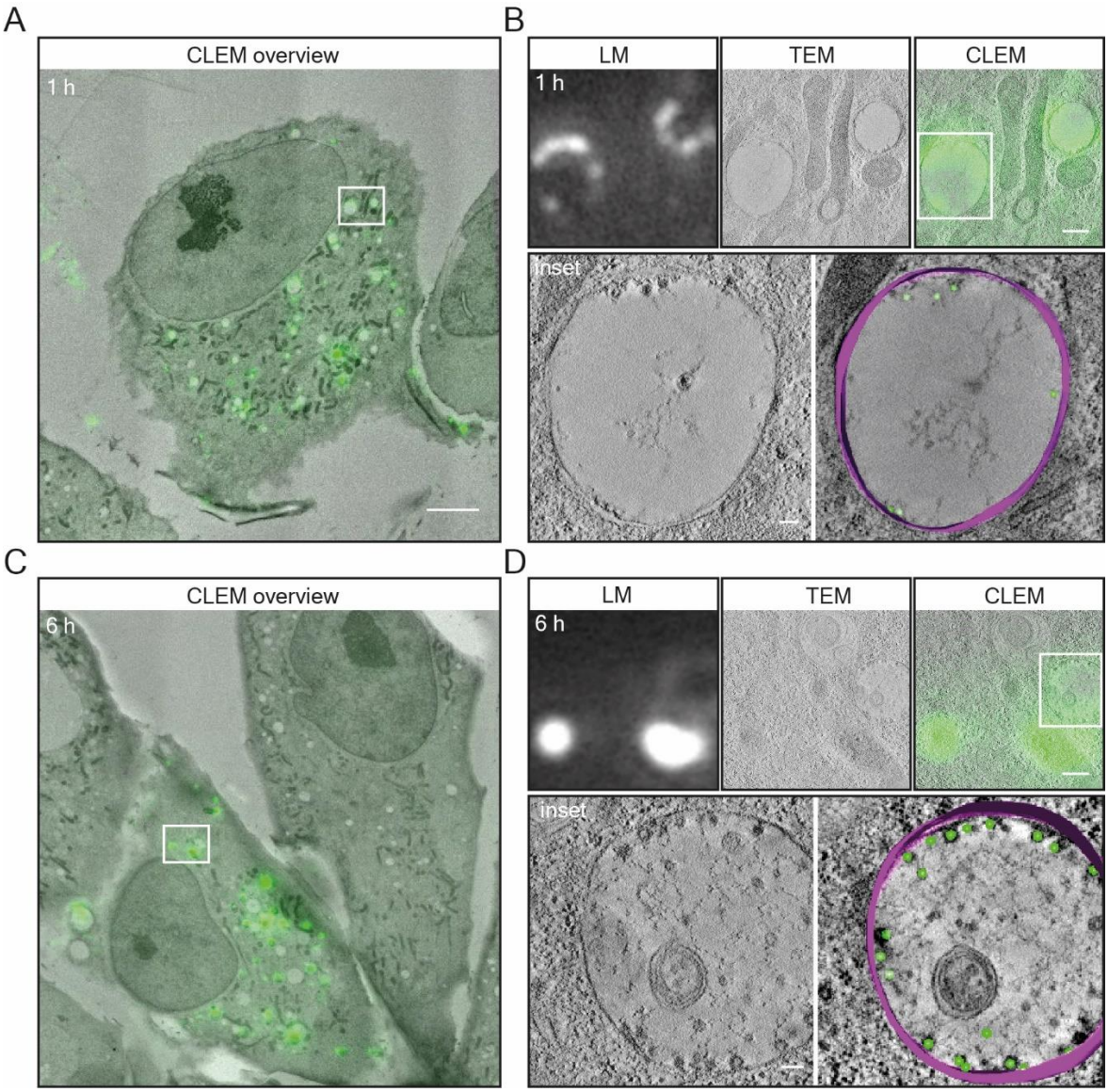

Figure 2.15. GEMs exclusively localize to endosomal compartments. A) Low magnification correlative fluorescence light microscopy and transmission electron microscopy of GEMs internalized in CV-1 cells expressing the GPI-anchored anti-GFP nanobody. Timepoint 1h after binding. Scale bar is 5 µm. **B)** High magnification correlative fluorescence light microscopy and transmission electron microscopy of GEMs internalized in CV-1 cells expressing the GPI-anchored nanobody from the region marked in A). Top panel from left to right: Fluorescence micrograph of GEMs; transmission electron micrograph of same region; correlative images. Each panel bottom left: Transmission electron micrograph of inset above. Each panel bottom right: Volumetric 3D-reconstruction of electron micrographs. GEMs emphasized in green, membrane emphasized in purple. Scale bars are 500 nm for overview and 100 nm for insets. **C)** Low magnification correlative fluorescence light microscopy and transmission electron microscopy of GEMs internalized in CV-1 cells expressing the GPI-anchored anti-GFP nanobody. Timepoint 6h after binding. **D)** High magnification correlative fluorescence light microscopy and transmission electron microscopy of GEMs internalized in CV-1 cells expressing the GPI-anchored nanobody from the region marked in C). Top panel from left to right: Fluorescence micrograph of GEMs; transmission electron micrograph of same region; correlative images. Each panel bottom left: Transmission electron micrograph of inset above. Each panel bottom right: Volumetric 3D-reconstruction of electron micrographs. GEMs emphasized in green, membrane emphasized in purple. Scale bars are 500 nm for overview and 100 nm for insets.

Chapter 2.2.3. Polyoma-virions exhibit pleiotropic membrane binding behaviour

To ask where the difference in the lysosomal trafficking specificity between the polyoma VLPs and the synthetic VLPs stems from, I investigated whether secondary receptors interacting with the virions on the plasma membrane might play a role. For this, I added the MCPyV to an *in vitro* model membrane system consisting of a membranous bubble that lacks any protein in its structure or in its lumen, called Giant Unilamellar Vesicles (GUVs). The GUVs contained only phospholipids and the GT1b ganglioside receptor of the VLPs (98% DOPC, 1% GT1b and 1% β-BODIPY FL C12-HPC membrane dye). Surprisingly, no VLP binding to these membranes could be observed (**Figure 2.16**B, top panel), suggesting that a third-party molecular player needs to mediate its adhesion to the ganglioside receptor.

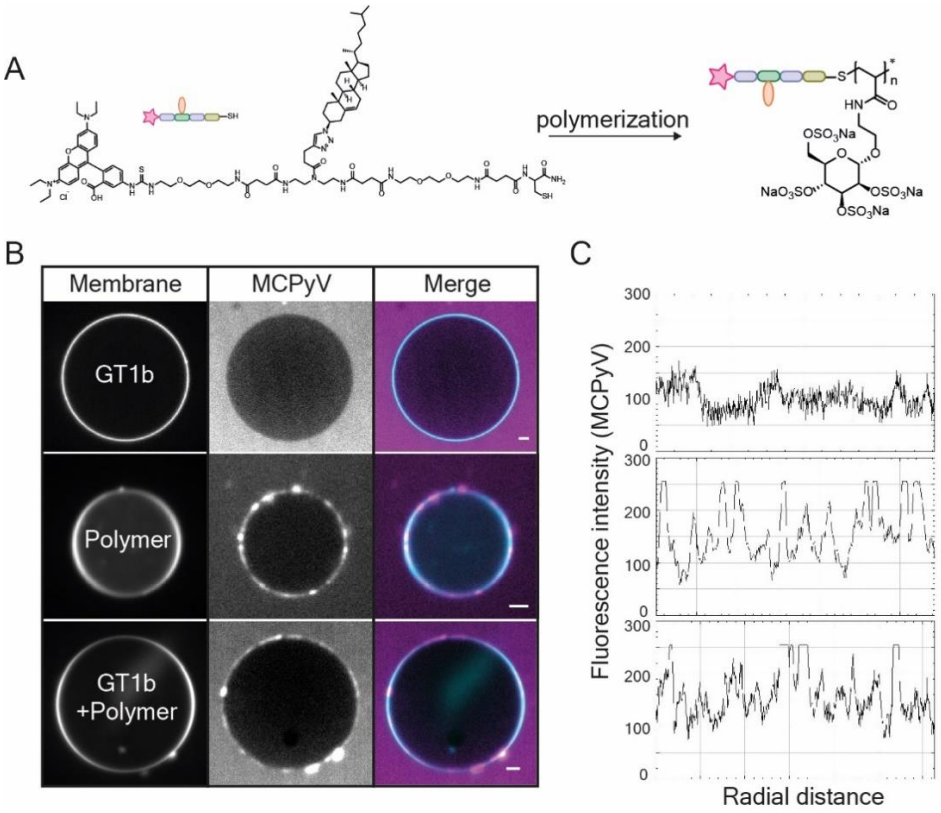

Figure 2.16. Polyoma-virions exhibit pleiotropic membrane binding behaviour. A) Schematic representation of the Rhodamine-labelled, cholesteryl-bound macroinitiator (left) attached to a polymeric backbone (right). The polymer contains n = 76 repeats of the monomer and is highly sulphated as a result. **B)** Spinning disc confocal fluorescence microscopy micrographs of MCPyVs bound to GUVs containing either the GT1b ganglioside receptor alone (top panel), the polymeric construct alone (middle panel) or both GT1b and the polymer (bottom panel). 2 µg of VLPs were incubated for 1 h at RT with GUVs and imaged at the equatorial plane. Scale bars are 2 µm. Magenta: VLPs; Cyan: Membrane stain or polymer fluorescence signal **C)** Fluorescence intensity profiles of the MCPyV at the equatorial planes of the respective GUVs.

To understand what kind of other factors could be involved in this interaction, we tested whether the MCPyV could bind to components of the glycocalyx surrounding the cells. For this, the chemistry group

of Prof. Laura Hartmann from the University of Düsseldorf synthesized a biomimetic glycopolymer that resembles the sulfation pattern of glycosaminoglycans (GAGs) found in the extracellular matrix. A cholesteryl tether and a fluorescent dye were attached to the monomer during synthesis (**Figure 2.16**A, left). This compound was then polymerized into a 76-monomeric long structure (**Figure 2.16**A, right). The polymer was successfully incorporated into the membranes of GUVs as confirmed from its fluorescence signal outlining the GUV contour at the equatorial plane (**Figure 2.16**B, middle and lower panels). Next, I added 2 µg/ml of MCPyVs to GUVs with or without gangliosides in their composition (99% DOPC, 1% polymer and 98% DOPC, 1% polymer, 1% GT1b). I observed that the VLPs could efficiently bind to the membranes of both GUVs (**Figure 2.16**B, middle and lower panel). There was no enhancement of VLP binding when the GT1b ganglioside was incorporated into the membranes, as can be seen in the plot profiles of the VLP fluorescence intensity around the circumference of the GUVs (**Figure 2.16**C).

These results point out the importance of the secondary receptors in the membrane binding ability of polyoma-virions. The interaction with long, highly-sulphated carbohydrates in the extracellular matrix on cells might have an influence on the intracellular trafficking of these virions as well.

Chapter 2.2.4. The pentameric subunits of AB5 bacterial toxins traffic through the Golgi apparatus

Next, I aimed to investigate whether all toxins that have an AB5 configuration of their lipid binding sites would traffic through the Golgi apparatus on their way to the endoplasmic reticulum. I performed pulse-chase assays with recombinant β-subunit of the Cholera toxin and recombinant β-subunit of the Shiga toxin (**Figure 2.17**A) to visualize their intracellular distribution over time after uptake. In brief, I added 5 µg/ml of each toxin to pre-cooled cells and incubated them for 30 minutes at 4 ˚C before transferring the samples to 37 ˚C. Next, the samples were fixed after the indicated incubation times, immunolabelled against GM130 and imaged on a spinning disk confocal microscope.

Both the toxins revealed a clear colocalization with the Golgi apparatus, starting as early as 30 minutes after uptake of the proteins in the cytosolic space (**Figure 2.17**B-D). At all time points, the toxins accumulated in structures that follow a Golgi-shape pattern that overlaps well with the GM130 labeling (**Figure 2.17**C,D). This effect has not been observed previously for neither the polyoma-virions nor for the globular synthetic particles (GEMs). In addition, the toxins are also found in round, vesicular structures, most likely recycling endosomes (**Figure 2.17**C,D), but this has not been quantified. These results correlate well with previous findings in literature where AB5 toxins were found to traffic through the Golgi apparatus[133,141,196,197].

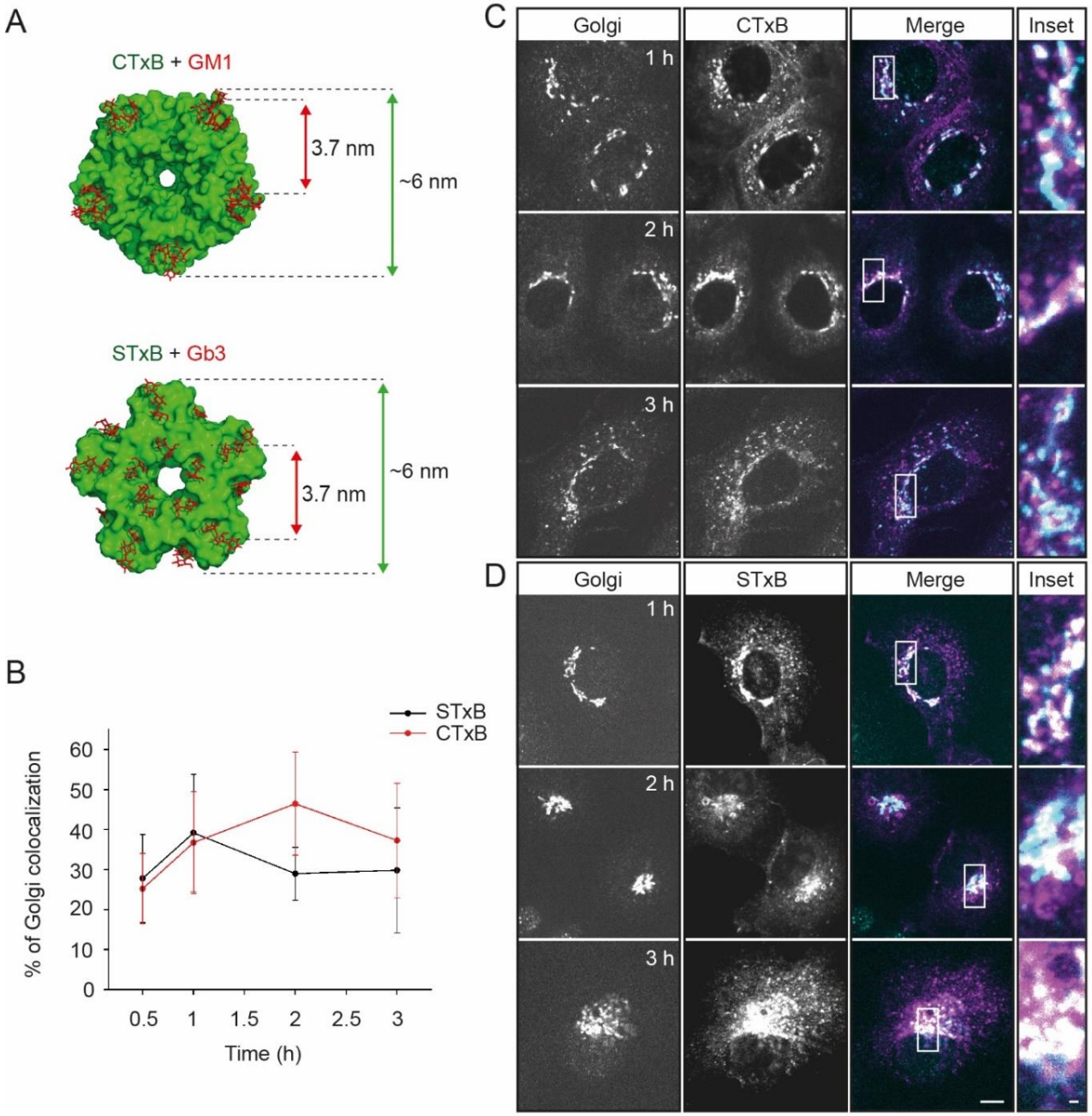

Figure 2.17. AB_5 toxins traffic through the Golgi apparatus. A) The organization of the lipid binding sites on AB5 toxins such as CTxB and STxB. PDB files: 1CT1 and 1BOS. **B)** Quantification of colocalization between CTxB/STxB and the Golgi apparatus. Means ± S.D. **C)** Fluorescence micrographs from a time-course experiment of endocytosis showing the distribution of CTxB in CV1 cells immunostained with anti-GM130 antibodies to mark the Golgi. CV1 cells were kept at 4 ˚C for 10 min before incubation with 5 µg of CTxB for 30 min at 4 ˚C. The cells were then switched to 37 ˚C for the indicated time points before fixation and immunolabeling. **D)** Fluorescence micrographs from a time-course experiment of endocytosis showing the distribution of STxB in CV1 cells immunostained with anti-GM130 antibodies to mark the Golgi. CV1 cells were kept at 4 ˚C for 10 min before incubation with 5 µg of STxB for 30 min at 4 ˚C. The cells were then switched to 37 ˚C for the indicated time points before fixation and immunolabeling. Scale bar is 10 µm and 1 µm for inset. Magenta: toxins; Cyan: Golgi.

Chapter 2.2.5. A pentameric configuration of lipid-binding sites is not sufficient to target the Golgi

Given the specificity of Golgi trafficking of the AB5 toxins, I first checked whether any protein with a similar pentameric organization of lipid-binding sites would follow the same intracellular route. The core structural proteins (VP1s) making up the capsids of the polyomaviruses adopt a pentameric configuration of the ganglioside binding sites, spaced exactly 3.7 nm apart. Their nanoscale architecture is indentical to the toxins, even though there is no sequence similarity between them (**Figure 2.18**A).

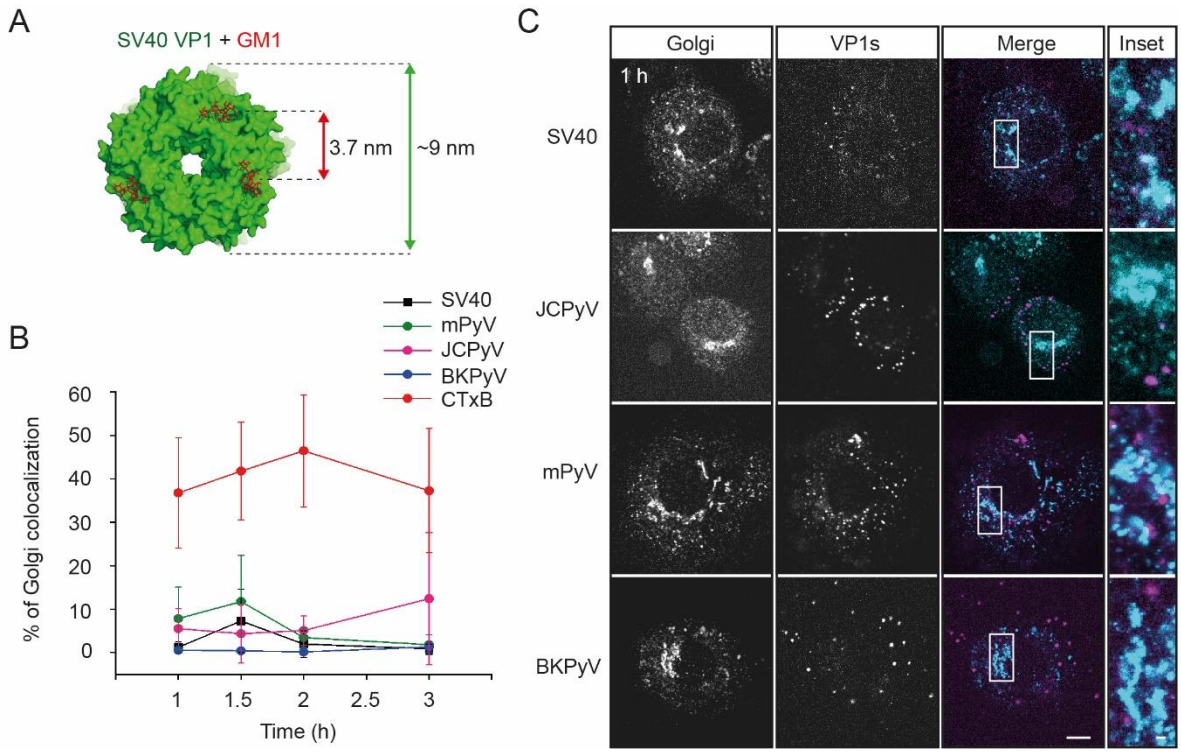

Figure 2.18. The pentameric polyoma VP1s do not traffic through the Golgi apparatus. A) The arrangement of lipid binding sites (Red) on the VP1 proteins used in the experiments. PDB file: 3BWR. These VP1s were recombinantly expressed and purified from truncated polyoma viral protein constructs that render them unable to self-assemble into VLPs. **B)** Quantification of colocalization between VP1s and Golgi apparatus. CTxB is used as a positive control for Golgi colocalization. Means ± S.D. **C)** Fluorescence micrographs from a time-course experiment of endocytosis showing the distribution of VP1s in CV1 cells immunostained with anti-GM130 antibodies to mark the Golgi. CV1 cells were kept at 4 ˚C for 10 min before incubation with 2 µg of the indicated VP1s for 30 min at 4 ˚C. The cells were then switched to 37 ˚C for the indicated time points before fixation and immunolabeling. Scale bar is 10 µm and 1 µm for inset. Magenta: VP1s; Cyan: Golgi.

Truncated versions of these proteins can render them unable to self-assemble into globular capsids. I purified the truncated mutant versions of the VP1 proteins of the SV40, JCPyV, BKPyV and mPyV polyoma-virions (**Annex 6.**). These proteins can bind to different glycolipid moieties on the membrane of cells, as described in the previous chapter. Next, I fluorescencetly labeled them and added them to CV1 cells

in order to determine their intracellular distribution in a time-course experiment. I performed a 3-hour pulse-chase assay together with master student Alexia de Caro, following the same protocol described previously for the AB_5 toxins. I then quantified their colocalization with the GM130 cys-Golgi marker and found that none of the VP1s overlapped significantly with the Golgi apparatus during the 3h time-course of the assay. The pentamers accumulated instead in round, vesicular structures resembling endosomes (**Figure 2.18**B, C), however this has not been quantified.

These results point out that the mere pentameric configuration of lipid-binding sites might not be sufficient to trigger the trafficking of exogeneous cargo to the Golgi apparatus. However, the VP1 proteins of the polyomaviruses have a much lower binding affinity for their ganglioside receptors[115] than the AB5 toxins, which might account for the loss in specifity of the intracellular trafficking.

Chapter 2.2.6. Synthetic polyvalent lipid-binding toxin mimics for targeted intracellular traffic

To further investigate the minimal requirements for Golgi targeting by exogeneous cargo, I developed three synthetic protein complexes that mimic the architecture of binding sites of CTxB. Each complex has an increasing number of binding sites arranged in a rather flat configuration and has high affinity for its lipid-anchored receptors, allowing for the investigation of the minimum number of binding sites required for targeted Golgi trafficking.

For the first toxin mimic, I coupled a tetrameric streptavidin protein to biotinylated-GFP molecules resulting in an approx. 13 nm by 5 nm synthetic toxin with possibly 1 to 4 GFPs on its surface (**Figure 2.19**A, top panel). I added these proteins to CV1 cells expressing a high-affinity GPI-anchored anti-GFP nanobody on their surface. I performed a 3 hour time-course pulse-chase assay to study the intracellular trafficking of these complexes and found that they do not colocalize with the Golgi apparatus at any time (**Figure 2.19**B, C). However, most of the complexes would only contain 1 bound GFP molecule at a time, with only a small fraction of streptavidins efficiently bound to 2 or 3 GFPs, as determined by size-exclusion chromatography (**Annex 7.**). It is possible that one GFP creates contacts to both biotin binding sites on one side of the streptavidin molecule, given the size of the GFP molecule and the abundance of biotinylation possibilities on it (due to its high lysine content). Therefore, the attachment of four GFP copies to one streptavidin molecule at a time might not be favorable.

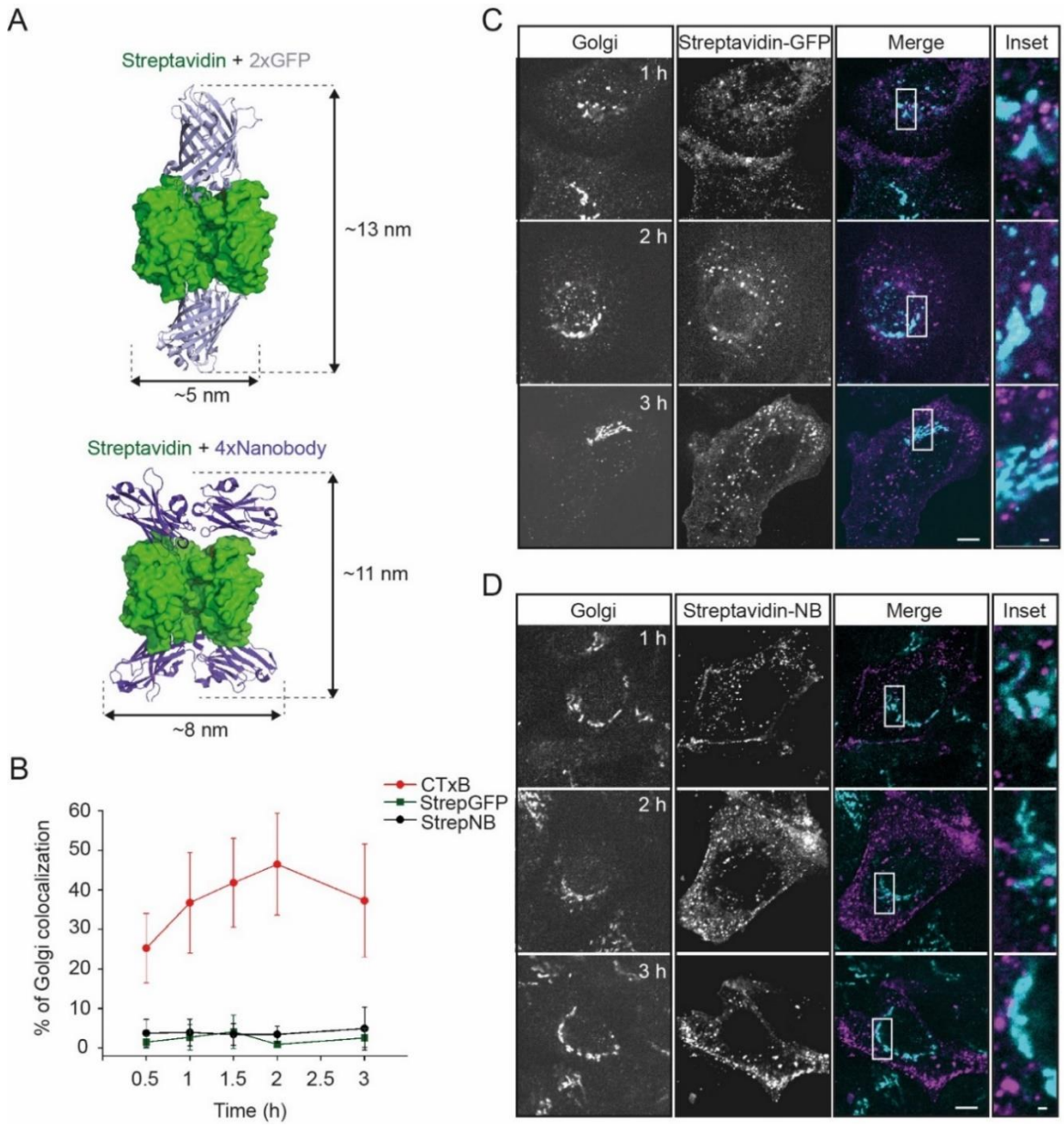

Figure 2.19. High-affinity synthetic toxin mimics with 1 to 4 receptor binding sites do not traffic to the Golgi apparatus. A) Cartoons of the synthetic toxin mimics used in the experiments. Streptavidin was conjugated to either recombinant GFP (top) or to recombinant high-affinity anti-GFP nanobodies (bottom). The complexes were then added to CV1 cells expressing either GPI-anchored anti-GFP nanobodies or GPI-anchored GFP. PDB files used: 4BX7 and 7SAH. **B)** Quantification of colocalization between the StrepGFP/StrepNB complexes and the Golgi apparatus. CTxB is used as a positive control for Golgi colocalization. Means ± S.D. **C)** Fluorescence micrographs from a pulse-chase assay showing the distribution of the StrepGFP complexes in CV1 cells immunostained with anti-GM130 antibodies to mark the Golgi. CV1 cells were kept at 4 ˚C for 10 min before incubation with 2 µg of the StrepGFP for 30 min at 4 ˚C. The cells were then switched to 37 ˚C for the indicated time points before fixation and immunolabeling. Scale bar is 10 µm and 1 µm for inset. **D)** Fluorescence micrographs from a pulse-chase assay showing the distribution of the StrepNB complexes in CV1 cells immunostained with anti-GM130 antibodies to mark the Golgi. CV1 cells were kept at 4 ˚C for 10 min before incubation with 2 µg of the StrepNB for 30 min at 4 ˚C. The cells were then switched to 37 ˚C for the indicated time points before fixation and immunolabeling. Scale bar is 10 µm and 1 µm for inset. Magenta: Strep-GFP/StrepNB; Cyan: Golgi.

To test whether a higher number of binding sites with high affinity towards their lipid-achored receptor are required to target the Golgi, I complexed the same streptavidin protein to four biotinylated anti-GFP nanobodies (streptavidin-NB) with high affinity for GFP (**Figure 2.19**A, bottom panel). There are only two lysine in the structure of these nanobodies and they are also smaller than GFP molecules, so it is likely that more than just one nanobodies can attach to the surface of the streptavidin. As receptors to this particles, I transfected a GPI-anchored GFP into CV1 cells that successfully locaziled at the plasma membrane. When I added the streptavidin-NB complexes to these cells and performed pulse-chase assays to follow their intracellular route, I found that they did not exhibit any Golgi colocalization and localized to endosomal-like structures instead (**Figure 2.19**B, D). This points out that a tetravalent organization of lipid binding sites on a flat, small molecule is not sufficient to trigger its traffic to the Golgi apparatus.

Next, I investigated whether a higher number of binding sites in a tight configuration with high affinity towards its lipid-anchored receptor would be enough to reroute the particles to the Golgi. Therefore, I used the Spyavidin complex[198] coupled to biotinylated GFP molecules. In brief, this complex is built from the linkage between 5 higher-affinity mutants of streptavidin, called traptavidin[199], organized in a star configuration (**Figure 2.20**A). The traptavidin mutants had each one inactive biotin binding site, termed dead streptavidin subunits. The dead subunit contained instead a short split tag used to bind to other dead streptavidin subunits containing the pairing split tag as represented in **Figure 2.20**A. The resulting Spyavidin molecule can bind up to 12 copies of biotinylated GFP. To bind these Spyavidin-GFP complexes to cells, I transiently expressed a GPI-anchored anti-GFP nanobody in CV1 cells, similar to the previous experimental set-ups. I then performed time-course pulse-chase assays and quantified the colocalization between Spyavidin-GFP and the Golgi marker GM130. I found almost no colocalization between the two channels at any time point (**Figure 2.20**B, C), but observed that Spyavidins accumulate in endosomal-like structures instead.

Taken together, these results point out that a high number of lipid binding sites on a flat particle resembling the architecture of AB_5 toxins is not sufficient to trigger the trafficking of these particles through the Golgi apparatus. There must be some other factors or molecular players responsible for the targeting of the bacterial toxins to this organelles, such as secondary receptors or intracellular signalling pathways.

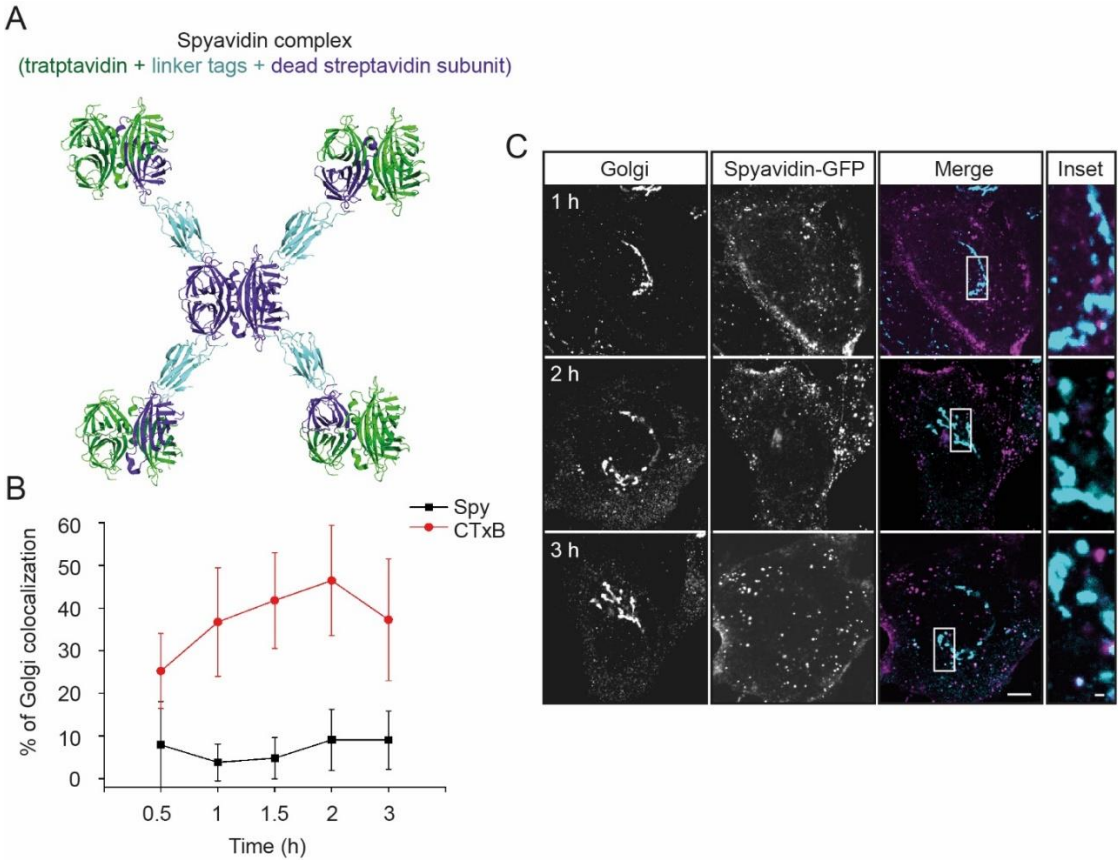

Figure 2.20. High-affinity synthetic toxin mimics with 12 receptor binding sites do not traffic to the Golgi apparatus either. A) The synthetic toxin mimic backbone consisting of Spyavidin: Traptavidins, a high affinity Streptavidin version (active binding sites in green, inactive mutated binding sites in purple) were linked together via the SpyTag/SpyCatcher system. GFP was subsequently conjugated to Spyavidin, resulting in a larger Spyavidin-GFP with 12 binding sites. The complexes were then added to CV1 cells expressing GPI-anchored anti-GFP nanobodies on the outer leaflet of the plasma membrane. **B)** Quantification of colocalization between the SpyavidinGFP complex and the Golgi apparatus. CTxB is used as a positive control for Golgi colocalization. Means ± S.D. **C)** Fluorescence micrographs from a pulse-chase assay showing the distribution of the SpyavidinGFP complexes in CV1 cells immunostained with anti-GM130 antibodies to mark the Golgi. CV1 cells were kept at 4 ˚C for 10 min before incubation with 2 µg of the SpyavidinGFP for 30 min at 4 ˚C. The cells were then switched to 37 ˚C for the indicated time points before fixation and immunolabeling. Scale bar is 10 µm and 1 µm for inset. Magenta: SpyavidinGFP; Cyan: Golgi.

Chapter 2.2.7. Discussion

In this chapter of the thesis, I have studied the intracellular trafficking mechanisms of non-enveloped viruses and bacterial toxins. I found that none of the members of the polyomavirus family traffic through the Golgi apparatus on their way to the endoplasmic reticulum, but rather go through the endo-lysosomal network instead (**Figure 2.11** and **Figure 2.12**). My results correlate well with previous findings in literature[106,109,110,135,200]. I made use of the synthetic virus-like-particle and lipid-receptor system I have previously developed in the first results chapter of this thesis to ask if a multivalent, globular arrangement of

lipid binding sites is sufficient to target lysosomes. In brief, I have purified a 37-nm in diameter globular particle that bears 180 copies of GFP distributed symmetrically all over its surface named GEM and added it to cells expressing a high-affinity GPI-anchored anti-GFP nanobody as a receptor. By employing pulse-chase assay in which the transport of exogeneous cargo throughout organelles can be traced in a time-course experiment, I have determined that these artificial GEMs become internalized and trafficked through the endo-lysosomal system as well (**Figure 2.13**). The GEMs were not found in the Golgi apparatus at any time, similarly to polyomaviruses (**Figure 2.14** and **Figure 2.15**). However, there was a clear loss in the specificity of trafficking to lysosomes observed for the synthetic particles as compared to the polyomas (**Figure 2.12** and **Figure 2.14**). Moreover, I found that a possible reason for specific targeting to lysosomes might be the involvement of additional receptors that the polyoma-virions can bind to (**Figure 2.16**), a feature lacking completely for the artificial GEMs.

Next, I could reproduce the already established trafficking of several AB_5 bacterial toxins to the Golgi apparatus (**Figure 2.17**). In trying to understand the minimal requirements to trigger exogeneous cargo sorting through this pathway, I first investigated whether the pentameric structural proteins of various polyoma-virions that adopt an identical configuration of lipid binding sites as the toxins would be transported to the Golgi as well. Surprisingly, none of the polyomavirus VP1s were found to traffic to the Golgi apparatus at any time point (**Figure 2.18**). Since the binding affinity of the polyomas for their glycolipid receptors are much lower than the affinities of the toxins, I next developed artificial toxin mimics with high affinity for lipid-anchored receptors and distinct number and configuration of binding sites on a flat surface. I found that none of them could reproduce the trafficking behaviour of bacterial toxins to the Golgi apparatus (**Figure 2.19** and **Figure 2.20**). These results provide a first glimpse into the minimal requirements for exogeneous cargo targeting to the Golgi apparatus and pave the way for further investigation into the biophysical mechanisms behind it.

Multivalent lipid binding is essential for viral traffic

The active life of a polyomavirus can be represented as: 1) Attachment to the cell surface 2) Lateral diffusion on the membrane and receptor clustering 3) Membrane deformation due to multivalent lipid binding 4) Clathrin-independent endocytosis in parallel to 5) Activation of cellular signalling pathways 6) Intracellular transport 7) Pore formation and release of genomic material at the ER. These processes are interconnected and disruption of one step leads to the disruption of the rest. Therefore, the specificity of intracellular trafficking through the lysosomes must be encoded in the previous lifetime processes undertaken by the virions.

Attachment to the surface of the cells occurs via the pentameric structural protein VP1 which contains 5 receptor binding sites spaced 3.7 nm apart. Each individual binding site has a low affinity for the ganglioside GM1 receptor, in the mM range[115]. However, its multivalent lipid binding to up 360 lipids leads to avidity effects and renders the interaction with the membrane virtually irreversible. Is it sufficient for one virion to bind 4 receptors simultaneously in order to stabilize the attachment to the membrane[118]. This leads to lipid clustering and the formation of liquid ordered nanodomains in the membrane, which facilitate membrane deformation and internalization. My work here aims to understand the importance of 1) the pentameric arrangement of binding sites and 2) the clustering of lipids induced by multivalent binding on the intracellular trafficking mechanism of virions. I looked at the transport and intracellular distribution of the artificial GEMs in a time-course experiment and found similarities to the polyoma-virion traffic. Both the GEMs and the polyomas were found in endosomes and in lysosomes after internalization. While up to 80% of the total amount of polyoma VLPs in a cell end up in lysosomes a few hours after internalization, only around 30% of the total amount of GEMs in a cell end up in lysosomes during a 6 hour period (**Figure 2.12** and **Figure 2.14**). Another 30% of GEMs end up in late endosomes. Since the GEMs do not have a solely pentameric architecture of binding sites, these results suggest that this specific configuration of lipid binding sites is dispensable for endo-lysosomal trafficking. The affinity of the particle for its receptor is also 7 orders of magnitude higher than the affinity of polyomas for their ganglioside receptors, but this does not seem to be crucial for endo-lysosomal targeting either. The homogeneous distribution of the amount of GEMs between different endosomal species instead of their accumulation in lysosomes might be a consequence of the inherent differences between the receptors of the particles and the flexibility of their interaction with them.

Viral traffic may be a consequence of the mode of interaction with the lipidic receptors

Viral tropism plays an important role in the ability of viruses to infect cells. Polyomas bind specifically to certain glycolipid species enriched on their host cells that contain one or more sialic acids in their structure. Upon modification of one single amino acid residue in the binding pockets of these viruses, they can lose their ability to infect cells[116] or lose their ability to bind to their receptor gangliosides[114,201,202]. Moreover, when binding to ganglioside receptor variants with shorter acyl chains, viruses cannot productively infect cells anymore[85]. In comparison, the artificial GEMs bind to a non-endogenous GPI-anchored protein on the surface of the cell. These proteins are post-translationally modified in the ER with a C-terminal GPI-anchor consisting of an ethanolamine liked to an oligosaccharide that in turn is attached to the inositol head group of a phosphatidylinositol. The two fatty acid chain of the phosphatidylinositol are inserted into the membrane, but it remains unclear how long or unsaturated these chains are. There have been many modifications of the type and length of the acyl chains of GPI-anchored proteins found across different

organisms[203,204] and it is not yet understood how these modifications are chosen by cells and to what extent they can influence the properties of the plasma membrane. It is possible that the structure of the fatty acid backbone of the receptors has an influence on the receptor clustering ability of the viral particles/ GEMs. Since the polyomas interact very tightly to their receptors, they are able to induce phase separation in the plasma membrane, however the GEMs interact more loosely with their receptors and perhaps are not able to induce the same liquid ordered domains. The formation of these domains upon viral binding is crucial to trigger certain intracellular signalling processes required for organelle sorting of the virions after uptake and might be lacking entirely for the GEMs. This could explain why they do not accumulate in lysosomes to the same extent as polyoma-virions.

Cholesterol modulates intracellular signalling induced by viral attachment

I found in my assays that the reduction of the amount of cholesterol in the membrane of cells did not significantly alter the internalization amount of GEMs in cells (**Figure 2.7** of the previous results chapter). Interestingly, cholesterol inhibition has a major influence on polyoma-virion entry, both in my assays (**Figure 2.7**) and in literature[70,85,107,110]. The ganglioside receptors of the polyoma-virions are prone to cluster together with cholesterol[169] and form membrane domains known as lipid-rafts[205]. When virions bind to such microdomains in the membrane, their diffusion is significantly reduced[117]. Is it very likely that such lipid domains mediate transmembrane interactions, for example with the cortical actin skeleton[117], which might play a role in the activation of intracellular signalling cascades after viral attachment. It is interesting to note that different polyoma-virions activate different signalling pathways[110,137,206], perhaps due to their association with different ganglioside species. The activation of such signalling cascades during viral entry might provide the specificity of their trafficking through the endo-lysosomal system. Since GEM uptake is independent of cholesterol, there might a possibility of no intracellular signalling occurring during their internalization. This could lead to a spreading of the GEMs throughout various endosomal organelles. Generally, GPI-anchored proteins integrate together with cholesterol in nanoscale domains formed by transmembrane interactions with cortical actin[193]. However, when an above-endogenous abundance of GPI-anchored proteins is induced in cells by transient expression, as is the case in my experiments, lipid clustering might not occur for the non-native species, or they might fail to be integrated in already formed GPI-anchored protein-cholesterol domains. The failure of GEMs to bind to preformed liquid-ordered domains like the polyomas do, could further explain the loss of accumulation of the GEMs in lysosomes.

In addition, GPI-anchored protein crosslinking leads to caveolin recruitment at the budding site[180]. In my assays, a fraction of the GEM-endocytic pits is caveolin positive (**Figure 2.9** of the previous results chapter). Caveolin is known to modulate the sorting of certain virions to endosomes[63,107,109] and might act

upon GEM trafficking as well. The precise extent to which caveolin mediates intracellular trafficking, both for polyoma-virions and for the GEMs, remains to be investigated.

Exogeneous cargo sorting could occur in early endosomes instead

Early endosomes are known to be the sorting station of the cell. There have been different early endosomal populations described in literature[132,207,208], depending on their membrane composition and presence or absence of effector molecules on their surface. Rabs are known to regulate the maturation of endosomes to lysosomes and Rab5 is required for conversion into late endosomal compartments[208,209]. In the CLIC/GEEC pathway, nascent endocytic pits enriched in GPI-anchored proteins fuse with a subtype of endosomes devoid of Rab5 effector protein[93]. A fraction of these endosomes might eventually fuse with Rab5-positive endosomes[93] and the rest of them fuse with recycling endosomes instead[210,211]. Since GEMs enter cells through clathrin-independent endocytosis, they might be sorted through Rab5-deficient early endosomes and from there they get dispersed in various endosomal structures, instead of accumulating in lysosomes.

In addition, the maturation of Rab5-positive early endosomes into late endosomes is dependent on the acidification of their lumen. These compartments need to fuse with incoming vesicles containing hydrolases in order to become lysosomes. As this fusion occurs, the intralumenal pH drops. The acidification of the endosomes triggers receptor release by exogeneous cargo and the receptors become recycled back to the plasma membrane as a consequence, where they mediate the uptake of other incoming viruses. The inhibition of endosomal acidification strongly inhibits polyoma viral internalization and subsequent intracellular traffic[110,135]. However, the inhibition of acidification did not alter GEM uptake in my assays (**Figure 2.7**) as they might be sorted to GEEC compartments negative for Rab5 for which acidification is not essential. This could explain why GEMs fail to accumulate over time in lysosomes. In the future, it would be useful to investigate to which early endosomal subpopulation the GEM-endocytic pits fuse to.

The involvement of secondary receptors in the cellular entry of polyoma-virions

One surprising finding in my study was the lack of MCPyV binding to *in vitro* model membranes containing its ganglioside receptor, GT1b (**Figure 2.16**). The MCPyV is a virus that induces skin cancer in immunosuppressed individuals and the elderly population[212]. GT1b has been identified as a co-receptor for the MCPyV[213] and the virus displays a high infection preference for dermal fibroblasts[214,215]. Dermal fibroblasts are localized in the dermis and are responsible for generating much of the extracellular matrix anchoring the dermis to the epidermis layers in the skin. Collagen, elastic fibers, proteoglycans and glycosaminoglycans (GAGs) are the principal components of the skin layers. Since MCPyV exhibits a high tropism for the epidermis cells, there is a possibility that it initially binds to a component of the extracellular

matrix to promote its attachment to cells through subsequent interaction with the ganglioside receptor GT1b. To test this, I created GUVs containing an artificial GAG-mimetic compound synthesized by the lab of Prof. Laura Hartmann at the Heinrich-Heine-Universität Düsseldorf. The GAG-mimetic is a cholesteryl-bound, highly-sulphated polymer whose incorporation into the membranes can be verified by its fluorescence signal around the circumference of the vesicle (**Figure 2.16**B). I observed that the MCPyV binds well to GUVs containing the GAG-mimetic, both in the presence and in the absence of the GT1b ganglioside (**Figure 2.16**B). Addition of the GT1b ganglioside in the composition of the vesicles did not cause a higher degree of viral binding (**Figure 2.16**B). However, the GAG-mimetic is indispensable for viral attachment to membranes, pointing out the importance of co-receptors in the successful cellular attachment and entry of polyomaviruses. The interaction with co-receptors was observed for other members of the polyomavirus family as well[150,216–221]. The exact role of the secondary receptor binding in the viral intracellular specificity of traffic still remains to be determined. Since the artificial GEMs do not interact with any other molecular player except for their GPI-anchored anti-GFP nanobody receptors (**Figure 2.5** of the previous chapter), it would be possible that certain intracellular signalling pathways do not become activated upon GEM entry and fail to provide lysosomal-specificity in its intracellular trafficking pathway. However, the activation of signalling cascades by GEM binding and entry in cells still remains to be investigated.

Golgi targeting of AB_5 bacterial toxins: due to binding site architecture alone?

AB_5 toxins bind to glycolipids in the plasma membrane in an identical pentameric configuration as the polyomaviruses, with individual binding sites spaced precisely 3.7 nm apart (**Figure 2.17**A). These toxins also induce the formation of liquid ordered domains as they bind to the plasma membrane. These domains subsequently facilitate the formation of membrane curvature and the bacterial toxins enter cells predominantly through clathrin-independent pathways. So how come despite all these similarities between polyomas and toxins, the two pathogens follow completely different intracellular routes on their way to the ER? Polyomas go through the endo-lysosomal system as discussed above, while the toxins pass through early endosomes directly to the Golgi and bypass late endosomes and lysosomes. Considering that the only resources these pathogens have at hand to target one organelle or another are found in their structure, or in their mode of interaction with their lipidic receptors, there are only two possibilities to explain their differential sorting inside the cell: multivalent lipid binding in a flat vs. globular configuration and/or engagement of additional secondary receptors at the plasma membrane/early endosome.

The first possibility is that multivalent lipid-receptor binding in a flat geometry triggers Golgi targeting. The main goal of the second part of this thesis was to test this hypothesis. It is already known that CTxB coupled to globular quantum dots gets re-routed to the endo-lysosomal system[222]. This suggests that a globular arrangement of lipid binding sites might indeed target cargo to lysosomes, while a more flat-like

configuration of binding sites (like in AB_5 toxins) might target the Golgi instead. To test this, I purified a mutated version of the pentameric core structural proteins VP1 of several polyoma-virions, that is truncated and unable to self-assemble into globular capsids as a result (**Annex 6.**). However, these pentamers could still bind to their glycolipid receptors. I found that they do indeed become endocytosed in cells and traffic to unidentified endosomal compartments (**Figure 2.18**). No VP1 pentamers accumulated in the Golgi apparatus in a 3 h time course experiment. Several similar studies in literature performed longer time course experiments with the VP1s and found no Golgi colocalization as well[106,223,224]. These results point out that the specific pentameric configuration of ganglioside binding sites spaced 3.7 nm apart is not the main culprit for Golgi targeting by bacterial toxins.

Golgi targeting by AB_5 bacterial toxins: due to high affinity multivalent binding?

The main difference between polyoma VP1 pentamers and AB5 toxins is the binding affinity to their lipid receptors, which is very low for polyomas (in the mM range)[115] and very high for toxins (in the pM range)[120]. To test if both a flat, multivalent configuration of binding sites and high affinity for lipid receptors are needed to target the Golgi, I designed artificial toxin mimics that had 1) a distinct number of binding sites arranged on a flat configuration and 2) a pM affinity for lipid-anchored receptors in the membrane of cells.

The first toxin mimic was constructed from a streptavidin molecule complexed to biotinylated GFP proteins (**Figure 2.19**A) and its corresponding receptors were GPI-anchored anti-GFP nanobodies transiently expressed in cells. I found that most of the streptavidins were bound to 2 or maximum 3 copies of GFP and no complex with 4 copies of GFP were formed (**Annex 7.**), even though streptavidin is a tetrameric protein that can potentially bind up to 4 biotins. However, the GFP molecules are quite large and contain many lysine residues where biotinylation is likely to occur, so one GFP might bind to both binding sites on the same side of the streptavidin. In any case, the streptavidin-GFP complexed did not traffic to the Golgi, but to vesicular compartments in the cell, regardless of the number of GFPs on its surface (**Figure 2.19**B). It would appear from these results that only 2 or 3 high-affinity lipid binding sites in close proximity are not enough to replicate bacterial toxin traffic. This is further supported by previous studies where antibodies against the GM1 and GD1a gangliosides containing only two binding sites were localized in recycling endosomes[225].

To increase the number of high affinity lipid binding sites, I created a second streptavidin-based toxin mimic with a reverse configuration: biotinylated high-affinity anti-GFP nanobodies were complexed to a tetrameric streptavidin (**Figure 2.19**A). Given the smaller size of the nanobodies and the reduced number of possible biotinylation sites (only two lysine residues in the Lag16 nanobody), it is likely that all four binding sites on the streptavidin are occupied by individual nanobodies. These complexes were then added to cells expressing GPI-anchored GFP molecules on their surface and their intracellular distribution was

investigated. However, no Golgi colocalization was observed either (**Figure 2.19**B), most likely because four binding sites are still not enough to promote lipid clustering to the same extent as the pentameric toxins do. It was shown that CTxB mutants or other lectin mutants with fewer number of functional binding sites that the wild type pentameric toxins/lectins failed to induce lipid clustering and had reduced cellular toxicity[125,226].

To ensure a sufficient number of high-affinity lipid binding sites in a flat configuration, I build a third version of the bacterial toxin mimic, this time composed out of a larger streptavidin-mutant network, bound together by small tags in between, called Spyavidin (**Figure 2.20**A). In total, the Spyavidin displays 12 functional biotin binding sites (represented in green) on a rather flat configuration. I added biotinylated GFP to form the toxin mimic and then added this complex to cells expressing a GPI-anchored anti-GFP nanobody on their surface. Unfortunately, I was not able to observe any Golgi colocalization for this toxin mimic either (**Figure 2.20**B, C).

Golgi targeting of AB_5 bacterial toxins: other molecular players

Taken together, all these results prove that the molecular mechanism of Golgi targeting by bacterial toxin relies on more than just a flat, multivalent arrangement of high-affinity lipid binding sites. Other factors are crucial for this process to occur, and they could be involved either 1) at the membrane entry site of toxins or 2) at the early endosomal sorting station.

At the endocytic entry site of the toxins in the plasma membrane, cholesterol plays an important role as already discussed in the previous paragraphs. Since the receptors for the toxin mimics created here are also GPI-anchored proteins as in the case of the artificial virions GEMs, there might be a lack of cholesterol dependence in the entry mechanism of these artificial toxins as well, like for the GEMs. This could lead to a loss of specificity in intracellular trafficking. Moreover, toxins are known to become internalized through both clathrin-dependent and clathrin-independent processes and these associations might be critical in the specificity of trafficking[103,196,227]. Particularly, the association between clathrin and CTxB is apparently indispensable for Golgi traffic[228]. The precise entry mechanism for the artificial toxins used in this study has not been investigated and could potentially provide more information into the behaviour of these particles. Furthermore, I have determined that polyomavirus entry is aided by molecular secondary receptors on the plasma membrane (**Figure 2.16**) and that they play an important role in the uptake and traffic of the viruses. Both Shiga toxin and Cholera toxin have been found to interact with other proteins on the membrane as well[127,229] and these interactions might prove to be crucial for their correct targeting inside the cell. Further investigation is needed into the role of secondary receptor attachment during intracellular trafficking.

As discussed in the previous sections, sorting of exogeneous cargo could also occur at the early endosomal level. An important, well-known class of coat proteins acting at the endosomal level is the retromer complex. The retromer is a protein complex that has been shown to be involved in the trafficking and recycling of proteins and transmembrane receptors from endosomes to the trans Golgi network[230]. Some of the exogeneous cargo destined for the Golgi might contain a certain sequence of hydrophobic or aromatic residues in its structure that can be recognized by the retromer complex. For example, the STxB associates with it in the early endosomes whose membranes are enriched in PI(3)P and some components of the retromer preferentially interact with these lipid enriched domains[231]. The STxB also associates with another retromer complex protein in recycling endosomes that could also mediate its subsequent traffic to the Golgi[232]. How exactly the STxB realizes its own association with proteins from the retromer complex still remains to be determined. In addition, trafficking of both STxB and CTxB from the early endosomes to the Golgi is dependent on other proteins enriched on early endosomal membranes, such as Rab6[233,234] and SNARE complexes[233,235,236], but little is understood about the exact role these proteins play in providing trafficking specificity to cargo.

Overall, the retrograde transport of AB_5 toxins from the early endosomes to the Golgi apparatus seems to be triggered by additional factors not studied in this work. Multivalent lipid binding is important, but not enough. In the future, more studies need to be performed to further understand the minimal requirements for Golgi targeting, based on the premise that mere high-affinity, multivalent lipid binding sites arranged in a flat configuration is not sufficient.

Chapter 3. Conclusions and future perspectives

To sum up, in this thesis I have studied the biophysical mechanism of multivalent lipid binding by pathogens to trigger membrane deformation, endocytosis and intracellular traffic. For this, I have developed artificial protein complexes that mimic the nanoscale architecture of lipid-binding sites adopted by non-enveloped viruses (i.e. the polyomavirus family) and bacterial toxins (i.e. CTxB and STxB).

First, I have determined that globular, multivalent lipid binders (artificial viral mimics) can replicate the behaviour of real polyomaviruses and promote their uptake into cells by inducing membrane deformation. Furthermore, I investigated the role of the adhesion energy of viral mimics in facilitating their internalization in cells and found a clear-cut threshold necessary for efficient membrane deformation and clathrin-independent endocytosis. My results suggest that multivalent lipid binding by any globular particles is a general biophysical principle employed to gain access to cells. Moreover, this study provides a fresh understanding of the minimal requirements to trigger clathrin-independent endocytosis and I believe the artificial experimental system developed in this thesis can be expanded further to gain more insight into the biophysics of viral entry. For example, one could purify GEMs of different sizes[237] bearing more or less number of lipid-binding sites than the GEMs employed in this study. This could provide information about the relationship between multivalency and the adhesion energy necessary for membrane deformation. In my opinion, it would be interesting to test how the threshold energy needed for triggering deformation would change when GEMs are larger or smaller than the 37-nm in diameter one used here. In addition, it would be useful to further engineer the GEMs as a drug delivery system. One could potentially encapsulate drugs or small DNA fragments into the GEMs. Also, the GFP molecules surrounding the GEMs could be switched for nanobodies against lipids or other native proteins to allow this system to target cells or tissues without the need for introducing the receptors exogenously.

Secondly, I determined that a mere multivalent architecture of lipid binding sites arranged on a flat surface similar in size to the B-subunit of bacterial toxins is not alone sufficient to provide the specificity of intracellular trafficking to the Golgi apparatus. It seems that neither a precise pentameric configuration of binding sites nor a high-affinity multimeric arrangement of binding sites on artificial toxin mimics triggers the particles to go to the Golgi. There must be other requirements involved in this mechanism that have not been investigated in this work. For example, one could engineer a toxin mimic that has a stiffer arrangement of binding sites, as the GFP molecules attach to the toxin mimic scaffolds might interact to loosely with the lipid-anchored receptors in the plasma membrane. Because of this, lipid clustering might not induce the formation of liquid ordered domains in the membrane and might not trigger the intracellular signalling cascades required to provide trafficking specificity. Moreover, there might be crucial secondary receptors

involved in the entry and traffic of bacterial toxins as mentioned above, that are not employed in the attachment and uptake of the artificial toxin mimics developed here. Additionally, the entry of bacterial toxins occurs through both clathrin-dependent and clathrin-independent endocytosis. It is possible that the involvement of clathrin in the entry of toxins is crucial for the correct sorting of the toxins. In the future, it would be interesting to investigate the relationship between the endocytic mechanism employed by exogeneous cargo and their intracellular trafficking routes. Even though Golgi targeting could not be reproduced using my artificial toxin mimics, my work explores the minimal requirements for targeting pathogenic cargo to certain organelles in the cytoplasm, such as the Golgi apparatus or lysosomes. The results obtained here provide a starting point for further investigation into the exact molecular mechanisms causing the specificity of intracellular traffic.

The main limitation of the artificial systems designed in this study to investigate the entry and trafficking requirements of multivalent lipid binding pathogens is its inability to be tuned for secondary receptor binding. Secondary receptors are involved in the entry of both non-enveloped viruses and bacterial toxins and could have detrimental effects on their endocytosis behaviour and intracellular trafficking. However, the GEMs exclusively bind to anti-GFP nanobodies. Even exchanging the GFPs on the GEMs to other proteins would still only allow for one receptor binding at a time. The second limitation of the artificial systems developed here is their inability to trigger intracellular signalling cascades due to their binding to a transiently expressed receptor. However, I envision this limitation could be circumvented by engineering the GEMs to bind to endogenous lipids or transmembrane protein receptors, that would activate signalling cascades upon ligand binding. Investigating how such signalling events could modulate subsequent intracellular trafficking of exogeneous cargo could provide a deeper understanding of the minimal requirements for its sorting to specific organelles.

All in all, the present work provides an experimental paradigm that enables the study of clathrin-independent endocytosis and intracellular traffic specificity and opens the possibility to be modulated in future studies to gain insight into the molecular mechanisms and biophysics behind endocytosis and traffic.

Materials and methods

Materials

Lipids were purchased either from Avanti Polar Lipids: DOPC (1,2-dioleoyl-sn-glycero-3-phosphocholine), from Enzo Life Sciences: GM1 (Ganglioside GM1 sodium salt (bovine brain)), GD1a (Ganglioside GD1a disodium salt (bovine brain)), GD1b (Ganglioside GD1b disodium salt (bovine brain)), GT1b (Ganglioside GT1b trisodium salt (bovine brain)) and from ThermoFisher Scientific: β-BODIPY™ FL C12-HPC (Invitrogen), DiIC18(3) stain (Invitrogen). Transferrin from Human Serum, Alexa Fluor™ 488 Conjugate (Invitrogen) was purchased from ThermoFisher Scientific, purified recombinant Enhanced Green Fluorescent Protein (EGFP) was purchased from Chromotek. Bafilomycin A1 was purchased from InvivoGen, Nystatin and Progesteron were purchased from Sigma-Aldrich. Clathrin Heavy Chain siRNA (Human CLTC, sequence: GGUUGCUCUUGUUACG, ID: s475) and Negative Control#1 siRNA Silencer Select were purchased from ThermoFisher Scientific. Purified Spyavidin was bought commercially from molox GmbH. Purified Streptavidin was bought commercially from Sigma-Aldrich. Recombinant CTxB and STxB were purchased from Sigma-Aldrich. Purified LaG16 nanobody was produced in house as previously described[238]. Mouse anti-GM130 antibody was purchased from BD Biosciences.

Methods

Virus-like-particles.

Polyomavirus-like-particles were assembled from purified VP1 proteins obtained from Abcam, namely Simian Virus 40 (ab74565), mouse polyomavirus strain RA (ab74571), JC polyomavirus (ab74569) and BK polyomavirus, strain AS (ab74567) according to the manufacturer's specifications. Alexa Fluor 647-NHS was covalently coupled to the assembled virus-like-particles in 0.2 M NaHCO3 at pH 8.3 using a 10-fold molar excess of the dye relative to VP1 protein. Unbound dye was removed by two subsequent washing steps on pre-equilibrated Zeba columns (40 KDa cut-off, Thermo Scientific) in PBS buffer.

Toxin-mimic preparation.

1. **Streptavidin-GFP.** GFP was added to Streptavidin in PBS buffer using a 10-fold molar excess of the GFP relative to Streptavidin and incubated overnight at 4 ˚C while shaking. The next day, the unbound GFP was removed by two subsequent washing steps on pre-equilibrated Zeba columns (40 KDa cut-off, Thermo Scientific) in PBS buffer.
2. **Streptavidin-nanobody.** Purified LaG16 was added to Streptavidin in PBS buffer using a 20-fold molar excess of the LaG16 relative to Streptavidin and incubated overnight at 4 ˚C while shaking.

The next day, the unbound LaG16 was removed by two subsequent washing steps on pre-equilibrated Zeba columns (40 KDa cut-off, Thermo Scientific) in PBS buffer.

3. **Spyavidin-GFP.** GFP was added to Spyavidin in PBS buffer using a 20-fold molar excess of the GFP relative to Spyavidin and incubated overnight at 4 ˚C while shaking. The next day, the unbound GFP was removed by two subsequent washing steps on pre-equilibrated Zeba columns (40 KDa cut-off, Thermo Scientific) in PBS buffer.

Gene cloning and plasmids.

Nanobody sequences (Clone IDs: LaG16-G_4S-2, LaG-16, LaG-21, LaG-17, LaG-42, LaG-18 and LaG-11 from [145]) were codon-optimized for expression in mammalian cells and cloned into a Twist Amp High-Copy vector after gene synthesis (Twist Bioscience), incorporating BamHI and XhoI restriction sites at 5′ and 3′ ends, respectively. Next, the nanobody sequences were subcloned into a pEGFP-N1 GPI-GFP vector in between the LPL-signal peptide and the GPI-anchor, replacing the GFP sequence. Successful insertion was verified by gene sequencing (Microsynth AG). GEM-GFP sequence[239] was codon-optimized for expression in *Escherichia coli* and cloned into a pET-29b(+) vector in between the NdeI and XhoI restriction sites after gene synthesis (Twist Bioscience). Lamp1-mRFP, Lamp1-EGFP, Rab7-mRFP, Clathrin light chain–mRFP, Caveolin1-mRFP and cytosolic RFP were a kind gift from the Ari Helenius laboratory. RFP Dynamin2 K44A and RFP Dynamin-2 Wild Type were a gift from the Jennifer Lippincott-Schwartz laboratory (Addgene plasmid # 128153 and Addgene plasmid # 128152)[240]. The codon-optimized MCPyV VP1- and VP2-coding plasmids used were pwM (Addgene plasmid 22515) and ph2m (Addgene plasmid 22518), as described previously[241]. The plasmids encoding the truncated VP1 proteins of SV40, JCPyV, BKPyV and mPyV were kind gifts from the Thilo Stehle lab.

Recombinant expression and protein purification:

1. **GEM-GFP purification procedure.**

GEM-GFP particles were expressed under a T7 promoter in *E.coli* BL21 strain in complex autoinduction medium (1% N-Z-amine AS, 0.5% yeast extract, 25 mM Na_2HPO4, 25 mM KH_2PO_4,50 mM NaH_4Cl, 5 mM Na_2SO_4, 2 mM $MgSO_4$, 0.2x trace metals, 0.5% glycerol, 0.05% glucose, 0.2% α-lactose, 30 µg/ml kanamycin) at 37 ˚C for 4 h, followed by further incubation at 21 ˚C for 72 h. The bacterial pellet was resuspended in lysis buffer (50 mM Phosphate buffer, 50 mM NH_4Cl, 40 mM imidazole, 700 mM NaCl, 10% Glycerol, 1 mg/ml lysozyme, 10 µg/ml DNAse I, protease and phosphatase inhibitor cocktail (Thermo Scientific) at pH 7) at 4 ˚C for 30 min and subsequently heated up at 55 ˚C for 30 min. The lysate was sonicated and cleared by centrifugation (7000 x g, 40 min, 4 ˚C). The supernatant was added to a pre-equilibrated Ni-NTA-bead gravity flow column, washed with washing buffer (50 mM Phosphate buffer, 50

mM NH_4Cl, 40 mM imidazole, 700 mM NaCl, 10% Glycerol, protease and phosphatase inhibitor cocktail at pH 7) and eluted with elution buffer (50 mM Phosphate buffer, 50 mM NH_4Cl, 500 mM imidazole, 700 mM NaCl, 10% Glycerol, protease and phosphatase inhibitor cocktail at pH 7). The elution was then dialyzed overnight at 4 ˚C into protein buffer (50 mM Phosphate buffer, 50 mM ammonium chloride, 700 mM NaCl, 5% Glycerol, protease and phosphatase inhibitor cocktail at pH 7). Next, a size-exclusion chromatography run on a Superdex 200 Increase 10/300 GL column was performed in protein buffer. The fractions eluted in the void volume of the column were verified to contain GEM-GFP proteins by SDS-Page gel and by MALDI mass spectrometry. The fractions were then pooled, concentrated on a Amicon Ultra 100K (Merk Millipore) concentrator, stored at 4 ˚C and used in the first two weeks after purification.

2. Merkel cell polyoma virus-like-particle purification procedure.

The protocol for MCPyV purification was described previously[241]. In brief, MCPyV VP1 wild type was expressed in mammalian cells, HEK293T cells, a human embryonic kidney cell line carrying an integrated copy of the SV40 genome. To ensure high expression levels of the SV40 large T antigen, HEK293TT stable cell line was generated prior to the purification by further transfection with linearized pTIH plasmid and selection with hygromycin[242]. HEK293TT were next transfected with plasmids containing the VP1 and VP2 capsid proteins of the MCPyV. After 4 days, cells expressing the viral capsid proteins were harvested, washed with PBS buffer supplemented with 9.5 mM $MgCl_2$ and resuspended in lysis buffer (PBS supplemented with 9.5 mM $MgCl_2$,0.5% Triton X-100, 0.2% Benzonase (Sigma), 25 mM ammonium sulfate (pH 9), 1 µg/ml soybean trypsin inhibitor (Sigma-Aldrich), rComplete protease inhibitor (Roche)). The cells were incubated in lysis buffer for 18 h at 37 ˚C to allow for capsid self-assembly. The VLP solution was then supplemented with 850 mM NaCl and incubated for 30 min at 4°C. The solution was spun down for 10 min at 10,000 × g, resuspended in purification buffer (20 mM HEPES [pH 6.6], 150 mM NaCl, 1 mM CaCl2) and run through a density gradient ultracentrifugation round (15% sucrose–35% CsCl) for 1 h at 129,840 × g. Next, the DNA-filled VLPs were separated from the empty VLPs by a second round of density gradient centrifugation (4.4 M CsCl) for 18 h at 277,816 × g. The resulting VLP solutions were dialyzed overnight in purification buffer. Lastly, the VLPs were run through a cation exchange chromatography using a monolithic CIMacSO_3 column (BiaSep). VLP fractions eluted with a linear NaCl gradient (0.15 to 1 M NaCl, 20 mM HEPES, 1 mM $CaCl_2$ pH 6.6), were concentrated to 1 mg/ml and subsequently labeled by covalent linking to Alexa Fluor 647-NHS in 0.2 M NaHCO3 at pH 8.3 using a 10-fold molar excess of the dye relative to VP1 protein. Unbound dye was removed by two subsequent washing steps on pre-equilibrated Zeba columns (40 KDa cut-off, Thermo Scientific) in PBS buffer.

3. Polyoma VP1 purification procedure.

The truncated VP1 capsid proteins of either SV40, BKPyV, JCPyV or mPyV were expressed under a T7 promoter in *E.coli* BL21 strain in Lysogeny Broth medium supplemented with 500µM IPTG when Optical Density at 600 nm reached 0.8. After 24 h, the bacteria expressing the proteins were harvested and resuspended in lysis buffer (50 mM Tris pH 7.5, 5% Glycerol, 250 mM NaCl, 20 mM imidazole, 1 mg/ml lysozyme, 10 µg/ml DNAse I, protease and phosphatase inhibitor cocktail (Thermo Scientific)). The lysate was sonicated and cleared by centrifugation (7000 x g, 40 min, 4 ˚C). The supernatant was added to a pre-equilibrated Ni-NTA-bead gravity flow column, washed with washing buffer ((50 mM Tris pH 7.5, 5% Glycerol, 250 mM NaCl, 20 mM imidazole, protease and phosphatase inhibitor cocktail (Thermo Scientific)) and eluted with elution buffer (50 mM Tris pH 7.5, 5% Glycerol, 250 mM NaCl, 500 mM imidazole, protease and phosphatase inhibitor cocktail). The elution was then dialyzed overnight at 4 ˚C into protein buffer (50 mM Tris pH 7.5, 5% Glycerol, 150 mM NaCl). Next, a size-exclusion chromatography run on a Superdex 200 Increase 10/300 GL column was performed in protein buffer. The fractions containing the purified VP1 were pooled and concentrated to 1 mg/ml and stored at 4 ˚C). The VP1 proteins were labeled with Alexa Fluor 647-NHS in 0.2 M NaHCO3 at pH 8.3 using a 10-fold molar excess of the dye relative to VP1 protein. Unbound dye was removed by two subsequent washing steps on pre-equilibrated Zeba columns (7 KDa cut-off, Thermo Scientific) in PBS buffer.

Cell culture and transfections.

CV1 (ATCC CCL-70) and NRK49F (ATCC CRL-1570) cells were cultured in DMEM (Gibco) supplemented with 10% fetal bovine serum (Corning), 1 mM GlutaMax (Gibco). Cells were regularly tested for mycoplasma contamination.

Cells were transfected by electroporation using a Neon transfection system kit (Thermo Fischer) according to the manufacturer's specifications. In brief, cells were detached with Trypsin (Gibco) and washed one time in PBS before resuspension in R-buffer. Cells were then mixed with either 1 µg (single transfection) or 0.5 µg (double transfection) of each plasmid used and transfected in a 10 µl Neon pipette tip with two electric pulses at 1050 V for 30 ms. After transfection, cells were plated onto 12-well plates (for flow cytometry) or on 18-mm glass coverslips, thickness 1.5 (VWR, Cat. – No. 631-0153) (for microscopy) and grown for 24 h in medium at 37 ˚C before use.

For knock-down experiments, cells were transfected with PolyFect Transfection Reagent (Qiagen) according to the manufacturer's specifications. In brief, 10^5 cells were plated in 6-well plates one day prior to transfection. On transfection day, 4 µg of siRNA was diluted in OptiMEM and subsequently mixed with

PolyFect Transfection Reagent. After 20 min incubation at room temperature, the mixture was added to the cells and further incubated for 48 h before measurement.

For expression of MCPyV VLPs, HEK293TT cells were transfected with VP1- and VP2-coding plasmids using Polyethylenimin (PEI). In brief, the plasmids were mixed with PEI and Opti-MEM and incubated for 20 min at 37 ˚C. Next, the mixture was added to the cells and incubated for 24 h at 37 ˚C before washing and medium exchange. The cells were further allowed to express the protein for 3 days before harvest and purification.

Binding assays.

Cells were plated a day prior to experiments on 18-mm cover glass, thickness 1.5 (VWR, Cat. – No. 631-0153). For the EGFP/GEM-GFP binding assay, cells were transfected with the nanobody constructs a day prior to the binding assay, as described in the previous section. On the measurement day, cells were incubated at 4 ˚C for 20 min to stop endocytosis and further incubated with 2 µg/ml of either VLPs, recombinant EGFP or purified GEM-GFPs at 4 ˚C for 30 min. Then, the cells were fixed with 4% PFA, 0.2% GA in PBS at RT for 20 min. The cells were washed with PBS and the fixation solution was quenched in 50 mM NH_4Cl in PBS at RT for 30 min and imaged on a spinning disk confocal microscope.

Endocytosis assay and inhibitor treatments.

We quantified the GEM-GFP endocytosis amounts for all the different binding affinity nanobody-GPI constructs by performing quantitative endocytosis assays using flow cytometry measurements. In brief, cells were co-transfected with the nanobody constructs and a cytosolic mRFP-marker to select the positively transfected cells a day prior to the endocytosis assay, as described in the previous section. On the measurement day, the cells were washed with PBS and resuspended in fresh medium. For inhibitor endocytosis assays, cells were resuspended in either fresh medium supplemented with DMSO (control) or fresh medium supplemented with inhibitors as follows: 100 nM BafilomycinA, 25 µg/ml nystatin and 10 µg/ml progesterone followed by 1 h incubation and overnight incubation at 37 ˚C, respectively. Either 10 µg/ml Transferrin AF-488, 2 µg/ml GEM-GFP or 2 µg/ml VLPs were added to the cells in medium (endocytosis assay) or in medium supplemented with inhibitors (inhibitor assay) and further incubated for 1 h at 37 ˚C. Next, cells were washed 3x in acid buffer (0.5 M glycine in PBS, pH 2.2) to remove all surface-bound fraction of VLPs/GEMs and 1x in PBS before detaching with trypsin. Cells were resuspended in fresh medium and measured with a BD FACSCanto Flow Cytometry System. The gating strategy employed in the flow cytometry data analysis is explained in Supplementary Figure 5.

For Transferrin Receptor and Nanobody-GPI surface level quantification, cells were transfected as described in the previous section a day prior to the experiment. On the measurement day, the cells were washed with PBS and resuspended in serum-free medium and were incubated at 4 ˚C for 15 min before addition of either 10 µg/ml Transferrin AF-488 or 2 µg/ml purified EGFP and further incubation at 4 ˚C for 45 min. Cells were then washed x2 with cold PBS and were detached with accutase. Cells were resuspended in serum-free medium and measured with a BD FACSCanto Flow Cytometry System.

For GEM-GFP binding inhibition experiments, cells were transfected with the 0.036 nM binding affinity nanobody one day prior to experiment as described in the previous section. On the measurement day, 2 µg/ml GEM-GFP were pre-incubated with either 0 (ctrl), 4, 8 or 20 µg/ml of recombinant LaG16 nanobody for 5 min at RT. Then, the mix was added to the cells and they were imaged live on a spinning disk microscope.

Clathrin- or caveolin-colocalization assays.

CV1 cells were co-transfected with the specified GPI-nanobody construct and with either Clathrin-Light-Chain-mRFP or Caveolin1-mRFP as described in the previous section. For polyoma VLP colocalization, cells were transfected with either Clathrin-Light-Chain-mRFP or Caveolin1-mRFP as described in the previous section. Next day, cells were washed 2x with PBS and fresh medium supplemented with 10 mM HEPES was added. Next, 2 µg/ml of either GEM-GFP or polyoma VLPs were added to the cells and incubated for 10 min at 37 ˚C before imaging live on a TIRF (total internal reflection fluorescence) microscope.

Pulse-chase assay for intracellular traffic.

CV1 cells were transfected with either endosomal or lysosomal markers one day prior to the pulse chase experiments as described in the previous section. The next day, cells were washed with PBS, then resuspended in fresh medium and incubated at 4 °C for 20 min to stop endocytosis. Next, 2 µg/ml of either VLPs or GEM-GFP were added to the cells and incubated further for 30 min at 4 °C to allow for protein binding while endocytosis is inhibited. Then, cells were washed with PBS and resuspended in warm medium supplemented with 10 mM HEPES. Cells were either imaged live and right away corresponding to time point t=0 min or after incubation at 37 °C for the indicated times and fixed immediately with a 4% PFA solution in PBS for 20 min at 37 °C. In the case of live cell imaging, cells were placed at 37 °C and incubated for the respective amounts of time before imaging live on a spinning disk confocal microscope. In the case of fixed cell imaging, the samples were next quenched in 50 mM NH4Cl in PBS for 30 min at RT. Then, cells were permeabilized and blocked in buffer A (PBS supplemented with 1% BSA, 0.05% Saponin and 4% Horse serum for 45 min at RT while shaking. Next, each sample was place onto 50 µl of 1:1000 primary antibody diluted in buffer B (PBS supplemented with 1% BSA and 0.05% Saponin) and incubated overnight at 4 °C.

The next day, the samples were washed in buffer B and further incubated with 50 µl of 1:800 secondary antibody diluted in buffer B (PBS supplemented with 1% BSA and 0.05% Saponin) for 30 min at RT. Lastly, samples were washed in PBS and imaged on a confocal spinning disk microscope.

Cellular energy starvation assay.

Cellular energy was depleted by incubating CV1 cells in PBS^{++} supplemented with 10 mM 2-deoxy-D-glucose and 10 mM NaN_3 for 30 min at 37 °C until residual ATP levels dropped to 2.1% according to previous findings[243]. Next, cells were incubated with at least 30 µg/ml of the specified VLPs or 2 nM of GEM-GFP in energy-depletion medium for 1 h at 37 °C. In the last 10 min of incubation, 1 mg/ml of DiI C12 membrane dye was added to the cells for the remaining time. Cells were then imaged live in energy-depletion medium supplemented with 10 mM HEPES on a spinning disk confocal microscope.

Model membrane systems: Giant Unilamellar Vesicles.

GUVs were grown using the electroformation technique as previously described[244]. Lipid mixtures were prepared in a methanol:chloroform solvent to 1 mg/ml final concentration. Next, 5 ul of the mix were spread on each platinum wire of an in-house-built Pt electrode electroformation chamber. An electric current was applied and vesicles were grown in a 300 mM sucrose solution for 1 hour at 10 Hz and 2 V at room temperature. The alternating current was then decreased to 2 Hz and 2 V for another 30 min. Once the electroformation procedure was completed, the GUV suspension was dropped onto coverslips that have been pre-incubated with 1 mg/ml BSA solution and washed in PBS. GUVs were subsequently incubated with 10 µg/ml of the specified VLPs for 1 hour at room temperature in VLP buffer (10 mM HEPES at pH 6.8, 150 mM NaCl and 2 mM $CaCl_2$) and then imaged on a spinning disk confocal microscope.

Model membrane systems: Giant Plasma Membrane-derived Vesicles.

GPMVs were isolated from CV1 cells a by chemical vesiculant technique as previously described[245]. Briefly, CV1 cells close to confluency were washed with PBS and incubated with 4 µg/ml of DiI C12 membrane dye in PBS for 10 min at 37 °C. Cells were washed in PBS and resuspended in GPMV buffer (10 mM HEPES, 150 mM NaCl , 2 mM $CaCl_2$, pH 7.4) supplemented with 10 µM of the vesiculation agent calmidazolium. After 2 h incubation at 37°C, the supernatant was transferred to an Eppendorf tube and GPMVs were allowed to settle down for 30 min at RT. Finally, 200 µl of the GPMV solution was dropped onto a 8-well imaging chamber containing 200 µl of GPMV buffer. GPMVs were further incubated with 0.45 nM of GEM-GFP protein solution for 1 hour at RT and imaged on a spinning disk confocal microscope.

Western Blot

CV1 cells were transfected with the indicated GPI-anchored nanobody constructs and with Clathrin Heavy Chain siRNA as described in the previous section. After 48 hours, cells were detached with trypsin and resuspended in lysis buffer (0.1% Triton-X in PBS) and incubated at 4 °C for 20 min. Cell suspensions were spun down at 20.000 *g* for 40 min at 4 °C. The supernatant was collected, denatured and run on a SDS-PAGE 4–12% Bis-Tris gel (Eurogentec, ID-PA4121-010) in MOPS buffer. Blotting was performed by Trans-Blot Turbo (Bio-Rad) with 0.2 µm PVDF membranes (Bio-Rad, IB301002) accordingly to the manufacturer's protocol. Afterwards, the membrane was blocked in TBS supplemented with 5% BSA for 1 h at RT. Next, the membrane was incubated overnight at 4 °C with 1:1000 dilution of anti-CHC antibody (Cell Signaling Technology, P1663) in TBS-T. The next day, the membrane was washed three times in TBS-T and further incubated for 1 h at RT with 1:1000 dilution of secondary goat anti-rabbit HRP antibody (Invitrogen, 31462) in TBS-T. Lastly, the membrane was washed three times with TBS-T and imaged in ECL solution. Next, the membrane was stripped of antibodies in a mild stripping solution for 1 h at RT (200 mM Glycine, 1% SDS, 10% Tween-20 in dH_2O, pH 2.2) before the staining and imaging procedures were performed again with loading control anti-GAPDH antibodies (Abcam, ab8245).

Correlative light and electron microscopy.

Transfected cells expressing the Nanobody-GPI construct were grown on carbon-coated sapphire discs (3 mm diameter, 50 µm thickness, Wohlwend GmbH, art. 405). Next day, cells were treated with 5 µg/ml GEM-GFP at 4 ˚C for 20 min and then transferred to 37 ˚C for the indicated times. After treatment, the samples were high pressure frozen (HPM010, AbraFluid) in their growth medium and freeze substituted (EM-AFS2 , Leica Microsystems) with 0.1% uranyl acetate in dry acetone at -90 ˚C for 40 h. The temperature was then raised to -45 ˚C with a rate of 4.5 ˚C/h and the sample were further incubated for 5 h. After rinsing in acetone, the samples were infiltrated with increasing concentrations of Lowicryl HM20 resin (25%, 50%, 75%, 4 h /step and 3 x 10 h in 100%), while raising the temperature to -25 ˚C. Finally, the samples were UV-polymerized at -25 ˚C. The sapphire disc was then removed from the resin and 300 nm sections parallel to the block surface were cut and collected on carbon coated mesh grids (S160, Plano). Fluorescence imaging of the sections on the grids was carried out with a widefield fluorescence microscope (Olympus IX81) equipped with a 100x 1.40 NA Plan-Apochromat oil immersion objective. After post-staining with 2% uranyl acetate in 70% methanol and Reynold's lead citrate, tilt series of the areas of interest were acquired with TECNAI F30 transmission electron microscope (FEI) at 300 kV acceleration voltage using the software package SerialEM[246]. Tomograms were reconstructed using IMOD [247]. Correlation between fluorescence and electron microscopy images was performed with the plugin ec-CLEM [248] of the software platform Icy [249], using features of the sample that could be identified in both imaging modalities.

Platinum Replica Electron Microscopy (PREM)

NRK49F cells were transfected with the 0.036 nM binding affinity GPI-anchored nanobody plasmid using Lipfectamine 3000 (Thermo Fisher Scientific) according to the manufacturer's instructions. 24 h after transfection, the cells were detached with 1 mM EDTA in PBS, pelleted at 200g for 4 min, and resuspended in cellular medium containing 0.3 µg/ml GEMs. Cell suspension was incubated with GEMs for 5 min at 37°C and inverted every 1 min. 25 mm round coverslips (thickness no. 1.5) were coated with 0.01% (wt/vol) poly-L-Lysine solution (Sigma) for 20 min and cell-GEM suspension was then plated on the coverslips. Cells were attached to the coverslips by centrifugation at 100 g for 1 min. After attachment cells were incubated at 37°C for 10 min prior to unroofing and fixation.

Cells were unroofed to obtain plasma membrane sheets as described previously[250,251]. Briefly, cells on coverslips were placed in stabilization buffer (70 mM KCl, 30 mM HEPES, 5 mM MgCl2, 3 mM EGTA, at pH 7.4 with KOH) and unroofing was performed with a squirt of 2% PFA in stabilization buffer (EM grade, freshly prepared, Electron Microscopy Science #15710) on the cells using a 21-gauge needle and syringe. Afterwards, the unroofed cells were placed in fresh 4% PFA for 15 min at 21°C and then used for immunostaining.

Immunostaining of PREM samples

After fixation the coverslips were washed in stabilization buffer once and fixation was quenched with 50 mM NH4Cl in stabilization buffer for 7 min and washed two more times. Cells were blocked for 1 h with 4% (v/v) horse serum and 1% (w/v) bovine serum albumin (BSA) in stabilization buffer. The samples were then incubated with anti-clathrin heavy chain (P1663) antibody (1:100, #2410, Cell Signaling Technology) and 1% BSA in stabilization buffer at 21°C for 1 h followed by 4 washing steps with 1% BSA in stabilization buffer. Next, cells were incubated with goat anti-rabbit IgG Alexa Fluor 568 (1:500, #A-11011, Invitrogen) and CellMask Deep Red Plasma Membrane Stain (1:5000, # C10046, Invitrogen) with 1% BSA in stabilization buffer for 45 min. Samples were rinsed 4 times with stabilization buffer, postfixed in 4% (w/v) paraformaldehyde in stabilization buffer for 10 min and quenched as described above prior to imaging by spinning disc confocal microscopy.

Platinum replica preparation

After spinning disc confocal microscopy, the plasma membrane sheets were fixed in 2% glutaraldehyde in stabilization buffer for at least 30 min and EM samples were prepared as described previously[250,251]. Samples were rinsed 3 times with water and stained with 0.1% (w/v) tannic acid for 20 min followed by staining with 0.1% (w/v) uranyl acetate for 20 min. The coverslips were then dehydrated through a series of increasing

ethanol concentration to 100% ethanol followed by critical point drying (Leica EM CPD300). The coverslips were then low angle rotary shadowed with 1.4 nm platinum and 5 nm carbon in a dual ion beam evaporator (Leica EM ACE600).

Electron microscopy

Platinum and carbon coated coverslips were mounted with double sided carbon disks and imaged at a Helios 5CX scanning electron microscope. Low resolution scans for navigation were done with ETD or ICE detectors using MAPS software. Alignment of fluorescence microscopic overview images with SEM tile sets to navigate to cells of interest was done with MAPS as well. Ultrahigh resolution scanning of unroofed cells was done with TLD detector in secondary electron mode at 3.7 mm working distance, 5 kV, 21 pA, 1 µs dwell time, line integration mode (8 cycles) and 0.67 nm pixel size. Tile sets were stitched with the Grid/Collection stitching plugin in ImageJ. Images were 2x2 binned.

Correlative Light Electron Microscopy for the PREM samples

Correlation of fluorescence microscopic and SEM images was achieved by taking overview images of the CellMask signal using 10x magnification for navigation and by marking the region on the coverslip used for fluorescence microscopic imaging with a diamond pen. After SEM imaging the fluorescence microscopic images were aligned to the ultrahigh resolution SEM images. Coarse alignment was done based on the CellMask staining and the cell borders, exact alignment was done based on the clathrin staining using the BigWarp plugin in ImageJ.

Spinning disc confocal microscopy

Fluorescence images were acquired on an inverted IX71 microscope (Olympus) equipped with a CSU-X1 spinning disk unit (Yokogawa) and an iLas laser illumination system (Gataca Systems) with 491 nm, 561 nm and 639 nm lasers for illumination. 10x NA 0.3 air or 60x NA 1.42 oil objectives (Olympus) were used, and images were captured with an ORCA Flash 4.0LT sCMOS camera (Hamamatsu). The system was operated using the software MetaMorph.

Total internal fluorescence microscopy.

A custom build TIRF microscope was used to perform the colocalization assays between CLC-dsRED/Caveolin1-mRFP and GEM-GFPs. In brief, a 473 nm laser (Laserglow Technologies) and 561 nm laser (Laserglow Technologies) were focused onto the back-focal plane of a TIRF objective (NA, 1.49; 60×; Olympus) for highly inclined plane illumination. A quad-edge dichroic beamsplitter (405/488/561/635 nm; Semrock) separated fluorescence emission from the excitation light. Emission light was filtered by a quad-band bandpass filter (446/523/600/677 nm; Semrock) and focused by a 500-mm tube lens onto the chip of a

back-illuminated electron-multiplying charge-coupled device camera (Evolve; Photometrics) that was water-cooled to −85°C.

Image analysis and quantification of colocalization.

Image analysis and fluorescence intensity quantification were performed with ImageJ [252]. The percentage of colocalization between the two channels (Organelle and Virus/GEM) imaged was quantitatively determined on a per-object basis using a custom-made pipeline in CellProfiler[253]. In brief, the Z-stacks acquired for each channel were first split into individual images that were then segmented into objects identifying either the VLPs/GEMs or the specific organelles inside cells. The percentage of colocalization was then calculated as the amount of overlapping pixels between the identified objects in the two channels divided by the total pixel area occupied by the Virus/GEM channel.

Schematics, drawings and illustrative representation of proteins.

All schematics were realized in Adobe Illustrator, unless otherwise specified. All illustrative representations of proteins, VLPs or toxin mimics were realized with PyMol from the indicated PDB structures.

Calculation of energy gain for joint particle wrapping in tubules.

We numerically determined the energy gain for the joint wrapping of GEM-GFP particles in tubules by minimizing the sum of bending and adhesion energies for the rotationally symmetric shapes of the membrane tubules and for membrane segments wrapping single particles as previously described[254]. For the energy minimization, the profiles of the rationally symmetric membranes around the particles are discretized into up to about 400 segments in the parametrizations as previously described[254]. To avoid membrane overlap in nearly closed membrane necks obtained for large values of the adhesion potential depth U (small values of K_D), the distance of membrane midplanes in these necks is constrained to be larger than 5 nm. The minimum-energy shapes were determined via constrained minimization with the FindMinimum function of the program Mathematica 13 [Wolfram Research, Inc., Mathematica, Version 13.2, Champaign, IL (2022)].

References

1. Singer, S. J. & Nicolson, G. L. The Fluid Mosaic Model of the Structure of Cell Membranes. *Science* **175**, 720–731 (1972).
2. Sezgin, E., Levental, I., Mayor, S. & Eggeling, C. The mystery of membrane organization: composition, regulation and roles of lipid rafts. *Nat Rev Mol Cell Biol* **18**, 361–374 (2017).
3. The Cell - Hardcover - Geoffrey Cooper - Oxford University Press. https://global.oup.com/ushe/product/the-cell-9781605357072.
4. Fiore, P. P. D. & Zastrow, M. von. Endocytosis, Signaling, and Beyond. *Cold Spring Harb Perspect Biol* **6**, a016865 (2014).
5. Antonescu, C. N., McGraw, T. E. & Klip, A. Reciprocal Regulation of Endocytosis and Metabolism. *Cold Spring Harb Perspect Biol* **6**, a016964 (2014).
6. Tauber, A. I. Metchnikoff and the phagocytosis theory. *Nat Rev Mol Cell Biol* **4**, 897–901 (2003).
7. Holter, H. Pinocytosis. in *International Review of Cytology* (eds. Bourne, G. H. & Danielli, J. F.) vol. 8 481–504 (Academic Press, 1959).
8. E, P. G. Fine structure of blood capillaries. *J Appl Physics* **24**, 1424–1448 (1953).
9. Yamada, E. The fine structure of the gall bladder epithelium of the mouse. *J Biophys Biochem Cytol* **1**, 445–458 (1955).
10. Roth, T. F. & Porter, K. R. Yolk protein uptake in the oocyte of the mosquito aedes aegypti. L. *Journal of Cell Biology* **20**, 313–332 (1964).
11. Pearse, B. M. F. Coated vesicles from pig brain: Purification and biochemical characterization. *Journal of Molecular Biology* **97**, 93–98 (1975).
12. Montesano, R., Roth, J., Robert, A. & Orci, L. Non-coated membrane invaginations are involved in binding and internalization of cholera and tetanus toxins. *Nature* **296**, 651–653 (1982).
13. Claude, A. Fractionation of mammalian liver cells by differential centrifugation. *J Exp Med* **84**, 51–59 (1946).
14. Pearse, B. M. Clathrin: a unique protein associated with intracellular transfer of membrane by coated vesicles. *Proceedings of the National Academy of Sciences* **73**, 1255–1259 (1976).
15. Kaksonen, M. & Roux, A. Mechanisms of clathrin-mediated endocytosis. *Nat Rev Mol Cell Biol* **19**, 313–326 (2018).
16. Moya, M., Dautry-Varsat, A., Goud, B., Louvard, D. & Boquet, P. Inhibition of coated pit formation in Hep2 cells blocks the cytotoxicity of diphtheria toxin but not that of ricin toxin. *Journal of Cell Biology* **101**, 548–559 (1985).
17. Sandvig, K., Olsnes, S., Petersen, O. W. & van Deurs, B. Acidification of the cytosol inhibits endocytosis from coated pits. *Journal of Cell Biology* **105**, 679–689 (1987).

18. Damke, H., Baba, T., van der Bliek, A. M. & Schmid, S. L. Clathrin-independent pinocytosis is induced in cells overexpressing a temperature-sensitive mutant of dynamin. *Journal of Cell Biology* **131**, 69–80 (1995).
19. Rennick, J. J., Johnston, A. P. R. & Parton, R. G. Key principles and methods for studying the endocytosis of biological and nanoparticle therapeutics. *Nat. Nanotechnol.* **16**, 266–276 (2021).
20. McMahon, H. T. & Boucrot, E. Molecular mechanism and physiological functions of clathrin-mediated endocytosis. *Nat Rev Mol Cell Biol* **12**, 517–533 (2011).
21. Mayor, S., Parton, R. G. & Donaldson, J. G. Clathrin-Independent Pathways of Endocytosis. *Cold Spring Harb Perspect Biol* **6**, a016758 (2014).
22. Ewers, H. & Helenius, A. Lipid-mediated endocytosis. *Cold Spring Harbor Perspectives in Biology* **3**, 1–14 (2011).
23. Bitsikas, V., Corrêa, I. R. & Nichols, B. J. Clathrin-independent pathways do not contribute significantly to endocytic flux. *eLife* **2014**, 1–26 (2014).
24. Weinberg, J. & Drubin, D. G. Clathrin-mediated endocytosis in budding yeast. *Trends Cell Biol* **22**, 1–13 (2012).
25. Henne, W. M. *et al.* FCHo Proteins Are Nucleators of Clathrin-Mediated Endocytosis. *Science* **328**, 1281–1284 (2010).
26. Stimpson, H. E. M., Toret, C. P., Cheng, A. T., Pauly, B. S. & Drubin, D. G. Early-Arriving Syp1p and Ede1p Function in Endocytic Site Placement and Formation in Budding Yeast. *MBoC* **20**, 4640–4651 (2009).
27. Kelly, B. T. *et al.* AP2 controls clathrin polymerization with a membrane-activated switch. *Science* **345**, 459–463 (2014).
28. Höning, S. *et al.* Phosphatidylinositol-(4,5)-Bisphosphate Regulates Sorting Signal Recognition by the Clathrin-Associated Adaptor Complex AP2. *Molecular Cell* **18**, 519–531 (2005).
29. Kelly, B. T. *et al.* A structural explanation for the binding of endocytic dileucine motifs by the AP2 complex. *Nature* **456**, 976–979 (2008).
30. Ohno, H. *et al.* Interaction of Tyrosine-Based Sorting Signals with Clathrin-Associated Proteins. *Science* **269**, 1872–1875 (1995).
31. Ford, M. G. J. *et al.* Curvature of clathrin-coated pits driven by epsin. *Nature* **419**, 361–366 (2002).
32. Kirchhausen, T. & Harrison, S. C. Protein organization in clathrin trimers. *Cell* **23**, 755–761 (1981).
33. Saleem, M. *et al.* A balance between membrane elasticity and polymerization energy sets the shape of spherical clathrin coats. *Nat Commun* **6**, 6249 (2015).
34. Heuser, J. Three-dimensional visualization of coated vesicle formation in fibroblasts. *Journal of Cell Biology* **84**, 560–583 (1980).

35. Kozlov, M. M. & Taraska, J. W. Generation of nanoscopic membrane curvature for membrane trafficking. *Nat Rev Mol Cell Biol* **24**, 63–78 (2023).
36. Sochacki, K. A. *et al.* The structure and spontaneous curvature of clathrin lattices at the plasma membrane. *Developmental Cell* **56**, 1131-1146.e3 (2021).
37. Cocucci, E., Aguet, F., Boulant, S. & Kirchhausen, T. The First Five Seconds in the Life of a Clathrin-Coated Pit. *Cell* **150**, 495–507 (2012).
38. Day, K. J. *et al.* Liquid-like protein interactions catalyse assembly of endocytic vesicles. *Nat Cell Biol* **23**, 366–376 (2021).
39. Kozak, M. & Kaksonen, M. Phase separation of Ede1 promotes the initiation of endocytic event. Preprint at https://doi.org/10.1101/861203 (2019).
40. Merrifield, C. J., Feldman, M. E., Wan, L. & Almers, W. Imaging actin and dynamin recruitment during invagination of single clathrin-coated pits. *Nat Cell Biol* **4**, 691–698 (2002).
41. Merrifield, C. J., Perrais, D. & Zenisek, D. Coupling between Clathrin-Coated-Pit Invagination, Cortactin Recruitment, and Membrane Scission Observed in Live Cells. *Cell* **121**, 593–606 (2005).
42. Mund, M. *et al.* Systematic Nanoscale Analysis of Endocytosis Links Efficient Vesicle Formation to Patterned Actin Nucleation. *Cell* **174**, 884-896.e17 (2018).
43. Cheng, J., Grassart, A. & Drubin, D. G. Myosin 1E coordinates actin assembly and cargo trafficking during clathrin-mediated endocytosis. *MBoC* **23**, 2891–2904 (2012).
44. Manenschijn, H. E. *et al.* Type-I myosins promote actin polymerization to drive membrane bending in endocytosis. *eLife* **8**, e44215 (2019).
45. Hinshaw, J. E. & Schmid, S. L. Dynamin self-assembles into rings suggesting a mechanism for coated vesicle budding. *Nature* **374**, 190–192 (1995).
46. Sweitzer, S. M. & Hinshaw, J. E. Dynamin Undergoes a GTP-Dependent Conformational Change Causing Vesiculation. *Cell* **93**, 1021–1029 (1998).
47. Sundborger, A. *et al.* An endophilin–dynamin complex promotes budding of clathrin-coated vesicles during synaptic vesicle recycling. *Journal of Cell Science* **124**, 133–143 (2011).
48. Ferguson, S. *et al.* Coordinated Actions of Actin and BAR Proteins Upstream of Dynamin at Endocytic Clathrin-Coated Pits. *Developmental Cell* **17**, 811–822 (2009).
49. Almeida-Souza, L. *et al.* A Flat BAR Protein Promotes Actin Polymerization at the Base of Clathrin-Coated Pits. *Cell* **174**, 325-337.e14 (2018).
50. Mayle, K. M., Le, A. M. & Kamei, D. T. The intracellular trafficking pathway of transferrin. *Biochimica et Biophysica Acta - General Subjects* **1820**, 264–281 (2012).
51. Jung, N. & Haucke, V. Clathrin-Mediated Endocytosis at Synapses. *Traffic* **8**, 1129–1136 (2007).

52. Thorn, H. *et al.* Cell Surface Orifices of Caveolae and Localization of Caveolin to the Necks of Caveolae in Adipocytes. *MBoC* **14**, 3967–3976 (2003).
53. Parton, R. G. Caveolae: Structure, Function, and Relationship to Disease. *Annual Review of Cell and Developmental Biology* **34**, 111–136 (2018).
54. Matthaeus, C. *et al.* The molecular organization of differentially curved caveolae indicates bendable structural units at the plasma membrane. *Nat Commun* **13**, 7234 (2022).
55. Han, B., Copeland, C. A., Tiwari, A. & Kenworthy, A. K. Assembly and Turnover of Caveolae: What Do We Really Know? *Front Cell Dev Biol* **4**, 68 (2016).
56. Porta, J. C. *et al.* Molecular architecture of the human caveolin-1 complex. *Science Advances* **8**, eabn7232 (2022).
57. Tillu, V. A. *et al.* Cavin1 intrinsically disordered domains are essential for fuzzy electrostatic interactions and caveola formation. *Nat Commun* **12**, 931 (2021).
58. Kovtun, O., Tillu, V. A., Ariotti, N., Parton, R. G. & Collins, B. M. Cavin family proteins and the assembly of caveolae. *J Cell Sci* **128**, 1269–1278 (2015).
59. Parton, R. G., Tillu, V., McMahon, K.-A. & Collins, B. M. Key phases in the formation of caveolae. *Current Opinion in Cell Biology* **71**, 7–14 (2021).
60. Oh, P., McIntosh, D. P. & Schnitzer, J. E. Dynamin at the Neck of Caveolae Mediates Their Budding to Form Transport Vesicles by GTP-driven Fission from the Plasma Membrane of Endothelium. *Journal of Cell Biology* **141**, 101–114 (1998).
61. Henley, J. R., Krueger, E. W. A., Oswald, B. J. & McNiven, M. A. Dynamin-mediated Internalization of Caveolae. *J Cell Biol* **141**, 85–99 (1998).
62. Stoeber, M. *et al.* Oligomers of the ATPase EHD2 confine caveolae to the plasma membrane through association with actin. *The EMBO Journal* **31**, 2350–2364 (2012).
63. Pelkmans, L., Bü, T., Zerial, M. & Helenius, A. Caveolin-Stabilized Membrane Domains as Multifunctional Transport and Sorting Devices in Endocytic Membrane Traffic Other Rab GTPases of early and recycling endosomes are segregated into distinct membrane domains that display different biochemical composition. *Cell* vol. 118 767–780 (2004).
64. Shvets, E., Bitsikas, V., Howard, G., Hansen, C. G. & Nichols, B. J. Dynamic caveolae exclude bulk membrane proteins and are required for sorting of excess glycosphingolipids. *Nat Commun* **6**, 6867 (2015).
65. Parton, R. G. & del Pozo, M. A. Caveolae as plasma membrane sensors, protectors and organizers. *Nat Rev Mol Cell Biol* **14**, 98–112 (2013).
66. Zhou, Y. *et al.* Caveolin-1 and cavin1 act synergistically to generate a unique lipid environment in caveolae. *Journal of Cell Biology* **220**, e202005138 (2021).

67. Murata, M. *et al.* VIP21/caveolin is a cholesterol-binding protein. *Proceedings of the National Academy of Sciences* **92**, 10339–10343 (1995).
68. Matthaeus, C. & Taraska, J. W. Energy and Dynamics of Caveolae Trafficking. *Frontiers in Cell and Developmental Biology* **8**, (2021).
69. Pelkmans, L. & Helenius, A. Endocytosis via caveolae. *Traffic* **3**, 311–320 (2002).
70. Pelkmans, L., Kartenbeck, J. & Helenius, A. Caveolar endocytosis of simian virus 40 reveals a new two-step vesicular-transport pathway to the ER. *Nature Cell Biology* **3**, 473–483 (2001).
71. Damm, E. M. *et al.* Clathrin- and caveolin-1-independent endocytosis: Entry of simian virus 40 into cells devoid of caveolae. *Journal of Cell Biology* **168**, 477–488 (2005).
72. Kirkham, M. *et al.* Ultrastructural identification of uncoated caveolin-independent early endocytic vehicles. *Journal of Cell Biology* **168**, 465–476 (2005).
73. Hanson, C. A. *et al.* Overexpression of Caveolin-1 Is Sufficient to Phenocopy the Behavior of a Disease-Associated Mutant. *Traffic* **14**, 663–677 (2013).
74. Helfrich, W. Elastic Properties of Lipid Bilayers: Theory and Possible Experiments. *Zeitschrift für Naturforschung C* **28**, 693–703 (1973).
75. Marsh, D. Elastic curvature constants of lipid monolayers and bilayers. *Chemistry and Physics of Lipids* **144**, 146–159 (2006).
76. Roux, A. *et al.* Role of curvature and phase transition in lipid sorting and fission of membrane tubules. *EMBO J* **24**, 1537–1545 (2005).
77. Baumgart, T., Hess, S. T. & Webb, W. W. Imaging coexisting fluid domains in biomembrane models coupling curvature and line tension. *Nature* **425**, 821–824 (2003).
78. Johannes, L., Wunder, C. & Bassereau, P. Bending 'on the rocks'-A cocktail of biophysical modules to build endocytic pathways. *Cold Spring Harbor Perspectives in Biology* **6**, (2014).
79. Pontes, B., Monzo, P. & Gauthier, N. C. Membrane tension: A challenging but universal physical parameter in cell biology. *Seminars in Cell & Developmental Biology* **71**, 30–41 (2017).
80. McMahon, H. T. & Boucrot, E. Membrane curvature at a glance. *Journal of Cell Science* **128**, 1065–1070 (2015).
81. Stachowiak, J. C., Hayden, C. C. & Sasaki, D. Y. Steric confinement of proteins on lipid membranes can drive curvature and tubulation. *Proceedings of the National Academy of Sciences* **107**, 7781–7786 (2010).
82. Stachowiak, J. C. *et al.* Membrane bending by protein-protein crowding. *Nature Cell Biology* **14**, 944–949 (2012).

83. A. T. Hammond, F. A. Heberle, T. Baumgart, D. Holowka, B. Baird, and G. W. F. Crosslinking a lipid raft component triggers liquid ordered–liquid disordered phase separation in model plasma membranes. *Proceedings of the National Academy of Sciences* **98**, 9471–9473 (2002).
84. Römer, W. *et al.* Shiga toxin induces tubular membrane invaginations for its uptake into cells. *Nature* **450**, 670–675 (2007).
85. Ewers, H. *et al.* GM1 structure determines SV40-induced membrane invagination and infection. *Nature Cell Biology* **12**, 11–18 (2010).
86. Boucrot, E. *et al.* Endophilin marks and controls a clathrin-independent endocytic pathway. *Nature* **517**, 460–465 (2015).
87. Renard, H. F. *et al.* Endophilin-A2 functions in membrane scission in clathrin-independent endocytosis. *Nature* **517**, 493–496 (2015).
88. Römer, W. *et al.* Actin Dynamics Drive Membrane Reorganization and Scission in Clathrin-Independent Endocytosis. *Cell* **140**, 540–553 (2010).
89. Pelkmans, L., Püntener, D. & Helenius, A. Local actin polymerization and dynamin recruitment in SV40-induced internalization of caveolae. *Science* **296**, 535–539 (2002).
90. Sathe, M. *et al.* Small GTPases and BAR domain proteins regulate branched actin polymerisation for clathrin and dynamin-independent endocytosis. *Nat Commun* **9**, 1835 (2018).
91. Day, C. A. *et al.* Microtubule Motors Power Plasma Membrane Tubulation in Clathrin-Independent Endocytosis. *Traffic* **16**, 572–590 (2015).
92. Zila, V., Difato, F., Klimova, L., Huerfano, S. & Forstova, J. Involvement of Microtubular Network and Its Motors in Productive Endocytic Trafficking of Mouse Polyomavirus. *PLoS ONE* **9**, e96922 (2014).
93. Sabharanjak, S., Sharma, P., Parton, R. G. & Mayor, S. GPI-anchored proteins are delivered to recycling endosomes via a distinct cdc42-regulated clathrin-independent pinocytic pathway. *Developmental Cell* **2**, 411–423 (2002).
94. Johannes, L., Wunder, C. & Shafaq-Zadah, M. Glycolipids and Lectins in Endocytic Uptake Processes. *Journal of Molecular Biology* **428**, 4792–4818 (2016).
95. Shafaq-Zadah, M., Dransart, E. & Johannes, L. Clathrin-independent endocytosis, retrograde trafficking, and cell polarity. *Current Opinion in Cell Biology* **65**, 112–121 (2020).
96. Abrami, L., Liu, S., Cosson, P., Leppla, S. H. & van der Goot, F. G. Anthrax toxin triggers endocytosis of its receptor via a lipid raft–mediated clathrin-dependent process. *Journal of Cell Biology* **160**, 321–328 (2003).
97. Boll, W., Ehrlich, M., Collier, R. J. & Kirchhausen, T. Effects of dynamin inactivation on pathways of anthrax toxin uptake. *European Journal of Cell Biology* **83**, 281–288 (2004).

98. Morris, R. E., Gerstein, A. S., Bonventre, P. F. & Saelinger, C. B. Receptor-mediated entry of diphtheria toxin into monkey kidney (Vero) cells: electron microscopic evaluation. *Infection and Immunity* **50**, 721–727 (1985).
99. Skretting, G., Torgersen, M. L., van Deurs, B. & Sandvig, K. Endocytic mechanisms responsible for uptake of GPI-linked diphtheria toxin receptor. *Journal of Cell Science* **112**, 3899–3909 (1999).
100. Pellett, S., Tepp, W. H., Scherf, J. M. & Johnson, E. A. Botulinum Neurotoxins Can Enter Cultured Neurons Independent of Synaptic Vesicle Recycling. *PLOS ONE* **10**, e0133737 (2015).
101. Deinhardt, K., Berninghausen, O., Willison, H. J., Hopkins, C. R. & Schiavo, G. Tetanus toxin is internalized by a sequential clathrin-dependent mechanism initiated within lipid microdomains and independent of epsin1. *Journal of Cell Biology* **174**, 459–471 (2006).
102. Sandvig, K. *et al.* Ricin transport into cells: studies of endocytosis and intracellular transport. *International Journal of Medical Microbiology* **290**, 415–420 (2000).
103. Sandvig, K., Olsnes, S., Brown, J. E., Petersen, O. W. & Van Deurs, B. Endocytosis from coated pits of Shiga toxin: A glycolipid-binding protein from Shigella dysenteriae 1. *Journal of Cell Biology* **108**, 1331–1343 (1989).
104. Torgersen, M. L., Skretting, G., van Deurs, B. & Sandvig, K. Internalization of cholera toxin by different endocytic mechanisms. *Journal of Cell Science* **114**, 3737–3747 (2001).
105. Wernick, N. L. B., Chinnapen, D. J.-F., Cho, J. A. & Lencer, W. I. Cholera Toxin: An Intracellular Journey into the Cytosol by Way of the Endoplasmic Reticulum. *Toxins (Basel)* **2**, 310–325 (2010).
106. Liebl, D. *et al.* Mouse Polyomavirus Enters Early Endosomes, Requires Their Acidic pH for Productive Infection, and Meets Transferrin Cargo in Rab11-Positive Endosomes. *Journal of Virology* **80**, 4610–4622 (2006).
107. Querbes, W., O'Hara, B. A., Williams, G. & Atwood, W. J. Invasion of Host Cells by JC Virus Identifies a Novel Role for Caveolae in Endosomal Sorting of Noncaveolar Ligands. *Journal of Virology* **80**, 9402–9413 (2006).
108. Zhao, L., Marciano, A. T., Rivet, C. R. & Imperiale, M. J. Caveolin- and clathrin-independent entry of BKPyV into primary human proximal tubule epithelial cells. *Virology* **492**, 66–72 (2016).
109. Eash, S., Querbes, W. & Atwood, W. J. Infection of Vero Cells by BK Virus Is Dependent on Caveolae. *Journal of Virology* **78**, 11583–11590 (2004).
110. Becker, M. *et al.* Infectious Entry of Merkel Cell Polyomavirus. *Journal of Virology* **93**, JVI.02004-18 (2019).
111. Nguyen, L. *et al.* Sialic acid-containing glycolipids mediate binding and viral entry of SARS-CoV-2. *Nat Chem Biol* **18**, 81–90 (2022).

112. Negi, G. *et al.* SARS-CoV-2 Binding to Terminal Sialic Acid of Gangliosides Embedded in Lipid Membranes. *ACS Infect. Dis.* (2023) doi:10.1021/acsinfecdis.3c00106.

113. Ayyar, B. V. *et al.* CLIC and membrane wound repair pathways enable pandemic norovirus entry and infection. *Nat Commun* **14**, 1148 (2023).

114. Neu, U. *et al.* A Structure-Guided Mutation in the Major Capsid Protein Retargets BK Polyomavirus. *PLoS Pathogens* **9**, e1003688 (2013).

115. Neu, U., Woellner, K., Gauglitz, G. & Stehle, T. Structural basis of GM1 ganglioside recognition by simian virus 40. *Proceedings of the National Academy of Sciences of the United States of America* **105**, 5219–5224 (2008).

116. Campanero-Rhodes, M. A. *et al.* N-Glycolyl GM1 Ganglioside as a Receptor for Simian Virus 40. *Journal of Virology* **81**, 12846–12858 (2007).

117. Ewers, H. *et al.* Single-particle tracking of murine polyoma virus-like particles on live cells and artificial membranes. *Proceedings of the National Academy of Sciences* **102**, 15110–15115 (2005).

118. Szklarczyk, O. M. *et al.* Receptor Concentration and Diffusivity Control Multivalent Binding of Sv40 to Membrane Bilayers. *PLoS Computational Biology* **9**, (2013).

119. Ali, M., Nelson, A. R., Lopez, A. L. & Sack, D. A. Updated Global Burden of Cholera in Endemic Countries. *PLoS Negl Trop Dis* **9**, e0003832 (2015).

120. Kuziemko, G. M., Stroh, M. & Stevens, R. C. Cholera toxin binding affinity and specificity for gangliosides determined by surface plasmon resonance. *Biochemistry* **35**, 6375–6384 (1996).

121. Bacia, K., Schwille, P. & Kurzchalia, T. Sterol structure determines the separation of phases and the curvature of the liquid-ordered phase in model membranes. *PNAS* **102**, (2005).

122. Lingwood, D., Ries, J., Schwille, P. & Simons, K. Plasma membranes are poised for activation of raft phase coalescence at physiological temperature. *Proceedings of the National Academy of Sciences of the United States of America* **105**, 10005–10010 (2008).

123. Kabbani, A. M., Raghunathan, K., Lencer, W. I., Kenworthy, A. K. & Kelly, C. V. Structured clustering of the glycosphingolipid GM1 is required for membrane curvature induced by cholera toxin. *Proceedings of the National Academy of Sciences* **117**, 14978–14986 (2020).

124. Raghunathan, K. *et al.* Glycolipid Crosslinking Is Required for Cholera Toxin to Partition Into and Stabilize Ordered Domains. *Biophysical Journal* **111**, 2547–2550 (2016).

125. Wolf, A. A. *et al.* Attenuated endocytosis and toxicity of a mutant cholera toxin with decreased ability to cluster ganglioside GM1 molecules. *Infection and Immunity* **76**, 1476–1484 (2008).

126. Cervin, J. *et al.* GM1 ganglioside-independent intoxication by Cholera toxin. *PLoS pathogens* **14**, e1006862 (2018).

127. Heim, J. B., Hodnik, V., Heggelund, J. E., Anderluh, G. & Krengel, U. Crystal structures of cholera toxin in complex with fucosylated receptors point to importance of secondary binding site. *Sci Rep* **9**, 12243 (2019).

128. Wands, A. M. *et al.* Fucosylation and protein glycosylation create functional receptors for cholera toxin. *eLife* **4**, e09545 (2015).

129. Fuchs, G. *et al.* Pathogenesis of Shigella diarrhea: rabbit intestinal cell microvillus membrane binding site for Shigella toxin. *Infection and Immunity* **53**, 372–377 (1986).

130. Watkins, E. B. *et al.* Shiga Toxin Induces Lipid Compression: A Mechanism for Generating Membrane Curvature. *Nano Lett.* **19**, 7365–7369 (2019).

131. Pezeshkian, W. *et al.* Mechanism of Shiga Toxin Clustering on Membranes. *ACS Nano* **11**, 314–324 (2017).

132. Lakadamyali, M., Rust, M. J. & Zhuang, X. Ligands for Clathrin-Mediated Endocytosis Are Differentially Sorted into Distinct Populations of Early Endosomes. *Cell* **124**, 997–1009 (2006).

133. Lencer, W. I. & Tsai, B. The intracellular voyage of cholera toxin: going retro. *Trends in Biochemical Sciences* **28**, 639–645 (2003).

134. Mallard, F. *et al.* Direct Pathway from Early/Recycling Endosomes to the Golgi Apparatus Revealed through the Study of Shiga Toxin B-fragment Transport. *Journal of Cell Biology* **143**, 973–990 (1998).

135. Engel, S. *et al.* Role of Endosomes in Simian Virus 40 Entry and Infection. *Journal of Virology* **85**, 4198–4211 (2011).

136. Dangoria, N. S., Breau, W. C., Anderson, H. A., Cishek, D. M. & Norkin, L. C. Extracellular simian virus 40 induces an ERK/MAP kinase-independent signalling pathway that activates primary response genes and promotes virus entry. *Journal of General Virology* **77**, 2173–2182 (1996).

137. Motamedi, N., Sewald, X., Luo, Y., Mothes, W. & DiMaio, D. SV40 Polyomavirus Activates the Ras-MAPK Signaling Pathway for Vacuolization, Cell Death, and Virus Release. *Viruses* **12**, 1128 (2020).

138. Bonifacino, J. S. & Hurley, J. H. Retromer. *Current Opinion in Cell Biology* **20**, 427–436 (2008).

139. Singh, V. *et al.* Cholera toxin inhibits SNX27-retromer-mediated delivery of cargo proteins to the plasma membrane. *Journal of Cell Science* **131**, jcs218610 (2018).

140. Johannes, L. Shiga toxin—a model for glycolipid-dependent and lectin-driven endocytosis. *Toxins* **9**, (2017).

141. Falguières, T. *et al.* Targeting of Shiga toxin B-subunit to retrograde transport route in association with detergent-resistant membranes. *Molecular Biology of the Cell* **12**, 2453–2468 (2001).

142. Chinnapen, D. J. F. *et al.* Lipid Sorting by Ceramide Structure from Plasma Membrane to ER for the Cholera Toxin Receptor Ganglioside GM1. *Developmental Cell* **23**, 573–586 (2012).

143. Akita, F. *et al.* The Crystal Structure of a Virus-like Particle from the Hyperthermophilic Archaeon Pyrococcus furiosus Provides Insight into the Evolution of Viruses. *Journal of Molecular Biology* **368**, 1469–1483 (2007).

144. Delarue, M. *et al.* mTORC1 Controls Phase Separation and the Biophysical Properties of the Cytoplasm by Tuning Crowding. *Cell* **174**, 338-349.e20 (2018).

145. Fridy, P. C. *et al.* A robust pipeline for rapid production of versatile nanobody repertoires. *Nat Methods* **11**, 1253–1260 (2014).

146. Xu, G.-K., Hu, J., Lipowsky, R. & Weikl, T. R. Binding constants of membrane-anchored receptors and ligands: A general theory corroborated by Monte Carlo simulations. *J. Chem. Phys.* **143**, 243136 (2015).

147. Steinkühler, J., Sezgin, E., Urbančič, I., Eggeling, C. & Dimova, R. Mechanical properties of plasma membrane vesicles correlate with lipid order, viscosity and cell density. *Commun Biol* **2**, 1–8 (2019).

148. Pezeshkian, W., Nåbo, L. J. & Ipsen, J. H. Cholera toxin B subunit induces local curvature on lipid bilayers. *FEBS Open Bio* **7**, 1638–1645 (2017).

149. Pezeshkian, W. *et al.* Membrane invagination induced by Shiga toxin B-subunit: from molecular structure to tube formation. *Soft Matter* **12**, 5164–5171 (2016).

150. Stang, E., Kartenbeck, J. & Parton, R. G. Major histocompatibility complex class I molecules mediate association of SV40 with caveolae. *Mol Biol Cell* **8**, 47–57 (1997).

151. Anderson, H. A., Chen, Y. & Norkin, L. C. MHC class I molecules are enriched in caveolae but do not enter with simian virus 40. *Journal of General Virology* **79**, 1469–1477 (1998).

152. Anderson, H. A., Chen, Y. & Norkin, L. C. Bound simian virus 40 translocates to caveolin-enriched membrane domains, and its entry is inhibited by drugs that selectively disrupt caveolae. *Mol Biol Cell* **7**, 1825–1834 (1996).

153. Norkin, L. C. Caveolae in the uptake and targeting of infectious agents and secreted toxins. *Advanced Drug Delivery Reviews* **49**, 301–315 (2001).

154. Scherer, P. E. *et al.* Cell-type and Tissue-specific Expression of Caveolin-2: caveolins 1 and 2 co-localize and form a stable hetero-oligomeric complex in vivo. *Journal of Biological Chemistry* **272**, 29337–29346 (1997).

155. Harris, J., Werling, D., Hope, J. C., Taylor, G. & Howard, C. J. Caveolae and caveolin in immune cells: distribution and functions. *Trends in Immunology* **23**, 158–164 (2002).

156. Mirre, C., Monlauzeur, L., Garcia, M., Delgrossi, M. H. & Le Bivic, A. Detergent-resistant membrane microdomains from Caco-2 cells do not contain caveolin. *American Journal of Physiology-Cell Physiology* **271**, C887–C894 (1996).

157. Campelo, F., McMahon, H. T. & Kozlov, M. M. The Hydrophobic Insertion Mechanism of Membrane Curvature Generation by Proteins. *Biophysical Journal* **95**, 2325–2339 (2008).

158. Solon, J., Gareil, O., Bassereau, P. & Gaudin, Y. Membrane deformations induced by the matrix protein of vesicular stomatitis virus in a minimal system. *J Gen Virol* **86**, 3357–3363 (2005).

159. Welsch, S., Müller, B. & Kräusslich, H.-G. More than one door – Budding of enveloped viruses through cellular membranes. *FEBS Letters* **581**, 2089–2097 (2007).

160. Busch, D. J. *et al.* Intrinsically disordered proteins drive membrane curvature. *Nat Commun* **6**, 7875 (2015).

161. Peter, B. J. *et al.* BAR Domains as Sensors of Membrane Curvature: The Amphiphysin BAR Structure. *Science* **303**, 495–499 (2004).

162. Mim, C. *et al.* Structural basis of membrane bending by the N-BAR protein endophilin. *Cell* **149**, 137–145 (2012).

163. Rao, Y. & Haucke, V. Membrane shaping by the Bin/amphiphysin/Rvs (BAR) domain protein superfamily. *Cell. Mol. Life Sci.* **68**, 3983–3993 (2011).

164. Frost, A. *et al.* Structural Basis of Membrane Invagination by F-BAR Domains. *Cell* **132**, 807–817 (2008).

165. Lakshminarayan, R. *et al.* Galectin-3 drives glycosphingolipid-dependent biogenesis of clathrin-independent carriers. *Nature Cell Biology* **16**, 592–603 (2014).

166. Hummeler, K., Tomassini, N. & Sokol, F. Morphological aspects of the uptake of simian virus 40 by permissive cells. *Journal of Virology* **6**, 87–93 (1970).

167. Maul, G. G., Rovera, G., Vorbrodt, A. & Abramczuk, J. Membrane fusion as a mechanism of simian virus 40 entry into different cellular compartments. *Journal of virology* **28**, 936–44 (1978).

168. Wolf, A. A., Fujinaga, Y. & Lencer, W. I. Uncoupling of the Cholera Toxin-GM1 Ganglioside Receptor Complex from Endocytosis, Retrograde Golgi Trafficking, and Downstream Signal Transduction by Depletion of Membrane Cholesterol. *Journal of Biological Chemistry* **277**, 16249–16256 (2002).

169. Sonnino, S., Mauri, L., Chigorno, V. & Prinetti, A. Gangliosides as components of lipid membrane domains. *Glycobiology* **17**, 1R-13R (2007).

170. Lozano, M. M. *et al.* Co-localization of the Ganglioside GM1 and Cholesterol Detected by Secondary Ion Mass Spectrometry. *J Am Chem Soc* **135**, 5620–5630 (2013).

171. Tsamaloukas, A., Szadkowska, H. & Heerklotz, H. Thermodynamic Comparison of the Interactions of Cholesterol with Unsaturated Phospholipid and Sphingomyelins. *Biophysical Journal* **90**, 4479–4487 (2006).

172. Sharma, P. *et al.* Nanoscale Organization of Multiple GPI-Anchored Proteins in Living Cell Membranes. *Cell* **116**, 577–589 (2004).

173. Chadda, R. *et al.* Cholesterol-Sensitive Cdc42 Activation Regulates Actin Polymerization for Endocytosis via the GEEC Pathway. *Traffic* **8**, 702–717 (2007).

174. Legler, D. F. *et al.* Differential insertion of GPI-anchored GFPs into lipid rafts of live cells. *The FASEB Journal* **19**, 73–75 (2005).

175. Madore, N. *et al.* Functionally different GPI proteins are organized in different domains on the neuronal surface. *The EMBO Journal* **18**, 6917–6926 (1999).

176. Brown, D. A. & Rose, J. K. Sorting of GPI-anchored proteins to glycolipid-enriched membrane subdomains during transport to the apical cell surface. *Cell* **68**, 533–544 (1992).

177. Kenworthy, A. K., Petranova, N. & Edidin, M. High-Resolution FRET Microscopy of Cholera Toxin B-Subunit and GPI-anchored Proteins in Cell Plasma Membranes. *MBoC* **11**, 1645–1655 (2000).

178. Glebov, O. O. & Nichols, B. J. Lipid raft proteins have a random distribution during localized activation of the T-cell receptor. *Nat Cell Biol* **6**, 238–243 (2004).

179. Rothberg, K. G. *et al.* Caveolin, a protein component of caveolae membrane coats. *Cell* **68**, 673–682 (1992).

180. Mayor, S., Rothberg, K. G. & Maxfield, F. R. Sequestration of GPI-Anchored Proteins in Caveolae Triggered by Cross-Linking. *Science* **264**, 1948–1951 (1994).

181. Parton, R. G., Joggerst, B. & Simons, K. Regulated internalization of caveolae. *Journal of Cell Biology* **127**, 1199–1215 (1994).

182. Fujimoto, T. GPI-anchored proteins, glycosphingolipids, and sphingomyelin are sequestered to caveolae only after crosslinking. *J Histochem Cytochem.* **44**, 929–941 (1996).

183. Yan, Y. *et al.* Bafilomycin A1 induces caspase-independent cell death in hepatocellular carcinoma cells via targeting of autophagy and MAPK pathways. *Sci Rep* **6**, 37052 (2016).

184. Bafilomycin A1 targets both autophagy and apoptosis pathways in pediatric B-cell acute lymphoblastic leukemia | Haematologica. https://haematologica.org/article/view/7306.

185. Gee, G. V., O'Hara, B. A., Derdowski, A. & Atwood, W. J. Pseudovirus mimics cell entry and trafficking of the human polyomavirus JCPyV. *Virus Res* **178**, 10.1016/j.virusres.2013.09.030 (2013).

186. Levis, G. M., Evangelatos, G. P. & Crumpton, M. J. Lipid composition of lymphocyte plasma membrane from pig mesenteric lymph node. *Biochem J* **156**, 103–110 (1976).

187. Örtegren, U. *et al.* Lipids and glycosphingolipids in caveolae and surrounding plasma membrane of primary rat adipocytes. *European Journal of Biochemistry* **271**, 2028–2036 (2004).

188. Lauvrak, S. U., Torgersen, M. L. & Sandvig, K. Efficient endosome-to-Golgi transport of Shiga toxin is dependent on dynamin and clathrin. *Journal of Cell Science* **117**, 2321–2331 (2004).

189. Aghamohammadzadeh, S. & Ayscough, K. R. Differential requirements for actin during yeast and mammalian endocytosis. *Nat Cell Biol* **11**, 1039–1042 (2009).

190. Boulant, S., Kural, C., Zeeh, J.-C., Ubelmann, F. & Kirchhausen, T. Actin dynamics counteract membrane tension during clathrin-mediated endocytosis. *Nat Cell Biol* **13**, 1124–1131 (2011).

191. Hinze, C. & Boucrot, E. Local actin polymerization during endocytic carrier formation. *Biochemical Society Transactions* **46**, 565–576 (2018).

192. Howes, M. T., Mayor, S. & Parton, R. G. Molecules, mechanisms, and cellular roles of clathrin-independent endocytosis. *Current Opinion in Cell Biology* **22**, 519–527 (2010).

193. Goswami, D. *et al.* Nanoclusters of GPI-Anchored Proteins Are Formed by Cortical Actin-Driven Activity. *Cell* **135**, 1085–1097 (2008).

194. Simunovic, M. *et al.* Friction Mediates Scission of Tubular Membranes Scaffolded by BAR Proteins. *Cell* **170**, 172-184.e11 (2017).

195. Nakamura, N. *et al.* Characterization of a cis-Golgi matrix protein, GM130. *Journal of Cell Biology* **131**, 1715–1726 (1995).

196. Nichols, B. J. *et al.* Rapid Cycling of Lipid Raft Markers between the Cell Surface and Golgi Complex. *J Cell Biol* **153**, 529–542 (2001).

197. McKenzie, J., Johannes, L., Taguchi, T. & Sheff, D. Passage through the Golgi is necessary for Shiga toxin B subunit to reach the endoplasmic reticulum. *The FEBS Journal* **276**, 1581–1595 (2009).

198. Fairhead, M. *et al.* SpyAvidin hubs enable precise and ultrastable orthogonal nanoassembly. *Journal of the American Chemical Society* **136**, 12355–12363 (2014).

199. Dubacheva, G. V. *et al.* Controlling Multivalent Binding through Surface Chemistry: Model Study on Streptavidin. *Journal of the American Chemical Society* **139**, 4157–4167 (2017).

200. Ashok, A. & Atwood, W. J. Contrasting Roles of Endosomal pH and the Cytoskeleton in Infection of Human Glial Cells by JC Virus and Simian Virus 40. *Journal of Virology* **77**, 1347–1356 (2003).

201. Gorelik, L. *et al.* Progressive multifocal leukoencephalopathy (PML) development is associated with mutations in JC virus capsid protein VP1 that change its receptor specificity. *Journal of Infectious Diseases* **204**, 103–114 (2011).

202. Ströh, L. J. & Stehle, T. Glycan Engagement by Viruses: Receptor Switches and Specificity. *Annual Review of Virology* **1**, 285–306 (2014).

203. Masterson, W. J., Raper, J., Doering, T. L., Hart, G. W. & Englund, P. T. Fatty acid remodeling: A novel reaction sequence in the biosynthesis of trypanosome glycosyl phosphatidylinositol membrane anchors. *Cell* **62**, 73–80 (1990).

204. Conzelmann, A., Puoti, A., Lester, R. l. & Desponds, C. Two different types of lipid moieties are present in glycophosphoinositol-anchored membrane proteins of Saccharomyces cerevisiae. *The EMBO Journal* **11**, 457–466 (1992).

205. Lingwood, D. & Simons, K. Lipid rafts as a membrane-organizing principle. *Science* **327**, 46–50 (2010).

206. Clark, P. *et al*. Phosphoinositide 3′-Kinase γ Facilitates Polyomavirus Infection. *Viruses* **12**, 1190 (2020).

207. Huotari, J. & Helenius, A. Endosome maturation. *The EMBO Journal* **30**, 3481–3500 (2011).

208. Zerial, M. & McBride, H. Rab proteins as membrane organizers. *Nat Rev Mol Cell Biol* **2**, 107–117 (2001).

209. Rink, J., Ghigo, E., Kalaidzidis, Y. & Zerial, M. Rab conversion as a mechanism of progression from early to late endosomes. *Cell* **122**, 735–749 (2005).

210. Chatterjee, S., Smith, E. R., Hanada, K., Stevens, V. L. & Mayor, S. GPI anchoring leads to sphingolipid-dependent retention of endocytosed proteins in the recycling endosomal compartment. *EMBO Journal* **20**, 1583–1592 (2001).

211. Mayor, S., Sabharanjak, S. & Maxfield, F. R. Cholesterol-dependent retention of GPI-anchored proteins in endosomes. *The EMBO Journal* **17**, 4626–4638 (1998).

212. Feng, H., Shuda, M., Chang, Y. & Moore, P. S. Clonal integration of a polyomavirus in human Merkel cell carcinoma. *Science* **319**, 1096–1100 (2008).

213. Erickson, K. D., Garcea, R. L. & Tsai, B. Ganglioside GT1b Is a Putative Host Cell Receptor for the Merkel Cell Polyomavirus. *Journal of Virology* **83**, 10275–10279 (2009).

214. Liu, W., Krump, N. A., MacDonald, M. & You, J. Merkel Cell Polyomavirus Infection of Animal Dermal Fibroblasts. *J Virol* **92**, e01610-17 (2018).

215. Liu, W. *et al*. Identifying the target cells and mechanisms of Merkel cell polyomavirus infection. *Cell Host Microbe* **19**, 775–787 (2016).

216. Breau, W. C., Atwood, W. J. & Norkin, L. C. Class I major histocompatibility proteins are an essential component of the simian virus 40 receptor. *Journal of virology* **66**, 2037–45 (1992).

217. Caruso, M., Belloni, L., Sthandier, O., Amati, P. & Garcia, M.-I. 4 1 Integrin Acts as a Cell Receptor for Murine Polyomavirus at the Postattachment Level. *Journal of Virology* **77**, 3913–3921 (2003).

218. Schowalter, R. M., Pastrana, D. V. & Buck, C. B. Glycosaminoglycans and sialylated glycans sequentially facilitate merkel cell polyomavirus infectious entry. *PLoS Pathogens* **7**, e1002161 (2011).

219. Mayberry, C. L., Soucy, A. N., Lajoie, C. R., DuShane, J. K. & Maginnis, M. S. JC Polyomavirus Entry by Clathrin-Mediated Endocytosis Is Driven by β-Arrestin. *Journal of Virology* **93**, JVI.01948-18 (2019).

220. Elphick, G. F. *et al.* The human polyomavirus, JCV, uses serotonin receptors to infect cells. *Science* **306**, 1380–1383 (2004).

221. Assetta, B. *et al.* Genetic and Functional Dissection of the Role of Individual 5-HT2 Receptors as Entry Receptors for JC Polyomavirus. *Cell Rep* **27**, 1960-1966.e6 (2019).

222. Chakraborty, S. K. *et al.* Cholera Toxin B Conjugated Quantum Dots for Live Cell Labeling. *Nano Lett.* **7**, 2618–2626 (2007).

223. Nelson, C. D. S., Derdowski, A., Maginnis, M. S., O'Hara, B. A. & Atwood, W. J. The VP1 subunit of JC polyomavirus recapitulates early events in viral trafficking and is a novel tool to study polyomavirus entry. *Virology* **428**, 30–40 (2012).

224. Mannova, P. & Forstova, J. Mouse Polyomavirus Utilizes Recycling Endosomes for a Traffic Pathway Independent of COPI Vesicle Transport. *Journal of Virology* **77**, 1672–1681 (2003).

225. Ruggiero, F. M., Vilcaes, A. A., Yuki, N. & Daniotti, J. L. Membrane binding, endocytic trafficking and intracellular fate of high-affinity antibodies to gangliosides GD1a and GM1. *Biochimica et Biophysica Acta - Biomembranes* **1859**, 80–93 (2017).

226. Arnaud, J. *et al.* Reduction of Lectin Valency Drastically Changes Glycolipid Dynamics in Membranes but Not Surface Avidity. *ACS Chem. Biol.* **8**, 1918–1924 (2013).

227. Massol, R. H., Larsen, J. E., Fujinaga, Y., Lencer, W. I. & Kirchhausen, T. Cholera Toxin Toxicity Does Not Require Functional Arf6- and Dynamin-dependent Endocytic Pathways. *MBoC* **15**, 3631–3641 (2004).

228. Matsudaira, T., Niki, T., Taguchi, T. & Arai, H. Transport of the cholera toxin B-subunit from recycling endosomes to the Golgi requires clathrin and AP-1. *Journal of Cell Science* **128**, 3131–3142 (2015).

229. Orth, D. *et al.* Shiga Toxin Activates Complement and Binds Factor H: Evidence for an Active Role of Complement in Hemolytic Uremic Syndrome1. *The Journal of Immunology* **182**, 6394–6400 (2009).

230. Wang, S. & Bellen, H. J. The retromer complex in development and disease. *Development* **142**, 2392–2396 (2015).

231. Utskarpen, A., Slagsvold, H. H., Dyve, A. B., Skånland, S. S. & Sandvig, K. SNX1 and SNX2 mediate retrograde transport of Shiga toxin. *Biochemical and Biophysical Research Communications* **358**, 566–570 (2007).

232. Popoff, V. *et al.* The retromer complex and clathrin define an early endosomal retrograde exit site. *Journal of Cell Science* **120**, 2022–2031 (2007).

233. Mallard, F. *et al.* Early/recycling endosomes-to-TGN transport involves two SNARE complexes and a Rab6 isoform. *Journal of Cell Biology* **156**, 653–664 (2002).

234. Del Nery, E. *et al.* Rab6A and Rab6A′ GTPases Play Non-overlapping Roles in Membrane Trafficking. *Traffic* **7**, 394–407 (2006).

235. Ganley, I. G., Espinosa, E. & Pfeffer, S. R. A syntaxin 10–SNARE complex distinguishes two distinct transport routes from endosomes to the trans-Golgi in human cells. *Journal of Cell Biology* **180**, 159–172 (2008).

236. Amessou, M. *et al.* Syntaxin 16 and syntaxin 5 are required for efficient retrograde transport of several exogenous and endogenous cargo proteins. *Journal of Cell Science* **120**, 1457–1468 (2007).

237. Jones, J. A. & Giessen, T. W. Advances in encapsulin nanocompartment biology and engineering. *Biotechnol Bioeng* **118**, 491–505 (2021).

238. Fabricius, V., Lefèbre, J., Geertsema, H., Marino, S. F. & Ewers, H. Rapid and efficient C-terminal labeling of nanobodies for DNA-PAINT. *J. Phys. D: Appl. Phys.* **51**, 474005 (2018).

239. Delarue, M. *et al.* mTORC1 Controls Phase Separation and the Biophysical Properties of the Cytoplasm by Tuning Crowding. *Cell* **174**, 338-349.e20 (2018).

240. Chua, J., Rikhy, R. & Lippincott-Schwartz, J. Dynamin 2 orchestrates the global actomyosin cytoskeleton for epithelial maintenance and apical constriction. *Proc Natl Acad Sci U S A* **106**, 20770–20775 (2009).

241. Bayer, N. J. *et al.* Structure of Merkel Cell Polyomavirus Capsid and Interaction with Its Glycosaminoglycan Attachment Receptor. *Journal of Virology* **94**, 10.1128/jvi.01664-19 (2020).

242. Buck, C. B., Pastrana, D. V., Lowy, D. R. & Schiller, J. T. Efficient Intracellular Assembly of Papillomaviral Vectors. *Journal of Virology* **78**, 751–757 (2004).

243. Zha, X. *et al.* Sphingomyelinase Treatment Induces ATP-independent Endocytosis. *Journal of Cell Biology* **140**, 39–47 (1998).

244. Dimitrov, D. S. & Angelova, M. I. Lipid swelling and liposome formation on solid surfaces in external electric fields. in *New Trends in Colloid Science* (ed. Hoffmann, H.) 48–56 (Steinkopff, 1987). doi:10.1007/3-798-50724-4_62.

245. Sezgin, E. *et al.* Elucidating membrane structure and protein behavior using giant plasma membrane vesicles. *Nature Protocols* **7**, 1042–1051 (2012).

246. Mastronarde, D. N. Automated electron microscope tomography using robust prediction of specimen movements. *Journal of Structural Biology* **152**, 36–51 (2005).

247. Kremer, J. R., Mastronarde, D. N. & McIntosh, J. R. Computer Visualization of Three-Dimensional Image Data Using IMOD. *Journal of Structural Biology* **116**, 71–76 (1996).

248. Paul-Gilloteaux, P. *et al.* eC-CLEM: flexible multidimensional registration software for correlative microscopies. *Nat Methods* **14**, 102–103 (2017).

249. de Chaumont, F. *et al.* Icy: an open bioimage informatics platform for extended reproducible research. *Nat Methods* **9**, 690–696 (2012).

250. Sochacki, K. A., Shtengel, G., van Engelenburg, S. B., Hess, H. F. & Taraska, J. W. Correlative super-resolution fluorescence and metal-replica transmission electron microscopy. *Nat Methods* **11**, 305–308 (2014).

251. Sochacki, K. A. & Taraska, J. W. Correlative Fluorescence Super-Resolution Localization Microscopy and Platinum Replica EM on Unroofed Cells. in *Super-Resolution Microscopy: Methods and Protocols* (ed. Erfle, H.) 219–230 (Springer, 2017). doi:10.1007/978-1-4939-7265-4_18.

252. Schindelin, J. *et al.* Fiji: an open-source platform for biological-image analysis. *Nat Methods* **9**, 676–682 (2012).

253. Carpenter, A. E. *et al.* CellProfiler: image analysis software for identifying and quantifying cell phenotypes. *Genome Biology* **7**, R100 (2006).

254. Raatz, M., Lipowsky, R. & Weikl, T. R. Cooperative wrapping of nanoparticles by membrane tubes. *Soft Matter* **10**, 3570–3577 (2014).

Curriculum Vitae

Highly motivated and proactive cell biologist with an interdisciplinary background. I have an innate curiosity about how things work, and I am keen on tackling complicated scientific riddles through innovative solutions. I am open to expanding my mindset through new experiences and enjoy meeting new people with different backgrounds, traveling, reading literature and going hiking.

Professional Experience

02/2018 – present - **Doctoral Researcher**

Biochemistry Institute of the Freie Universität Berlin, Germany
Multivalent lipid-binding triggered membrane deformation and endocytosis– in the group of Prof. Helge Ewers

03/2022 - **Visiting scientist**

European Molecular Biology Laboratory (EMBL), Heidelberg, Germany
Part of a collaboration with the Electron Microscopy Core facility

03/2018 - **Visiting scientist**

Institut Pasteur, Paris, France
Principles and Applications of Fluorescence Microscopy workshop

10/2016 – 12/2017 **- Student Research Assistant**
B CUBE - Center for molecular bioengineering, Technische Universität Dresden, Germany
Reconstitution of *in vitro* motor protein-cargo gliding assays – in the group of Prof. Stefan Diez

Education

02/2018 – present
PhD candidate in Biochemistry at the **Freie Universität Berlin, Germany**
Doctoral thesis supervisor: Prof. Helge Ewers

10/2015 – 10/2017
MSc in Biophysics at the **Technische Universität Dresden, Germany**

09/2011 – 07/2015
BEng in Applied Engineering Sciences (Physics) at **Babes-Bolyai University, Romania**

Publications

R. Groza, K. Schmidt, P. Müller, P. Ronchi, C. Schlack-Leigers, U. Neu, D. Puchkov, R. Dimova, C. Matthäus, J. Taraska, T. Weikl, H. Ewers, Adhesion energy controls lipid binding-mediated endocytosis, *bioRxiv*, 2023

F. Goerdeler, E. Reuber, J. Lühle, S. Leichnitz, A. Freitag, R. Nedielkov, **R. Groza**, H. Ewers, H. Möller, P. Seeberger, O. Moscovitz, Thiol-Mediated Uptake of a Cysteine-Containing Nanobody for Anticancer Drug Delivery, *ACS Central Science*, 2023

R. Groza, H. Ewers, Membrane deformation by the cholera toxin beta subunit requires more than one binding site, *PNAS*, 2020

A.M. Craciun, **R. Groza**, D. Maniu, S. Astilean, Steady-state and time-resolved fluorescence studies on the conjugation of Rose Bengal to gold nanorods, *Journal of Molecular Structure*, 2014

Conferences

Biomembrane days – Berlin, Germany
09/2022 – oral presentation

Molecular basis for membrane remodelling and organisation – Roscoff, France
05/2022 – poster presentation

Biophysical Society Annual Meeting (BPS) – San Francisco, California
02/2022 – poster presentation

International Symposium on Glycovirology - Schöntal, Germany
05/2018 – oral presentation

Reviewing activity

Nature Communications, since 2023

Teaching experience

Tutor for the Quantitative fluorescence microscopy method course, **Freie Universität Berlin, Germany**
05/2018 - 05/2021

Supervisor for 2 Biochemistry master students and 2 Biochemistry bachelor students, **Freie Universität Berlin, Germany**
10/2021 – 10/2023

Languages

Romanian	Native
English	C1
German	B1/B2

Research skills

Mammalian cell culture, transfection, stable cell line generation, inhibitor assays
Flow cytometry
Molecular cloning
Protein expression and purification
Model membrane systems (Giant Unilamellar Vesicles, Supported lipid bilayers)
Immunofluorescence
Fluorescence microscopy imaging

Other skills & activities

Organizer of the Virocarb PhD Symposium 2021 for the FOR2327 consortium
Volunteer at the Long Night of Science, Berlin
Data analysis: ImageJ, FlowJo, CellProfiler, Origin
Figure generation and illustrations: Adobe Illustrator
Programming languages: Python (basic), Matlab (basic)

Annexes

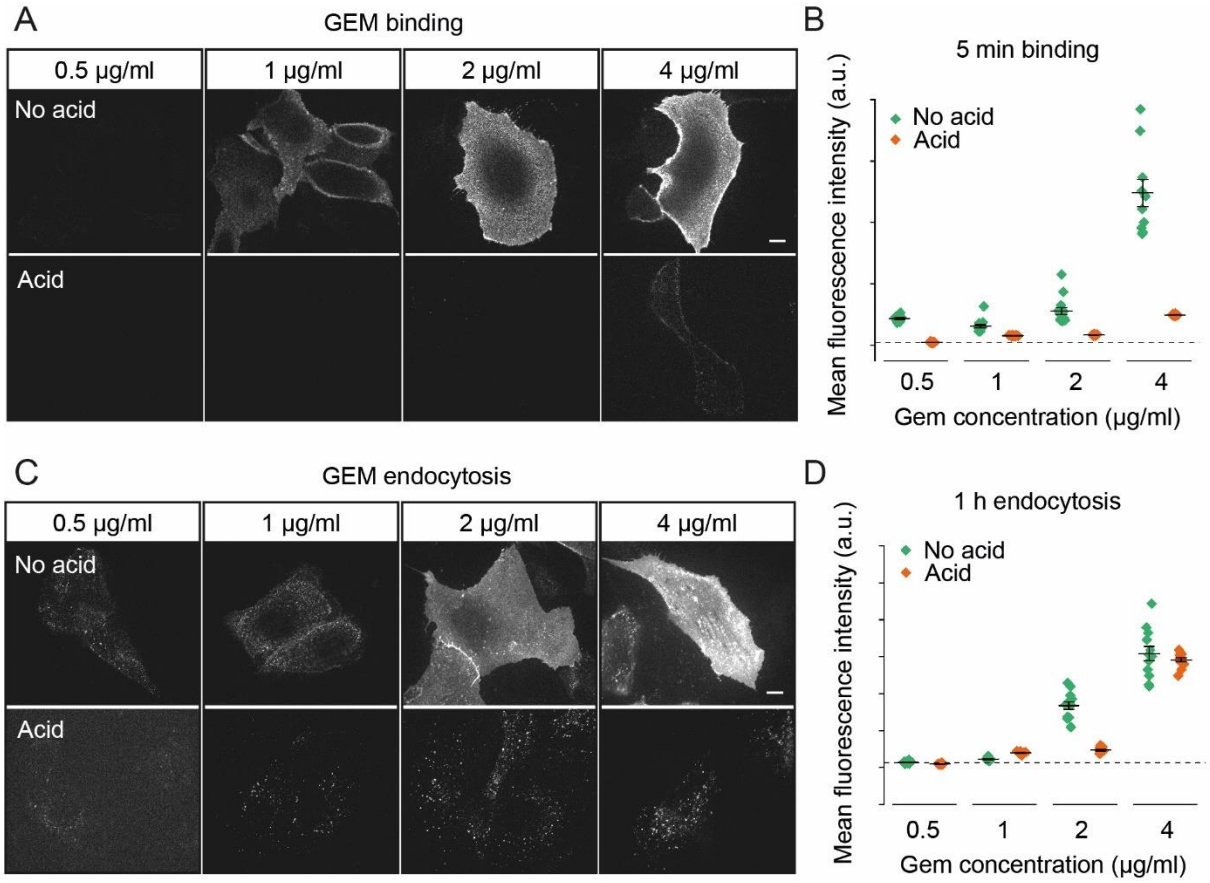

Annex 1. Quantitative endocytosis assay validation part 1: acid stripping of the ligand surface-bound fraction. A. Fluorescence micrographs of CV1 cells expressing a high-affinity GPI-anchored anti-GFP nanobody incubated for 5 min at 37 ˚C with increasing GEM-GFP concentrations as indicated. Top panel: fluorescence micrographs of GEM binding without further treatment. Bottom panel: fluorescence micrographs of GEM binding followed by acidic buffer washing. **B.** Quantification of the fluorescence intensity of the cells containing GEMs bound to their membrane, represented in panel A. Shown are means± s.e.m. Dotted line represents fluorescence background levels. **C.** Fluorescence micrographs of CV1 cells expressing a high-affinity GPI-anchored anti-GFP nanobody incubated for 1 h at 37 ˚C with increasing GEM-GFP concentrations as indicated. Top panel: fluorescence micrographs of GEM endocytosis without further treatment. Bottom panel: fluorescence micrographs of GEM endocytosis followed by acidic buffer washing. **D.** Quantification of the fluorescence intensity of the cells containing internalized GEMs, represented in panel C. Shown are means± s.e.m. Dotted line represents fluorescence background levels.

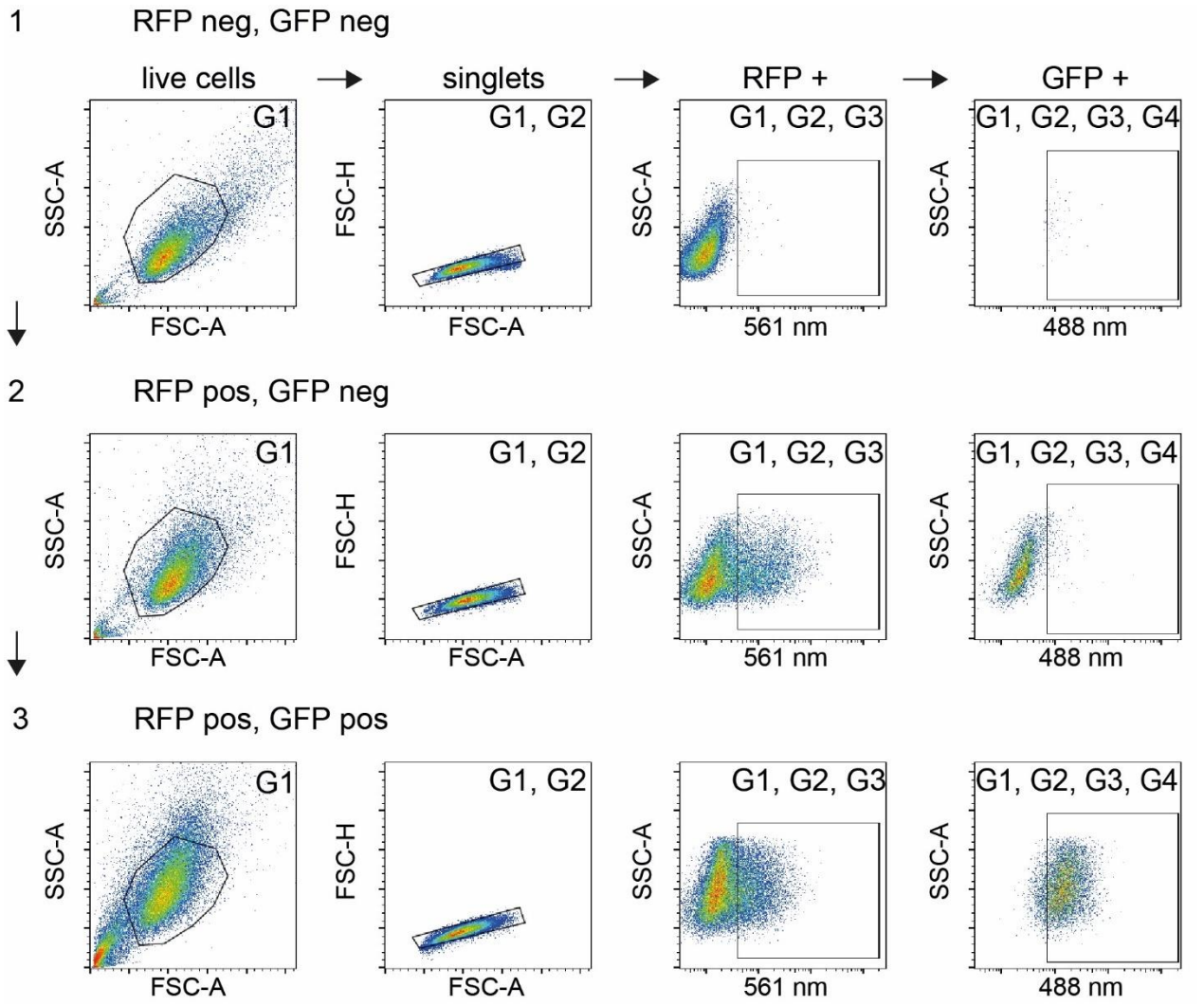

Annex 2. Quantitative endocytosis assay validation part 2: gating strategy for the flow cytometry experiments. In brief, live cell population was always selected first, indicated as G1 (left panels). From the selected live cell population, doublets and aggregates were always removed, indicated as G1, G2 (second panels from the left). Next, the RFP positive population gate was selected according to the RFP negative control in the top panels. This gate is marked as G1, G2, G3 (second panels from the right). Next, the GFP positive population gate was selected according to the RFP positive, GFP negative control shown in the middle panels. This gate is marked as G1, G2, G3, G4 (right panels). A representative sample of GEMs in GPI-anchored anti-GFP nanobody expressing cells is shown in the lower panel, the respective gates as indicated. Figure S6 displays the G1,G2,G3,G4 gate (GEM-GFP positive) as histograms and the corresponding G1,G2,G3 gate (RFP positive) for the RFP co-transfection levels of the same cells. All samples were washed in acidic buffer before measurement.

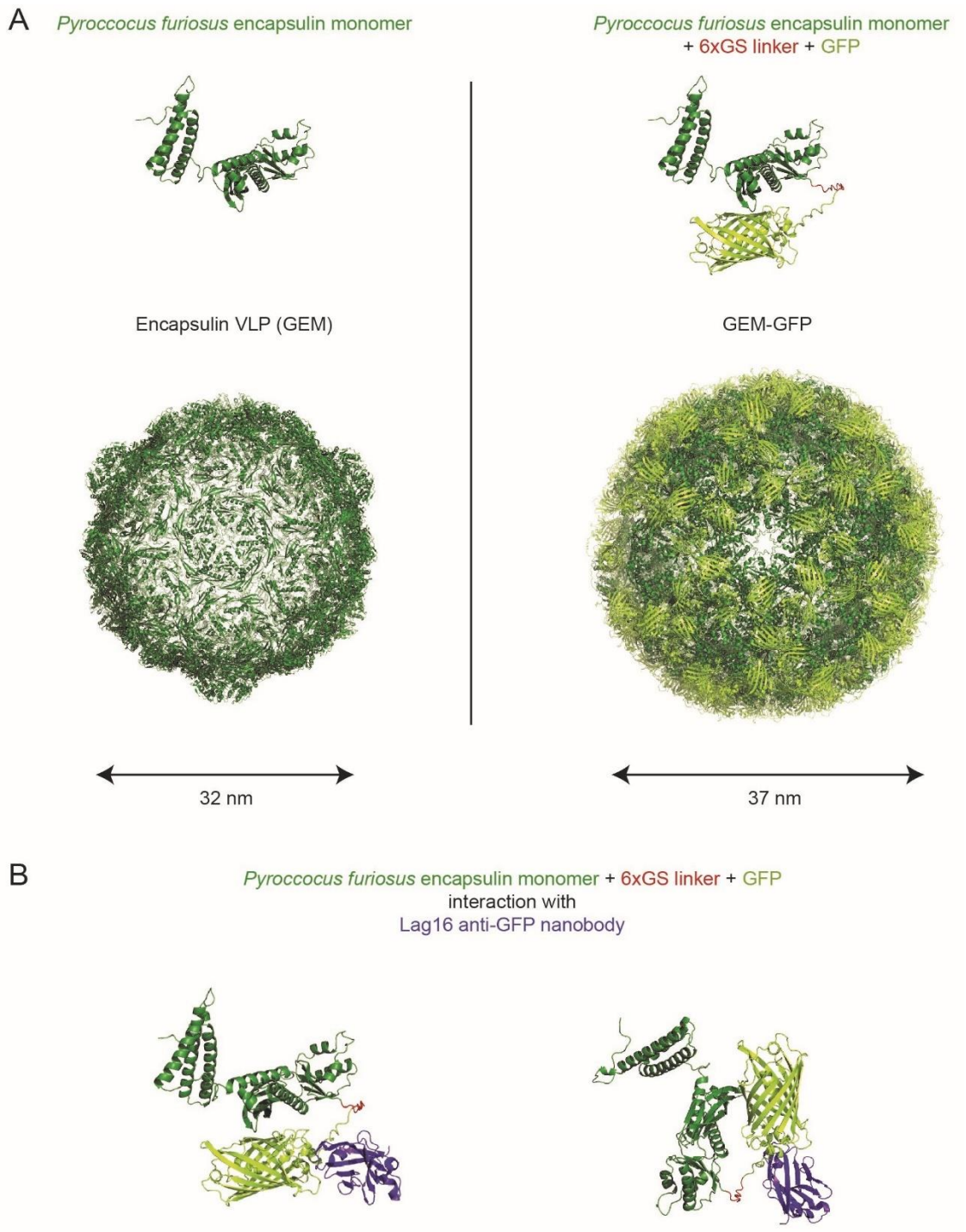

Annex 3. Structural assembly of the synthetic polyvalent lipid binder GEM-GFP and its interaction with receptors. A. Core proteins and assembled capsids of the Pyroccocus furiosus VLP vs. the artificial GEM VLP. Top left panel: crystal structure of the encapsuling protein; Bottom left panel: crystal structure of the virus-like-particle from the Pyrococcus furiosus archaeon. PDB file: 2E0Z. Top right panel: predicted 3D structure of the encapsulin core protein genetically linked to a GFP molecule (as simulated with AlphaFold based on the amino acid sequence). Bottom right panel: 3D structure of the entire GEM VLP bearing 180 copies of the GFP protein on its surface (reconstructed in PyMol based on the AlphaFold predicted structure of the encapsuling monomer). **B.** Interaction between the GEM-GFP monomer and the 0.7 nM binding affinity anti-GFP nanobody. PDB file: 7SAH.

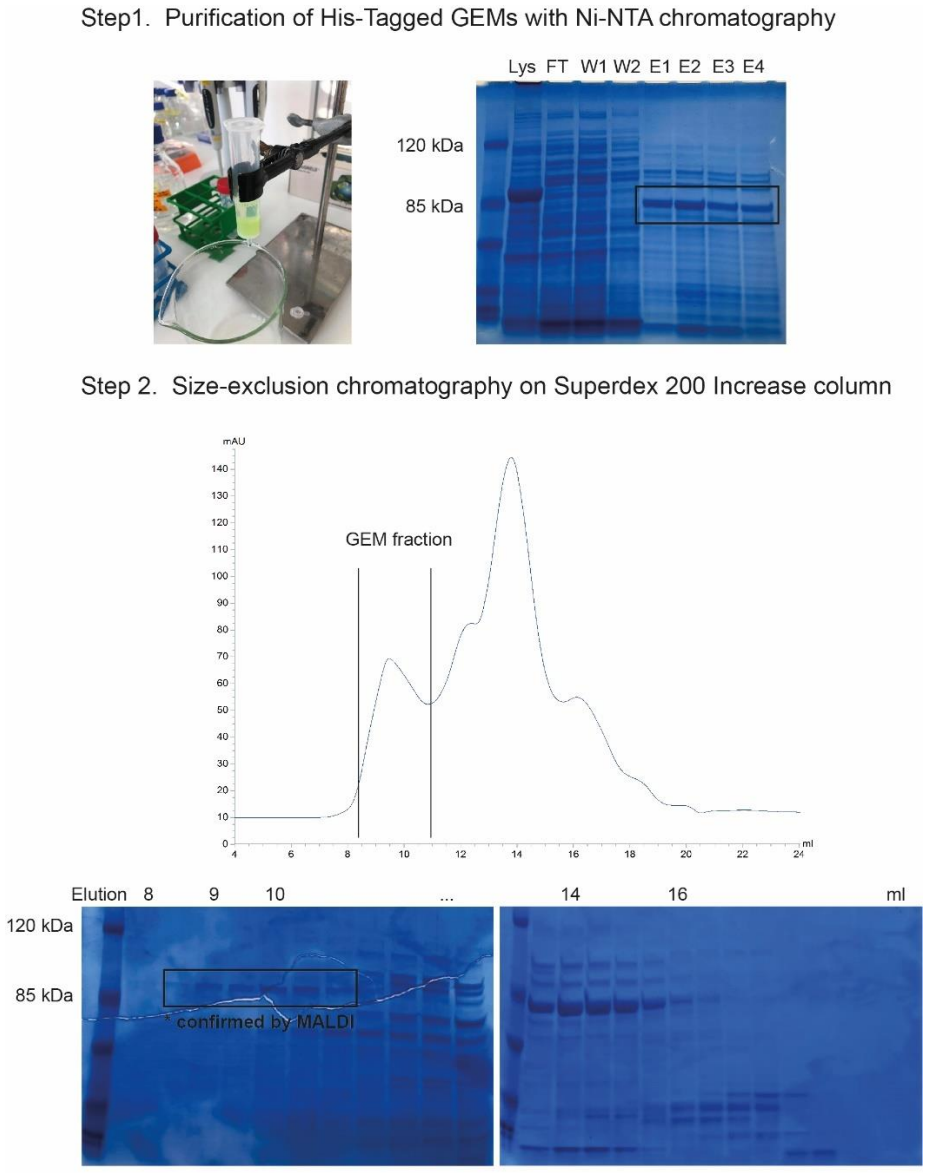

Annex 4. Purification procedure of the GEM-GFP virus-like-particles. In brief, the cleared bacterial lysate was passed through a Ni-NTA-bead gravity flow column (left image) that allowed for extraction of the His-tagged GEMs. SDS-Page gel was run with samples from all the purification steps to identify the fractions containing the protein of interest (right image). Next, a size-exclusion chromatography run was performed with the elution from the first step on a Superdex 200 Increase 10/300 GL column. The fractions eluted in the void volume of the column were verified to contain GEM-GFP proteins by SDS-Page gel and by MALDI mass spectrometry of the marked SDS-page bands. Finally, the purification procedure was validated using transmission electron microscopy to detect individual particles with high resolution.

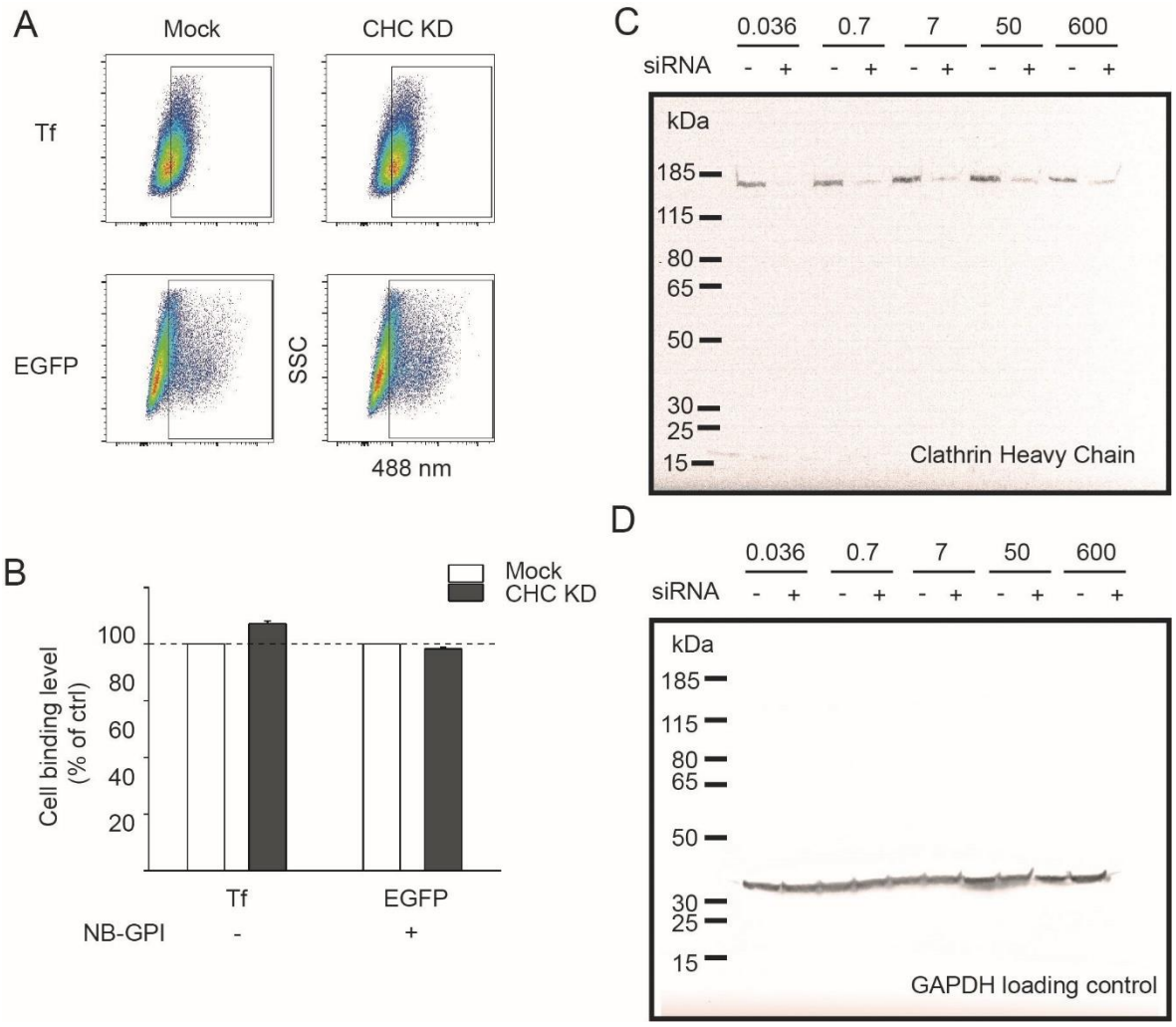

Annex 5. Validation of the CHC knock down assays. **A-B** Quantification of surface receptor levels for mock and siRNA treated samples. **C-D** Validation of the decrease in CHC total protein content in siRNA treated samples vs mock. **A)** Fluorescence intensity dot blots from flow cytometry measurements of Transferrin-AF488 binding (top panel) to non-transfected CV1 cells or of EGFP binding (bottom panel) to CV1 cells expressing the 0.036 nM binding affinity GPI-anchored nanobody receptor. Cells were either mock treated (left panels) or treated with genetic inhibitors (siRNA) against clathrin-heavy-chain (right panels). The cells were incubated with 2 µg of either Transferrin-AF488 or recombinant EGFP for 45 min at 4 ˚C before flow cytometry measurements. **B)** Quantification of Transferrin-AF488 and EGFP binding to cells upon mock or siRNA treatment, as represented in the flow cytometry dot blots in panel A). Measured is intensity of at least 5000 cells/sample, shown is means ± s.e.m., n = 2 independent experiments. **C)** Scan of uncropped western blot showing CHC levels in cells expressing the panel of GPI-anchored anti-GFP nanobody constructs as indicated. Cells were either mock treated or treated with siRNA against CHC for 48 h at 37 ˚C. **D)** Scan of the same uncropped blot as in panel C) stripped of anti-CHC antibodies and re-labeled with anti-GAPDH antibody as loading control.

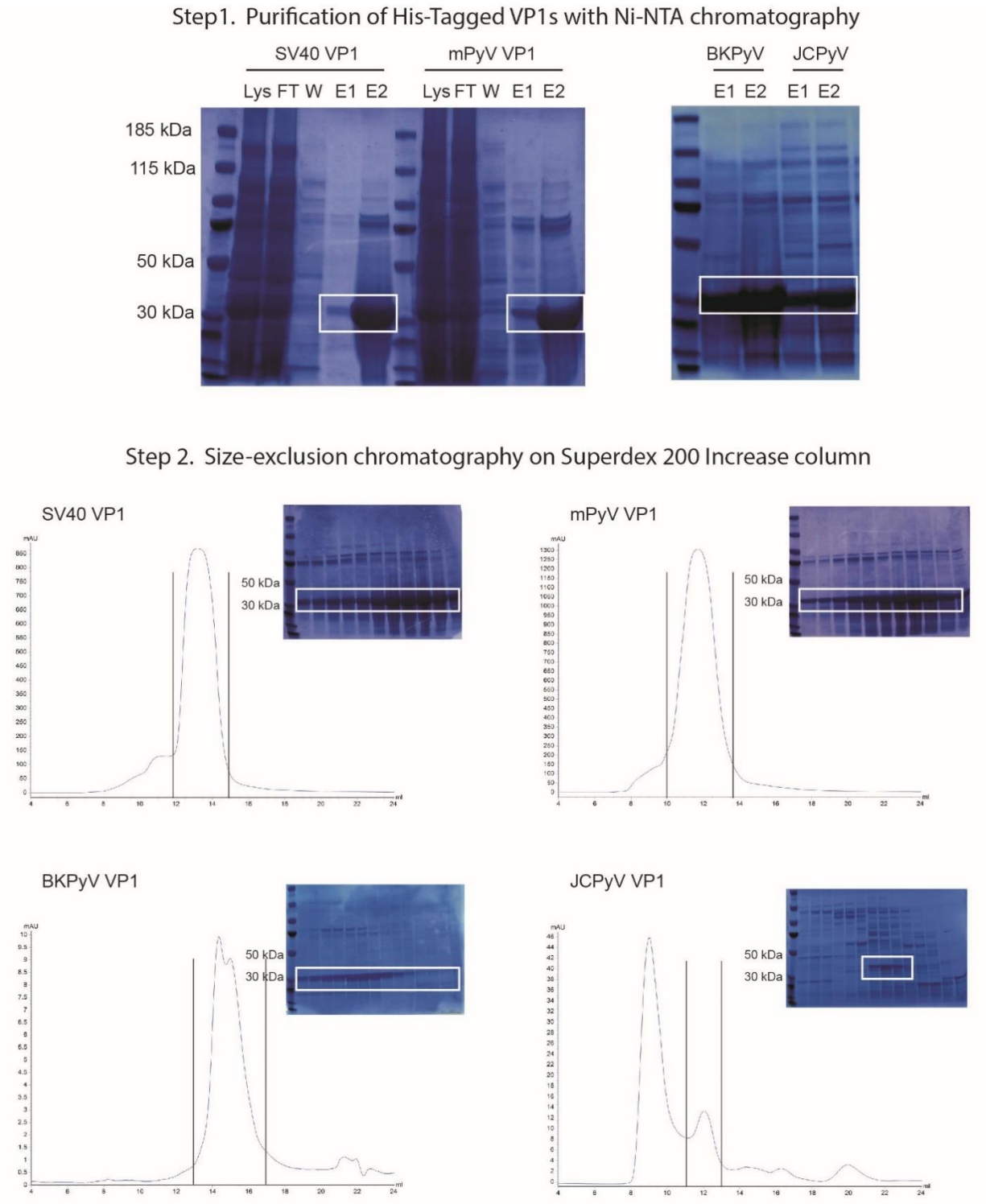

Annex 6. Purification procedure of the truncated polyoma VP1 pentamers. In brief, the cleared bacterial lysates expressing each of the different polyoma VP1s were passed through Ni-NTA-bead gravity flow columns that allowed for extraction of the His-tagged pentamers. SDS-Page gels were run with samples from all the purification steps to identify the fractions containing the protein of interest as indicated. Next, size-exclusion chromatography was performed with the elution fractions from the first step on a Superdex 200 Increase 10/300 GL column. The eluted fractions were verified to contain the protein of interest by SDS-Page gel as indicated.

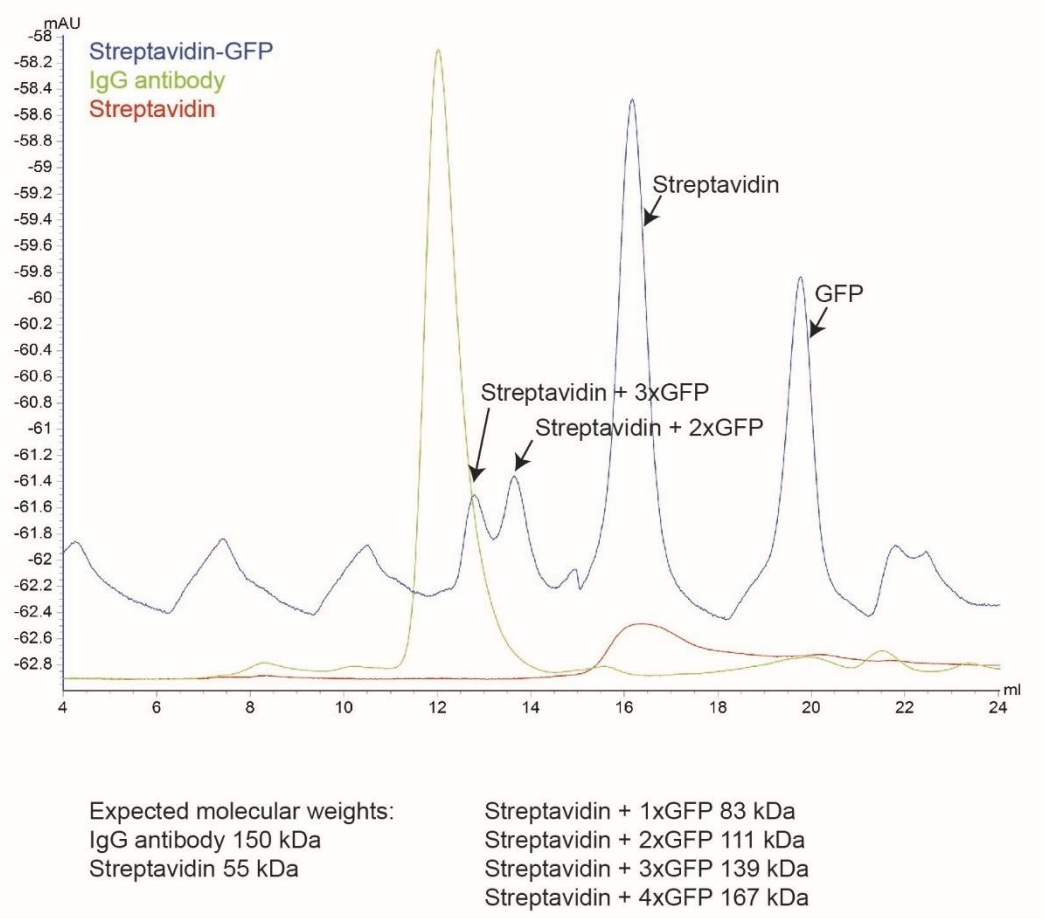

Annex 7. Streptavidin complexed to GFP population determined by size-exclusion chromatography. Control runs were performed with IgG antibodies and unlabeled Streptavidin to calibrate the molecular weight of the eluted fractions. The streptavidin-GFP complexes were then eluted, revealing four distinct populations: unbound GFP, unlabelled streptavidin and 2 or 3 copies of GFP successfully bound to streptavidin.

Acknowledgements

First, I would like to thank my supervisor Prof. Helge Ewers for his mentoring and enthusiastic support throughout the years. I learned a great deal from you and had lots of fun doing science together. I hope your kindness and excitement will inspire other students in the future like they inspired me.

I would like to thank my second supervisor, Prof. Francesca Bottanelli, for taking the time to correct this thesis. I am in deep awe of mothers in science, thank you for the strong example.

I would like to acknowledge all the collaborators that contributed to this study and the paper. First and foremost, thank you to Dr. Thomas Weikl for the fruitful discussions and theoretical model developed for this study. Thanks for offering me the chance to give a talk at Biomembrane days, I hope we will collaborate further in the future. Thanks to Prof. Claudia Matthäus for her contribution and moral support, it was nice talking to you. Huge thanks to Dr. Ursula Neu for taking the time to help me establish the GEM purification procedure. Thanks to Dr. Paolo Ronchi from the EMBL for his prompt and efficient delivery of the CLEM results. Thank you to Justin Taraska, Dmytro Puchkov Rumiana Dimova for the support. Thanks to Thilo Stehle and his lab members for helping with the purification of the MCPyV and providing plasmids.

Big thank you goes to the members of the lab, especially to those who helped with my project: Claire, Markus and Kita. Thanks to Bas for the corrections of the thesis, to Amin for helping with the analysis pipelines, Purba and Ando for being a ray of sunlight, thanks to Jakob for the laughs, thanks to Nadja, Ria and Micha for their support. Thanks to all my other students and to former lab members that offered me advice, thanks Jia.

Next, I want to say a huge thanks to all my close friends for always being there for me. Thanks, Claire, for being my best friend in the lab and for all the life advice. Also big, big thanks to Andrea (Senge) for unconditional help in the lab, for inviting me into your home and making me feel part of your family. I would also like to thank Mengfei for always being available for my (many) bad moments. Thanks to Ursula and Peter, you have become a very important part of my life that brings a smile to my face in any situation. Thanks to Deni and Mihai for the good times. Thanks to my best friends back in Romania for sticking with me since high school: Didi, Larisa, Marina, Sonia and especially, Diana. Thanks for being part of my life. Also Iris, I am grateful to have connected with you after graduation, thanks for becoming my best friend.

Thanks to my family for the support. My parents but specially my grandparents for believing in me and my dreams. Last but not least, thanks to Andrei for the immense support, for growing with me and creating a life together. Looking forward to the next chapter together.